Dissertation
submitted to the
Combined Faculties of the Natural Sciences and Mathematics
of the Ruperto-Carola-University of Heidelberg, Germany
for the degree of
Doctor of Natural Sciences

Put forward by
Friedhelm Serwane
Born in: Munich
Oral examination: November 2nd, 2011

Deterministic preparation of a tunable few-fermion system

Referees: **Prof. Dr. Selim Jochim**
Prof. Dr. Klaus Blaum

Abstract:

This thesis reports on the preparation of a tunable few-fermion system using ultracold ^{6}Li atoms in an optical dipole trap. We prepare ground state systems consisting of 1 to 10 fermions with fidelities of ∼90%. This system has the unique property that key parameters such as particle number, inter-particle interactions and external confining potential are tunable.

We use this model system to explore two interacting atoms confined in a one-dimensional potential. For increasing repulsion we measure a decrease of the tunneling time of one atom through a barrier which is created by tilting the potential. From the measured tunneling time we calculate the interaction energy of the system using the WKB technique. This requires detailed knowledge of the confining potential, which we obtain by controlling the motional quantum state of a single atom in the trap.

To increase the preparation fidelity of the few-particle systems a high-resolution objective has been designed during this thesis. It will allow us to explore tunable quantum systems in two and three dimensions confined in arbitrary potentials.

Because of its great tunability our model system is uniquely suited to explore strongly correlated few-fermion systems, which is one of the major challenges of modern physics.

Zusammenfassung:

Diese Arbeit beschreibt die Präparation eines einstellbaren Quantensystems bestehend aus wenigen Fermionen unter Verwendung von ultrakalten ^{6}Li Atomen in einer optischen Dipolfalle. Wir präparieren Systeme im Grundzustand bestehend aus 1 bis 10 Fermionen mit einer Präparationswahrscheinlichkeit von ∼90%. Unser System hat die einzigartige Eigenschaft, dass entscheidende Parameter wie Teilchenzahl, Wechselwirkungen zwischen den Teilchen sowie das äußere Fallenpotential einstellbar sind.

Wir verwenden dieses Modellsystem, um zwei wechselwirkende Atome in einem eindimensionalen Fallenpotential zu untersuchen. Bei zunehmender Abstoßung wird ein Abfall der Tunnelzeit eines Atoms durch eine Tunnelbarriere nachgewiesen, welche durch Kippen des Potentials erzeugt wird. Aus der gemessenen Tunnelzeit berechnen wir die Wechselwirkungsenergie des Systems unter Verwendung der WKB-Näherung. Dazu ist eine genaue Kenntnis des Fallenpotentials erforderlich. Dieses bestimmen wir, indem wir den Quantenzustand der Bewegung eines einzelnen Atoms in der Falle kontrollieren.

Um die Präparationswahrscheinlichkeit der Wenigteilchensysteme zu erhöhen wurde im Rahmen dieser Arbeit ein hochauflösendes Objektiv entwickelt. Dies wird uns ermöglichen, einstellbare Quantensysteme in zwei und drei Dimensionen in beliebigen Fallenpotentialen zu erforschen.

Aufgrund dieses hohen Maßes an Einstellbarkeit eignet sich unser System auf einzigartige Weise Systeme, die aus wenigen wechselwirkenden Fermionen bestehen, zu erforschen, welches eine der großen Herausforderungen der modernen Physik darstellt.

für Laurin & Julia

Contents

1 Introduction

It is the ambitious goal of fundamental research to look past the high diversity of nature to reveal its underlying structure. A prime example is the exploration of metals and nuclei. Although both systems show completely different physical properties, they follow common fundamental principles: Their constituents, electrons in metals and protons and neutron in nuclei, are fermions. These obey Pauli's principle, which states that each quantum state cannot be occupied by two or more identical fermions. This simple rule has the tremendous consequence to prevent matter from collapsing: in a metal, it forces electrons to fill up energy bands up to the Fermi energy and *not* condense into the lowest energy state.
A variety of phenomena could be successfully explained by extending this basis. An intriguing example is the superconductivity in metals which could be explained by the pairing of two fermions within the framework of BCS theory [Bar57]. Only one year later it has been suggested that pairing of fermions also leads to the gap which has been observed in the excitation spectrum of nuclei [Boh58]. The following application of BCS theory to nuclei allowed to explain a large variety of experimental observations in nuclear physics [Bel59]. Connecting those seemingly alien worlds is a prime example of successful fundamental research.
Scientific progress crucially depends on two aspects: both the development of theoretical models, which describe nature's behavior based on few simple principles, and the ability to manipulate key parameters and directly observe the system's response. However, theory and experiment, have fundamental limitations: One example is that the resources which are required to calculate the time evolution of a quantum many-body system scale exponentially with its size. Even for a moderate particle number this problem becomes intractable. On the experimental side many properties are set by fundamental constants and thus cannot be changed.
To overcome these limitations R. Feynman proposed a universal quantum simulator, a machine which is capable to simulate any given quantum system [Fey82]. How efficiently pairing in nuclei could be explored when the relevant parameter, i.e. interaction strength between the constituents, was tunable? So far, this has remained an experimentalist's dream.
To approach this goal, researchers created few-particle systems with tunable properties which they called 'artificial atoms'. The two most important realizations are quantum dots [Rei02] and atomic clusters [Hee93]. However, these systems are

generally coupled to their environment which makes the deterministic preparation of a well defined quantum state challenging.
During this thesis, a few-particle system with full control over the system's quantum state has been realized using ultracold atoms in an optical dipole trap [Ser11]. Since the key parameter, the inter-particle interaction, is directly tunable, this system is uniquely suited to simulate interacting few-fermion systems.
The thesis is structured in the following way. An overview over quantum dots and atomic clusters is presented. Their impact on fundamental research and technological applications is discussed as well as their limitations. This sets the stage for a summary of our approach of realizing an artificial atom using ultracold fermions. Chapter 3 introduces ultracold atoms as highly tunable quantum systems emphasizing the ability to tune inter-particle interactions and tailoring almost arbitrary confining potentials. The key technique to proceed from a macroscopic quantum system to the few-particle regime is the spilling technique, which is introduced in chapter 4. This technique can be used to probe the energy structure of the system as well, which is also explained in this chapter. Theoretical estimations of the bound states in a tilted potential and the corresponding experimental observables, i.e. the lifetimes of those states, are given both for a non-interacting system as well as for a system with two interacting particles. The experimental setup with emphasis on the key elements required to prepare and detect the few-body samples, the microtrap setup, is presented in chapter 5. A new level of tunability for future experiments can be reached with a high-resolution objective which has has been designed within the scope of this thesis. Its design goals and benefits are also presented in this chapter. Chapter 6 and 7 present the main experimental results of this thesis: the deterministic preparation of a tunable few-fermion system. While chapter 6 focuses on the preparation of non-interacting samples, chapter 7 can be seen as a first step towards quantum simulation of interacting few-fermion systems. This opens up a new playground for the exploration of a variety of interacting few-particle systems. Chapter 8 summarizes the results of this thesis and gives an outlook on some of the fascinating experiments that can be performed with the new model system.

2 Artificial atoms - Tunable mesoscopic quantum systems

Researchers created synthetic quantum systems which allowed them to tune the number of constituents, their mutual interactions and the external trapping potential. They called them 'artificial atoms' because of their ability to mimic properties of real atoms. Just as electrons in an atom, their constituents are fermions. Therefore each quantum state can be occupied with one particle according to Pauli's principle. This leads to the formation of a shell structure in their energy spectrum with the important consequence that the number of particles occupying the same energy shell determines the system's physical and chemical properties. The full spectrum is given by interactions between the constituents and the shape of the external potential.
Within the last decades mainly two types of artificial atoms have been developed: quantum dots and atomic clusters. Their development has had major impact not only on technological applications but also on the fundamental understanding of few-fermion systems.
This chapter gives a brief overview over the properties and possibilities of these systems as well as their limitations. It will set the stage for the introduction of our approach of realizing an artificial atom using ultracold fermionic atoms. An overview over few-electron quantum dots can be found in the review paper of Reimann et al. [Rei02] whereas for atomic clusters the review by de Heer et al. [Hee93] is recommended.

2.1 Atomic clusters

Atomic clusters are particles composed of 2 to 10^6 atoms which are typically prepared in molecular beam experiments. Individual cluster sizes are selected by mass spectrometry and ionized clusters are stored in ion traps [Wal09]. The transition from the solid-state to the few-particle regime was reached by [Kni84] where clusters consisting of 4 to 100 particles could be produced by vaporizing sodium. A surprising result was found in the mass spectrometry data of the sodium beam: for cluster sizes of $N = 8, 20, 40, 58, 92$ large peaks were found (figure 2.1) indicating

higher stability of these cluster sizes. These observations could be attributed to the electronic structure of the clusters which is determined by the valence electrons of the sodium atoms confined in the electrostatic potential of the ions.

2.1.1 Simple model

The energy spectra can be understood by means of the rather simple Jellium model. Its main assumption is that the positive charge of the ions is distributed uniformly over a sphere of the size of the cluster. Since the interactions of the valence electron with the background charge are incorporated into a spherically symmetric mean field potential the Schrödinger equation becomes effectively one-dimensional and can be solved [Bra93]. When a rounded potential well is assumed as mean field, the energy spectrum of the system yields closed shells which agree with stable cluster sizes observed in the experiment. When the number of atoms in the cluster and thus the number of available valence electrons becomes a magic number of this potential, a shell is filled and the stability of the cluster is enhanced.

2.1.2 Prospects and challenges

The main tuning parameters of the system are the number of atoms in the cluster and the electronic structure of those atoms. This tunability allowed the field to proceed towards controlled engineering of clusters to design new materials with well defined electronic structure. A recent review can found in [Cas09]. These synthetic systems called 'Superatoms' are able to mimic chemical properties of real atoms in the periodic table. An intriguing example is the $Al_{13}-$ cluster consisting of 13 aluminum atoms and 40 valence-electrons. It has a filled shell of valence electrons which makes it chemically inert similar to noble gases. By exchanging only one atom the cluster's outermost shell opens and the system can be made reactive. These experiments open the door to chemistry at a fundamental level.
The tunability of these systems leads to important technical applications. One example is the preparation of a 'designer magnetic superatom' [Rev09], an atomic cluster with tunable magnetic properties. The prospect of these systems is to engineer semiconductors with a tunable band gap which has been a long-standing goal in applied solid state physics.
While researchers are able to create a variety of clusters which differ in the number of constituents and electronic structure, the size of the cluster cannot be varied at will. In particular, the size is limited to stable configurations of those self-organized systems. Furthermore the inter-particle interaction cannot be tuned directly because it is dominated by Coulomb repulsion of the charged electrons.

Also the confining potential can be tuned only indirectly via the cluster size and the choice of buffer gas.

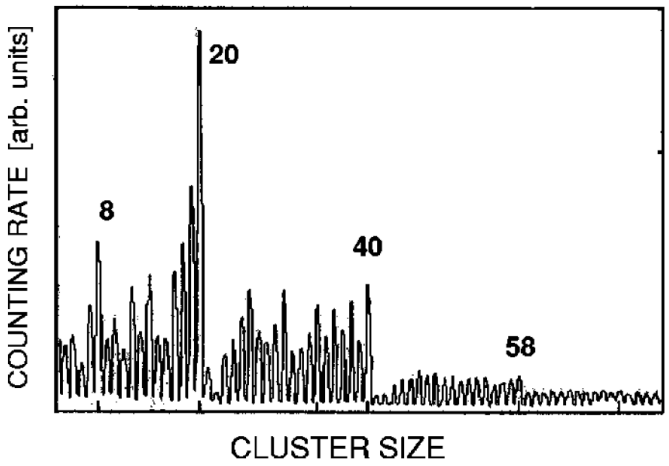

Figure 2.1: Abundance spectra of metallic clusters. Stable clusters with $N = 8, 20, 40, 58...$ atoms correspond to magic numbers of the potential. From [Kni84].

2.2 Quantum dots

To obtain quantum systems whose properties could be manipulated in a simple way by applying external fields, researchers created quantum dots, micro-fabricated structures on semiconductor devices. By etching appropriate geometries onto the surface and applying electrostatic fields, custom confining potentials for electrons in the conduction band can be created.

2.2.1 Simple model

For most quantum dots the confining potential is well described by a two-dimensional harmonic oscillator

$$V(\boldsymbol{r}) = \frac{1}{2} m^* \omega_0^2 \left(x^2 + y^2\right) + V(z). \tag{2.1}$$

where m^* is the effective electron mass and ω_0 the trapping frequency. The effective mass is used to account for Coulomb interaction with charges present in the environment such as valence and core electrons of the material. The Hamiltonian

can be written as

$$H = H_0 + H_{\text{int}} = \sum_i^N \left(\frac{\boldsymbol{p}_i^2}{2m^*} + V(\boldsymbol{r}_i) \right) + \frac{1}{2} \sum_{i<j}^N \frac{e^2}{4\pi\epsilon\epsilon_0 \left| \boldsymbol{r}_i - \boldsymbol{r}_j \right|} \tag{2.2}$$

where ϵ is the dielectric constant of the host semiconductor [Ron06]. For $N > 2$ the eigenfunctions of the Hamiltonian cannot be calculated analytically. However the solution for a non-interacting system with Hamiltonian H_0 can be obtained analytically. The energies are given as

$$E_{n,l} = (2n + |l| + 1)\, \hbar\omega_0 \tag{2.3}$$

with radial quantum number $n = (0, 1, 2...)$ and angular momentum quantum number $l = (0, \pm 1, \pm 2, ...)$. The energy levels are d-fold degenerate where d is given by $d = 2n + |l| + 1$.
In particular, the ground state with quantum numbers $(n, l) = (0, 0)$ is 1-fold degenerate. Therefore, the shell can host two electrons with opposite spin. The second excited state with energy $E_{(0,-1)}$ is degenerate with state $E_{(0,1)}$. This shell can be occupied by 4 electrons. The third shell with an energy of $E_{(0,-2)} = E_{(1,0)} = E_{(0,2)}$ can host 6 electrons in total. This leads to magic numbers of the potential $N = 2, 6, 12....$

2.2.2 Tunability

One of the most appealing features of quantum dots is that they can be manipulated and probed by simply applying external electric and magnetic fields.
With a magnetic field applied in the z-direction the effective trapping frequency ω_B of the potential can be tuned as

$$\omega_B^2 = \omega_0^2 + \frac{1}{4}\omega_c^2 \tag{2.4}$$

where $\omega_c = \frac{eB}{m^*}$ is the the cyclotron frequency of the electron.
When a voltage is applied to the reservoir, the energy of electrons located in the reservoir with respect to the energy of electrons in the dot can be controlled. By increasing the voltage electrons from the reservoir can tunnel onto the dot. If there already is an electron on the dot the second electron has to overcome the coulomb blockade to tunnel onto the dot. Therefore the minimum voltage increase leading to another electron on the dot is at least $\Delta U = e/C$ with the dot's capacitance C. The energy cost of adding further electrons and thus the applied voltage depends on the configuration of electrons already in the dot. For adding an electron to a closed shell not only the Coulomb blockade but also the energy difference between

the closed shell and the next shell has to be supplied. The energy spectrum of the system can be probed simply by counting the number of electrons on the dot with increasing gate voltage. In a key experiment the number of electrons could be reduced so far that the regime of few-body quantum physics could be reached [Tar96]. A measured spectrum of electrons and the corresponding shell structure is shown in figure 2.2 taken from a review article on quantum dots [Kou01]. When $N = 2, 6, 12$ electrons are present the energy cost for adding a further electron has a maximum. This corresponds to filled shells of the energy spectrum of the Hamiltonian H_0 from equation 2.2.

2.2.3 Prospects and challenges

Because the electronic structure of quantum dots can be manipulated and they are part of semiconductor devices these systems have a variety of technical applications. For example they can serve as a light source with tunable wavelength.
However, the main challenge in preparing few-body quantum systems is to prepare the quantum state in a reproducible way. The limiting factor is the coupling of the systems to its environment. For quantum dots this problem becomes significant because of several coupling mechanisms. A summary of the relevant effects can be found in [Her02]. In different quantum dots optical excitons (electron-hole pairs) show different emission energy due to electric charges in the materials which are hard to control. Furthermore electron-phonon coupling leads to fast dephasing and decoherence of excited states. One approach to avoid coupling to optical phonons which is one of the major decoherence processes is to cool quantum dots down to temperatures of $T = 6\,\mathrm{K}$. Using cooling techniques the decoherence times could be extended by three orders of magnitude to a few hundred picoseconds.
Recently carbon nanotube quantum dots could be engineered [Ste09] which provide a clean environment eliminating major decoherence effects. In such a system a double well potential with tunable coupling between two dots was realized. Using clean gate materials the coherence times are expected to be long enough to use the system for quantum information processing.

To summarize, both quantum dots and atomic clusters provide systems with widely tunable properties. However they are coupled to their environment which makes the deterministic preparation of the system's quantum state challenging. Furthermore, the inter-particle interaction and the confining potential cannot be tuned independently.

2.3 Ultracold atoms

Ultracold neutral atoms are typically cooled to a temperature on the order of $T = 1\mu\text{K}$ which corresponds to a de Broglie wavelength of

$$\lambda = (2\pi\hbar^2/mk_BT)^{1/2} \approx 1\mu\text{m} \tag{2.5}$$

where m is the particle mass. This large value of the de Broglie wavelength is the origin of the system's tunability and allows to control its quantum state. Since this will be described within this thesis in detail a brief overview is given here.

2.3.1 Tunability

The de Broglie wavelength is much larger than the characteristic range of the van-der-Waals potential which determines interactions between two neutral particles. As a consequence the wavelength of the relative wave function of two colliding atoms becomes to large to resolve the fine details of the scattering potential. Therefore the description of the scattering process can be abstracted from the true scattering potential to a new simplified layer as discussed in chapter 3.1. In particular the interactions between to atoms with spatial coordinates $\boldsymbol{r}_1, \boldsymbol{r}_2$ can be simply written as a delta function

$$V_{\text{int}}(\boldsymbol{r}_1, \boldsymbol{r}_2) = g \cdot \delta(\boldsymbol{r}_1 - \boldsymbol{r}_2). \tag{2.6}$$

where g is the coupling strength. Because g depends only on one parameter, the s-wave scattering length a via

$$g = \frac{4\pi\hbar^2}{m}a \tag{2.7}$$

and we can tune a by means of a Feshbach resonance as discussed in chapter 3.1, we can realize coupling strengths with any value between

$$-\infty < g < \infty. \tag{2.8}$$

The possibility to directly tune interactions between two particles and the fact that interactions can be described in the most simple way makes ultracold atoms uniquely suited to explore interacting many-body systems. Furthermore almost arbitrary external potentials can be realized utilizing optical dipole traps as described in chapter 3.2. With those degrees of freedom a variety of Hamiltonians has been explored in the laboratory reviewed in [Blo08].

2.3.2 Control over the quantum state

Since the de Broglie wavelength becomes comparable to the inter-particle distance, properties of the system are governed by the quantum statistics of its constituents. Bosonic atoms follow Bose-Einstein statistics: they condense into the lowest energy state to form a Bose-Einstein condensate which has been realized experimentally in 1995 [And95, Bra95, Dav95].
Since the behavior of fermionic atoms is dictated by Fermi-Dirac statistics and Pauli's principle one energy state is occupied with one fermionic atom per spin state and consequently, they form a degenerate Fermi gas [DeM99].
In such a degenerate Fermi gas, the occupation probability for the lowest energy states approaches unity. Because of this characteristic property we can use a degenerate Fermi gas as a starting point to proceed from the macroscopic to the few-particle limit. As the lowest energy states are occupied with one fermionic atom per spin state with high probability, we obtain control over the number of particles by controlling the number of occupied quantum states. Our approach, the spilling technique, is to choose the occupied quantum states by tilting the confining potential in such a way that only a well defined number of states remains bound. The ability to select those bound states with single state precision allows us to gain complete control over the final system's quantum state as we will show in chapter 6.

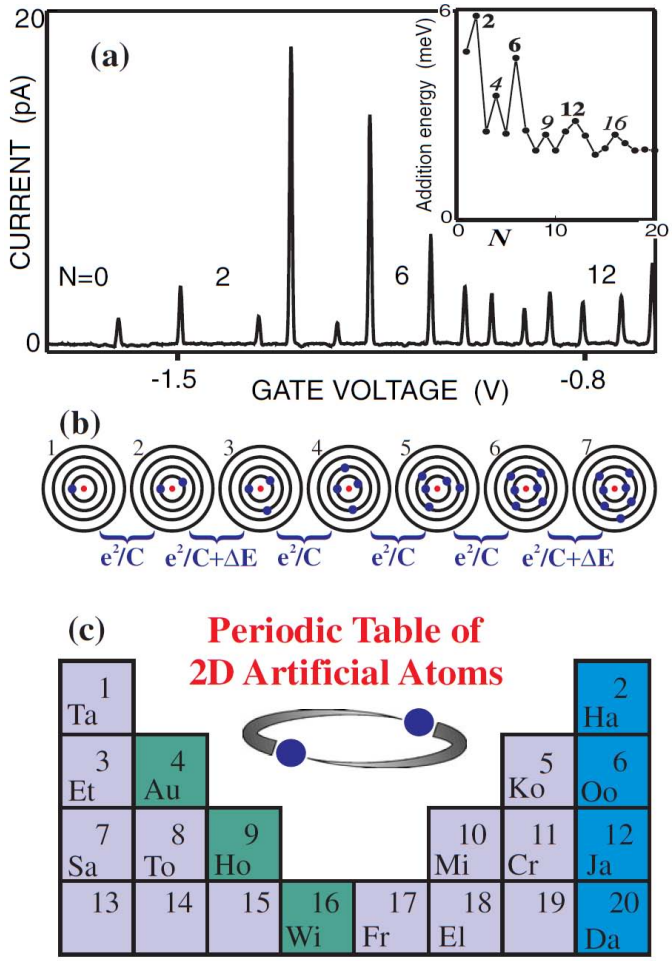

Figure 2.2: Few-electron quantum dots. By increasing the gate voltage electrons can tunnel onto the dot (a). The distance between the peaks reveals the shell structure of the energy spectrum. To open up a new shell a higher voltage increase is required. When the gate voltage is increased by $U = e/C$ where C is the dot's capacitance, an additional electron can tunnel onto an unfilled shell (b). One shell can host $N = 2, 6, 12, 20$ particles corresponding to the magic numbers of a two-dimensional harmonic oscillator potential. Adding an electron to a closed shell requires additional energy ΔE in analogy to noble gases (c). From [Kou01].

3 Ultracold atoms – highly tunable quantum systems

Ultracold gases have the great advantage that they are well isolated from the environment. With this degree of isolation the system is even suited to perform precision measurement of time competing with state of the art techniques [Tak05]. Furthermore, interaction between the particles can be tuned directly and almost arbitrary confining potentials can be realized. Because these degrees of freedom can be tuned independently these systems provide the unique possibility to explore Hamiltonians of a general form

$$H = T + V_{\text{int}} + V_{\text{ext}} \tag{3.1}$$

where T is the kinetic energy, V_{int} the interaction energy and V_{ext} the energy due to an external potential. A comprehensive overview over systems which have been realized using ultracold fermions and bosons can be found in the review papers [Blo08, Ket08].

3.1 Tuning interactions

A major advantage of ultracold atom systems is that interactions between two particles can be described in the simplest possible form

$$V_{\text{int}}(\boldsymbol{r}_1, \boldsymbol{r}_2) = g \cdot \delta(\boldsymbol{r}_1 - \boldsymbol{r}_2) \tag{3.2}$$

where g is the coupling strength which can be tuned in the experiment to any value between

$$-\infty \leq g \leq \infty \tag{3.3}$$

In the following section relation 3.2 will be derived and it will be explained how g can be tuned simply by applying an external magnetic field.
As an introduction basic concepts of quantum mechanical scattering theory are revisited following [Dal98, Sch07, Zwi06].

3.1.1 Ultracold scattering

The physics of two interacting particles with coordinates $\boldsymbol{r}_1$ and $\boldsymbol{r}_2$ and mass m is described by the total wave function ψ_{sc} of the system as the stationary solution of the Schrödinger equation

$$H\psi_{sc}(\boldsymbol{r}_1, \boldsymbol{r}_2) = E\psi_{sc}(\boldsymbol{r}_1, \boldsymbol{r}_2) \tag{3.4}$$

with Hamiltonian

$$H = -\frac{\hbar^2}{2m}\nabla_1^2 - \frac{\hbar^2}{2m}\nabla_1^2 + V_{\text{ext}}(\boldsymbol{r}_1) + V_{\text{ext}}(\boldsymbol{r}_2) + V_{\text{int}}(\boldsymbol{r}_1 - \boldsymbol{r}_2). \tag{3.5}$$

When the characteristic length scale of the external confinement x_0 is much larger than the range of the interaction potential r_0 the external confinement can be neglected ($V_{\text{ext}}(\boldsymbol{r}_1) = V_{\text{ext}}(\boldsymbol{r}_2) = 0$). The scenario of potentials with confinement strong enough to modify the interaction between the particles is treated in chapter 4.3.

General solution for a spherically symmetric potential

For a spherically symmetric potential the wave function separates into a term depending on the relative coordinate

$$\boldsymbol{r} = \boldsymbol{r}_1 - \boldsymbol{r}_2 \tag{3.6}$$

and a term depending on the center-of-mass coordinate

$$\boldsymbol{R} = (\boldsymbol{r}_1 + \boldsymbol{r}_2)/2 \tag{3.7}$$

of the particles:

$$\psi_{sc}(\boldsymbol{r}_1, \boldsymbol{r}_2) = \psi_R(\boldsymbol{R})\psi_r(\boldsymbol{r}). \tag{3.8}$$

The center-of-mass solution is given by a plane wave

$$\psi_R(\boldsymbol{R}) \sim e^{i\boldsymbol{k}\cdot\boldsymbol{R}} \tag{3.9}$$

with wave vector $\boldsymbol{k}$. This just adds an offset to the system's total energy

$$E = E_R + E_r \tag{3.10}$$

The equation in the relative coordinate $\boldsymbol{r}$ becomes

$$\left(-\frac{\hbar^2}{2\mu}\nabla_{\boldsymbol{r}}^2 + V_{\text{int}}(\boldsymbol{r})\right)\psi_r(\boldsymbol{r}) = E_r\psi_r(\boldsymbol{r}) \tag{3.11}$$

where $\mu = m/2$ denotes the reduced mass. The solution far away from the scattering potential is given by the sum of an incoming plane wave and an outgoing spherical wave

$$\psi_r(\boldsymbol{r}) \sim e^{i\boldsymbol{k}\boldsymbol{r}} + f(\boldsymbol{k}', \boldsymbol{k})\frac{e^{i\,kr}}{r} \tag{3.12}$$

where $\boldsymbol{k}$ is the direction of the incoming plane wave and $\boldsymbol{k}'$ the direction of observation. The physics of the scattering process is contained in the scattering amplitude defined as

$$f(\boldsymbol{k}', \boldsymbol{k}) = -\frac{\mu}{2\pi\hbar^2}\int e^{-i\boldsymbol{k}'\boldsymbol{r}'}V(\boldsymbol{r}')\psi_r(\boldsymbol{r}')\,d^3r'. \tag{3.13}$$

Equation 3.13 is important because it relates the wave function far away from the potential determined by the scattering amplitude (left hand side) with its values inside the potential $\psi_r(\boldsymbol{r}')$ (right hand side). If $\psi_r(\boldsymbol{r}')$ was known for all $\boldsymbol{r}'$, the problem would be solved.

Scattering amplitude for ultracold collisions

Now the advantage of ultracold atoms comes into play: A simple expression for the scattering amplitude (left hand side of equation 3.13) can be found without knowing the details of the potential $V(\boldsymbol{r}')$ (right hand side of equation 3.13). This is possible because the atoms collide at low momentum $\boldsymbol{k}$. Therefore their de Broglie wavelength $\lambda \sim \frac{1}{k}$ is much longer than the range of the interaction potential r_0. As a consequence the wave function of the atoms does not resolve the fine details of the potential.
To obtain an expression for the scattering amplitude the symmetry of the problem can be used. Because of the spherically symmetric scattering potential, the scattered wave 3.12 must be axially symmetric with respect to the wave vector of the incident plane wave $\boldsymbol{k}$. Then, the incoming plane wave and scattered wave can be expanded into partial waves with angular momentum quantum number l

$$\psi_r(\boldsymbol{r}) = \sum_{l=0}^{\infty} P_l(cos(\theta))R_{k,l}(r) \tag{3.14}$$

where $P_l(cos(\theta))$ are the Legendre polynomials and θ denotes the angle between $\boldsymbol{k}$ and $\boldsymbol{k}'$. The radial functions $R_{k,l}(r)$ can be found solving the Schrödinger equation for the radial degree of freedom

$$u''_{k,l}(r) + \left(k^2 - \frac{l(l+1)}{r^2} - \frac{2\,\mu\,V(r)}{\hbar^2}\right)\,u_{k,l}(r) = 0 \tag{3.15}$$

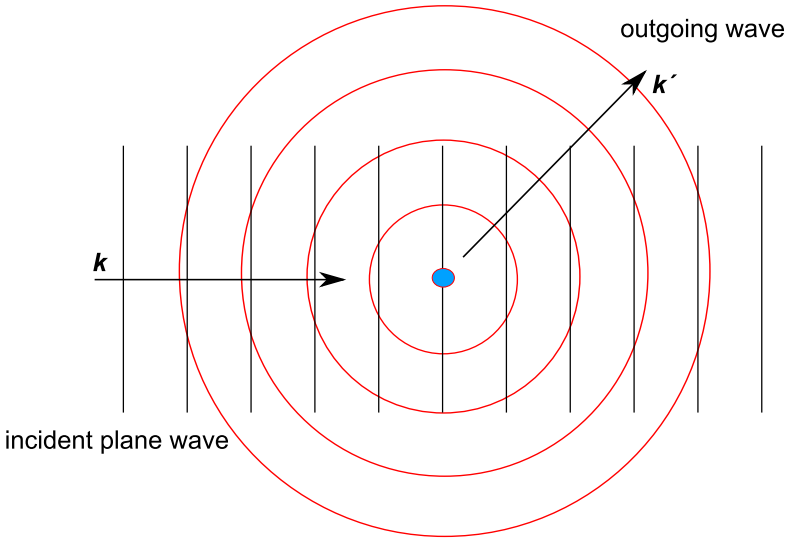

Figure 3.1: Quantum mechanical scattering. Far away from the scattering potential the relative wave function ψ_r is a superposition of incident plane wave and outgoing spherical wave. For two ultracold atoms their scattering process can be described in a very simple form for two reasons. Because the de Broglie wavelength exceeds the characteristic length scale of the scattering potential (blue), the wave function does not resolve its fine details. Therefore the true scattering potential can be replaced by a much simpler description. And as the momentum of the colliding particles is low, collisions only take place at zero angular momentum. In this case the scattered wave function is simply spherically symmetric with amplitude a/r where a is the s-wave scattering length.

where $R_{k,l}(r) = \frac{u_{k,l}(r)}{r}$. Far away from the potential they behave like

$$R_{k,l}(r) \sim \frac{1}{r} \sin\left(r - l\frac{\pi}{2} + \delta_l\right). \tag{3.16}$$

If only the incident plane wave is expanded the radial functions $R_{k,l}(r)$ have the same form but no phase shift $\delta_l = 0$. Therefore, the effect of the scattering potential on the incoming wave is simply to add a phase shift of δ_l to each incoming wave with angular momentum l.

Inserting the expanded wave function 3.14 into the equation 3.12 one finds for the scattering amplitude

$$f(k,\theta) = \frac{1}{2ik} \sum_{l=0}^{\infty} (2l+1)\left(e^{2i\delta_l} - 1\right) P_l(\cos(\theta)). \tag{3.17}$$

For ultracold collisions the energy of the colliding atoms is too low to overcome the centrifugal barrier set by the $(l\,(l+1))/r^2$ term in equation 3.15 for $l > 0$. This barrier reflects these partial waves such that they cannot come close enough to be disturbed by the actual inter-atomic potential. Therefore only s-waves probe the interaction potential. This simplifies the expression for the scattering amplitude 3.17 to

$$f_{l=0} = \frac{1}{2ik}\left(e^{2i\delta_0} - 1\right) = \frac{1}{k\cot\delta_0 - ik} \tag{3.18}$$

where δ_0 is the s-wave phase shift. In the limit of low momentum collisions

$$k \ll \frac{1}{r_0}, \tag{3.19}$$

where r_0 denotes the van-der-Waals length of the potential, the term in the denominator of 3.18 can be expanded as

$$k\cot\delta_0 \approx -\frac{1}{a} + r_{\text{eff}}\frac{k^2}{2} \tag{3.20}$$

where the s-wave scattering length is defined as

$$a = -\lim_{k\ll 1/r_0}\frac{\tan\delta(k)}{k} \tag{3.21}$$

and r_{eff} denotes the effective range of the scattering potential. For a van-der-Waals potential the effective range is on the same order as r_0.
Using equation 3.20 the scattering amplitude 3.18 can be rewritten as

$$f(k) = -\frac{1}{-\frac{1}{a} + r_{\text{eff}}\frac{k^2}{2} - ik} \tag{3.22}$$

When the de Broglie wavelength of the particles exceeds the range of the potential, i.e. in the limit $r_{\text{eff}} \ll 1/k$, the expression for the s-wave scattering amplitude becomes

$$f(k) = -\frac{a}{1 + ika} \tag{3.23}$$

In the limit $k\,|a| \ll 1$ the scattering amplitude is simply given as

$$f = -a \tag{3.24}$$

In this case the outgoing wave solution becomes particularly simple: spherically symmetric as indicated in figure 3.1

$$\psi_r(\boldsymbol{r}) \sim e^{i\boldsymbol{k}\boldsymbol{r}} - \frac{a}{r}e^{i\,kr} \tag{3.25}$$

and all the physics is described by a one parameter, the scattering length a.

Scattering cross sections

Experimentally observable quantities of the scattering process such as the differential and total cross section can be directly obtained from the scattering amplitude. The differential cross section is given by

$$\frac{d\sigma}{d\Omega} = \left| f\left(\boldsymbol{k}', \boldsymbol{k}\right)\right|^2 \tag{3.26}$$

and the total cross section

$$\sigma = \int d^3k' \left| f\left(\boldsymbol{k}', \boldsymbol{k}\right)\right|^2 \tag{3.27}$$

For distinguishable particles the cross section can be found integrating equation 3.17

$$\sigma_d(k) = \frac{4\pi}{k^2} \sum_{l=0}^{\infty} (2l+1) \sin^2 \delta_l. \tag{3.28}$$

For non-distinguishable particles the cross section crucially depends on whether the particles are bosons or fermions. Under exchange of two non-distinguishable particles the final state remains the same. This leads to two possible pathways resulting in the same final state which can interfere.
For bosons the pathways show constructive interference leading to an enhancement of the cross section

$$\sigma(k) = 2 \cdot \sigma_d(k), \tag{3.29}$$

whereas for fermions the interference is destructive. This has the important consequence that the cross section for $l = 0$ vanishes for identical fermions

$$\sigma(k) = 0. \tag{3.30}$$

To overcome this limitation fermions in different hyperfine states can be used. Because they are distinguishable their cross section is given by $\sigma_d(k)$.
In the low momentum limit $k \cdot |a| \ll 1$ the cross section is obtained by integrating equation 3.24 and can be summarized as

$$\sigma = \begin{cases} 0 & \text{identical fermions} \\ 4\pi a^2 & \text{distinguishable particles} \\ 8\pi a^2 & \text{identical bosons.} \end{cases} \tag{3.31}$$

A simple expression for the scattering potential

Starting from the exact expression for the scattering amplitude as given in equation 3.13

$$f(\boldsymbol{k}', \boldsymbol{k}) = -\frac{\mu}{2\pi\hbar^2} \int d^3r' e^{-i\boldsymbol{k}'\boldsymbol{r}'} V(\boldsymbol{r}') \psi_r(\boldsymbol{r}')$$

we found a simple expression for the left hand side using the fact that ultracold atoms collide at low momenta k. This solution was found without evaluating the right hand side of equation 3.13. Any potential $V(\boldsymbol{r})$ yielding the right scattering amplitude 3.24 in the low momentum limit would be a valid description for the problem. To be able to evaluate the integral although the exact wave function inside the potential $\psi_r(\boldsymbol{r'})$ is not known one can approximate it with a plane wave

$$\psi_r(\boldsymbol{r'}) = e^{i\boldsymbol{k}\cdot\boldsymbol{r'}}. \tag{3.32}$$

This is the first Born approximation. The scattering amplitude simplifies to

$$f(\boldsymbol{k'}, \boldsymbol{k}) = -\frac{\mu}{2\pi\hbar^2}\int d^3r' e^{-i(\boldsymbol{k}-\boldsymbol{k'})\cdot\boldsymbol{r'}}\, V(\boldsymbol{r'}) = -\frac{\mu}{2\pi\hbar^2}\tilde{v}(\boldsymbol{k'}-\boldsymbol{k}) \tag{3.33}$$

Therefore the scattering amplitude is just the Fourier transform of the potential. When the point like interaction potential

$$V_{\text{int}}(\boldsymbol{r}_1, \boldsymbol{r}_2) = g \cdot \delta(\boldsymbol{r}_1 - \boldsymbol{r}_2) \tag{3.34}$$

is plugged into equation 3.33 the scattering amplitude in the Born approximation becomes

$$f_{\text{Born}} = -\frac{m}{2\cdot 2\pi\hbar^2} g \tag{3.35}$$

It yields the right scattering amplitude in the limit of low momentum

$$f = -a \tag{3.36}$$

if

$$V_{\text{int}}(\boldsymbol{r}_1, \boldsymbol{r}_2) = g \cdot \delta(\boldsymbol{r}_1 - \boldsymbol{r}_2) = \frac{4\pi\hbar^2}{m}\, a\, \delta\left(\boldsymbol{r}_1 - \boldsymbol{r}_2\right) \tag{3.37}$$

Therefore a delta-potential where the coupling strength g is proportional to the s-wave scattering length is an appropriate description of the scattering process at low momenta.

Although the Born approximation for the delta-potential yields the right scattering amplitude in the low momentum limit, the higher order terms in the Born series diverge because the Fourier transform of the potential does not fall off for large momenta [Ket08]. However this is only a theoretical problem since every physical potential falls off at some momentum. To overcome this problem the diverging terms can be balanced by replacing g with

$$g = \left(\frac{m}{4\pi\hbar^2 a} - \frac{m}{\hbar^2}\int \frac{d^3q}{(2\pi)^3}\frac{1}{q^2}\right)^{-1} \tag{3.38}$$

in the calculation. However for the relevant regime of low momentum the Fourier transform of the delta potential given by equation 3.37 provides a valid description of the interaction strength.

Scattering resonance

In this section we will see how the s-wave scattering length a and thus the coupling strength g can be tuned. To get an intuitive picture on can consider scattering on a repulsive spherical potential well as indicated in figure 3.2. According to equa-

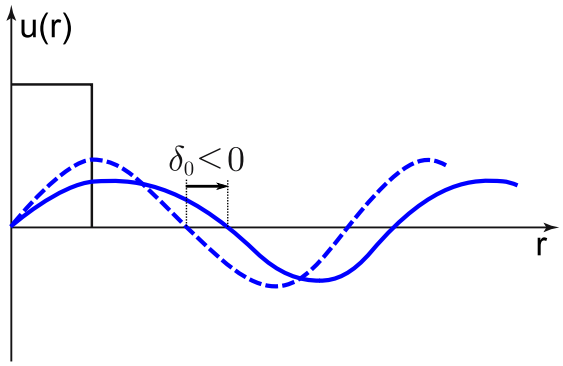

Figure 3.2: Scattering length for a repulsive box potential. The potential causes a negative phase shift δ_0 of the asymptotic solution of the perturbed wave with respect to the unperturbed solution (dashed line). Therefore the wave function gets pushed out of the center. Because $\delta_0 \sim -a$ for small δ_0 the scattering length a can be tuned by increasing the height of the barrier.

tion 3.21, the scattering length is proportional to the relative phase shift of the asymptotic wave function with and without scattering potential for small values of δ_0. In this picture the perturbed solution acquires a negative phase shift with respect to the unperturbed wave (dashed line) leading to $a > 0$. This phase shift pushes the wave function out of the potential. By increasing the potential height, a can be increased.
The full tunability of a arises when a bound state is available in an attractive potential as shown in figure 3.3. Here the influence of the potential on the asymptotic wave function is shown when the well gets deeper. When no bound state exists the wave function acquires a positive phase shift ($a < 0$) due to the potential. When the potential becomes deeper such that a bound state occurs at zero energy, the phase shift becomes $\delta_0 = \pi/2$ which leads to a divergence of the scattering length $a \to -\infty$ according to equation 3.21. When the potential is made slightly deeper the phase shift exceeds $\pi/2$. Therefore the scattering length changes sign ($a > 0$). For finite binding energy the scattering length becomes finite again. By shifting the energy E_0 of the bound state with the potential depth, the value of a can be tuned between $-\infty < a < \infty$.

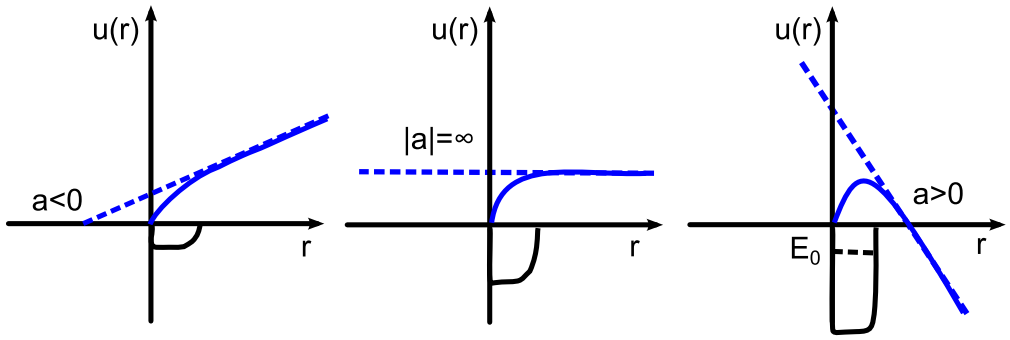

Figure 3.3: Scattering length a for a potential without bound state, with bound state at $E_0 = 0$ and with bound state at finite energy. The radial solution $u(r)$ for the Schrödinger equation outside the potential (solid line) is extrapolated to small values of r (dashed line). The scattering length is the point where the extrapolation crosses the x-axis. Its value can be tuned to $-\infty < a < \infty$ by shifting the energy E_0 of the bound state with the potential depth.

3.1.2 Tuning interactions between ultracold atoms

Feshbach resonances

For ultracold atoms this simple picture of changing the depth of the scattering potential until a bound state becomes degenerate with $E_0 = 0$ cannot be applied directly. Instead there is a bound state whose energy can be tuned with respect to the energy of the colliding atoms. The result on the scattering length is effectively the same. This phenomenon is called a Feshbach resonance and can be described in the following way: Because of the internal degrees of freedom of the colliding atoms such as their spin, different scattering channels exist as indicated in figure 3.4. The open scattering channel represents the potential curve for a collision of atoms with anti-aligned spin, i.e. a singlet configuration, with total spin 0. Therefore the system has negligible net magnetic moment. There also exists a closed scattering channel corresponding to parallel spins of the colliding atoms, i.e. triplet configuration, which results in a net magnetic moment of the system. When a magnetic field B is applied, the potential curve of the closed channel can be shifted in energy by an amount of

$$\Delta E = \Delta\mu \times B. \tag{3.39}$$

where $\Delta\mu$ is the difference in magnetic moment between systems in the two scattering channels. By tuning the magnetic field the energy difference between the two channels can be tuned. In particular a bound state of the closed channel can

be made degenerate with the energy of the incident atoms. Far away from the collision center there is negligible coupling between singlet and triplet channel because good quantum numbers are the total electronic spin $\mathbf{S} = \mathbf{s}_1 + \mathbf{s}_2$ and the total nuclear spin $\mathbf{I} = \mathbf{i}_1 + \mathbf{i}_2$. Therefore the wave function of electronic triplet and singlet configuration have vanishing overlap. The situation changes when the atoms come close to each other. At short distances the following part of the hyperfine interaction leads to a coupling of open and closed channel [Moe95]

$$V_{\mathrm{hf}} \propto (\mathbf{s}_1 - \mathbf{s}_2) \cdot (\mathbf{i}_1 - \mathbf{i}_2)\,. \tag{3.40}$$

Then the closed channel bound state becomes available to the colliding atoms which leads to a divergence of the scattering length according to

$$a = a_{\mathrm{bg}} \left(1 - \frac{\Delta B}{B - B_0}\right) \tag{3.41}$$

where a_{bg} is the background scattering length, B_0 is the magnetic field where the bound state becomes resonant and ΔB is the width of the resonance. When the bound state is tuned slightly above resonance ($B > B_0$), the scattering length a becomes infinitely negative. For $B < B_0$ the scattering length becomes positive.

^{6}Li as an ideal candidate

A ^{6}Li nucleus is composed of three protons and three neutrons. Therefore its nuclear spin amounts to $I = 1$ whereas its electronic spin is determined by the single valence electron to $S = 1/2$. At large magnetic fields $B > 100\,\mathrm{Gauss}$, nuclear spin and electronic spin decouple. Therefore the total angular momentum quantum number $F = I + S$ is not a good quantum number in this regime. Instead the six non-degenerate energy states of the ground state are split into two groups according to their z-component of their electronic spin as shown in figure 3.5. Since only the three lowest states in the $m_{\mathrm{S}} = -1/2$ manifold are stable against dipolar relaxation which causes atom loss, we only work with those in the experiment. According to figure 3.5 we label these states $|1\rangle$,$|2\rangle$ and $|3\rangle$. To prepare few-fermion samples we use a two-component mixture of atoms in state $|1\rangle$ and $|2\rangle$. In principle other combinations are possible.
The behavior of the scattering length between possible combinations of atoms in state $|1\rangle$,$|2\rangle$ and $|3\rangle$ is shown in figure 3.6. The broadness of the Feshbach resonance ($\Delta B \approx 300\,\mathrm{Gauss}$) has the main advantage that the interaction can be controlled more precisely given a limited accuracy of control over the magnetic field. Because the width is more than two orders of magnitude larger compared to other fermionic species [Chi10], ^{6}Li is the ideal species to prepare interacting few-particle systems.

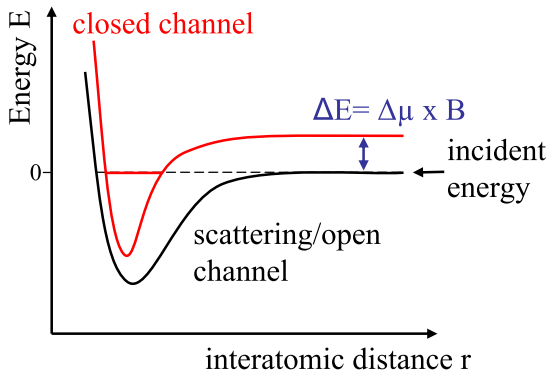

Figure 3.4: Principle of a Feshbach resonance. Two free atoms with total spin zero collide in an open scattering channel (black line) which represents the total potential energy depending on the relative distance between the atoms. There is also a closed scattering channel with non-zero total spin. This channel has an energy offset due to its magnetic moment which is proportional to the magnetic field. Because this offset can be tuned the bound state in the closed channel can be made degenerate with the incident energy of the colliding atoms. Associated with this bound state is a divergence of the scattering length (see figure 3.6). From [Ott10].

3.2 Tailoring confining potentials

Utilizing optical dipole traps an almost arbitrary potential landscape can be realized. Here the basic concepts for this are summarized following [Gri00]. When an electric field $\boldsymbol{E}$ oscillating with frequency ω, such as the light field, acts on a neutral atom it induces an electric dipole moment

$$\boldsymbol{p} = \alpha\, \boldsymbol{E} \tag{3.42}$$

where α is the complex polarizability. Because this electric dipole moment interacts with the light field the atom has a potential energy of

$$U_{\text{dip}} = -1/2\, \langle \boldsymbol{p}\, \boldsymbol{E} \rangle \propto -\text{Re}\,(\alpha)\, |E|^2 \,. \tag{3.43}$$

Therefore the potential energy is proportional to the intensity $I \propto |E|^2$ of the oscillating field.
This is the key relationship which allows to realize any external potential term V_{ext} in the Hamiltonian 3.1 by means of a spatially varying intensity distribution of light

$$V_{\text{ext}}(\boldsymbol{r}) \propto I(\boldsymbol{r}) \tag{3.44}$$

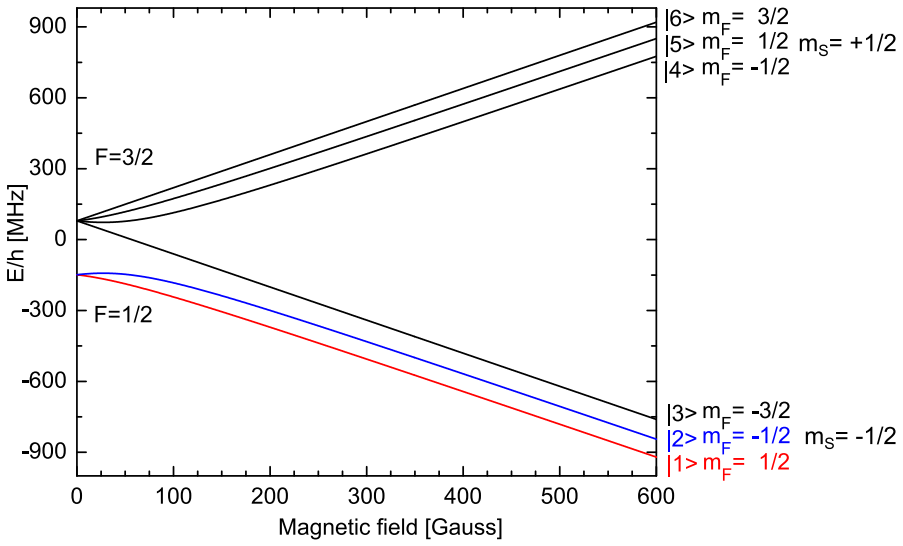

Figure 3.5: Zeeman hyperfine levels of the electronic ground state of ^{6}Li. Our few-fermion system is composed of atoms in states $|1\rangle$ and $|2\rangle$. Interactions between atoms in these two states can be tuned via a Feshbach resonance as shown in figure 3.6.

Taking into account the frequency dependence of α and damping due to spontaneous emission, the full expression for the dipole potential for large detunings and negligible saturation can be written as [Gri00]

$$U_{\mathrm{dip}}(\boldsymbol{r}) = -\frac{3\,\pi\,c^2}{2\,\omega_0^3}\left(\frac{\Gamma}{\omega_0-\omega}+\frac{\Gamma}{\omega_0+\omega}\right) I(\boldsymbol{r}) \tag{3.45}$$

where ω_0 is the frequency of the atomic transition, and Γ is its spontaneous decay width. When the frequency of the laser ω is lower than the atomic transition frequency ω_0, the oscillating dipole moment of the atom is able to follow the electric field of the laser. Therefore the induced dipole oscillates in phase with the light field (blue detuned dipole trap). In this case, the potential energy given by equation 3.43 is minimized for low light intensities. Therefore the potential becomes repulsive for increasing light intensities.
In the case of red detuning ($\omega > \omega_0$), the dipole moment of the atom cannot follow the oscillation of the light field. Therefore the dipole moment is oriented antiparallel with respect to the electric field. The corresponding potential becomes attractive for increasing light intensities.
In the simplest case the potential is created by a red-detuned focused Gaussian laser beam propagating along the z-direction. Its intensity distribution can be

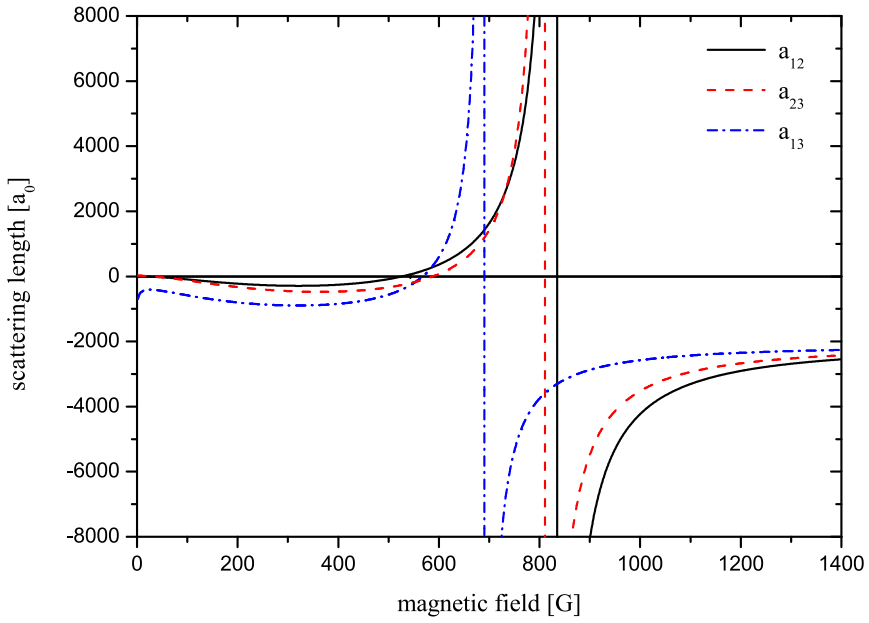

Figure 3.6: Scattering length as a function of magnetic field between the three lowest hyperfine states of ^{6}Li. From [Jul].

written as

$$I(r,z) = \frac{2P}{\pi w^2(z)} \exp\left(-2\frac{r^2}{w^2(z)}\right) \tag{3.46}$$

where r represents the radial coordinate and P the laser power. The $1/e^2$-beam radius $w(z) = w_0\sqrt{1+\left(\frac{z}{z_\mathrm{R}}\right)^2}$ is determined by the beam waist w_0 and Rayleigh length $z_\mathrm{R} = \pi w_0^2/\lambda$.

The realization of complex trapping geometries is one of the major challenges of state-of-the-art experiments. First examples which could be realized are ring shaped potentials [Hen09] which can be dynamically modified and periodic potentials in various dimensions [Zim11, Blo08]. In principle optical traps along arbitrary curves in three dimensions can be realized using holographic techniques. The power of this technique is demonstrated in figure 3.7 where the intensity distribution of a knotted ring geometry is realized which could potentially serve as a trap for cold atoms.

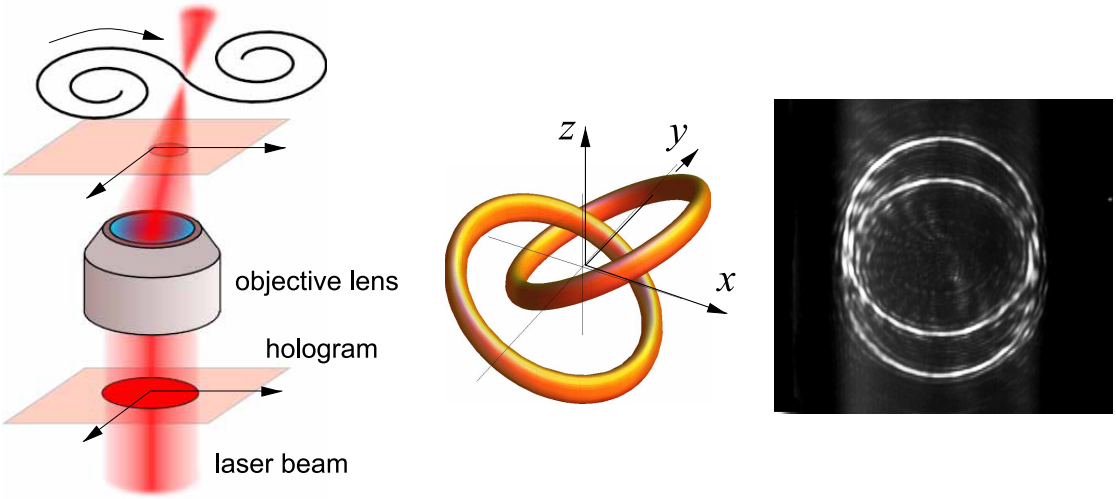

Figure 3.7: Realizing arbitrary optical potentials with light. A hologram and an objective can be used to create arbitrary optical potential geometries (left panel). The power of this technique is shown in the middle and right panel with the intensity distribution of knotted rings realized in three dimensions. Adapted from [Sha11].

4 From macroscopic to mesoscopic ensembles

Ultracold atoms have been used to explore fundamental problems of quantum physics. So far research has been focused on the exploration of bulk properties of many-particle systems. To proceed towards the intriguing regime of few-particle physics several hurdles have to be overcome. The main challenge is to gain full control over the system's quantum state, in particular the number of particles.
Our approach to realize a few-particle quantum system, the 'spilling technique', is introduced in this chapter. This is followed by a description of the WBK method, the main theoretical tool, which we use to estimate relevant quantities such as the energy of the system's quantum states and their tunneling times. The chapter closes with the description of the simplest non-trivial few-particle system: two interacting atoms in the ground state of a one-dimensional harmonic potential. The analytic solution for the system's energy as a function of interaction strength is discussed and a calculation is performed how interaction shifts modify the dynamics of the two particles.

4.1 Controlling the quantum state – the spilling technique

To proceed from the macroscopic to the few-particle limit we use two fundamental properties of a degenerate Fermi gas: According to Pauli's principle each energy state can be occupied with one fermionic atom per spin state. Furthermore, the occupation probability for the lowest energy states approaches unity according to Fermi-Dirac statistics. As a consequence the lowest energy states are occupied with one fermionic atom per spin state with high probability.
This allows us to obtain control over the number of particles by controlling the number of occupied quantum states. Our approach, the spilling technique, is to choose the occupied quantum states by tilting the confining potential in such a way that only a well defined number of states remains bound.
The starting point for applying this scheme is a degenerate Fermi gas as sketched

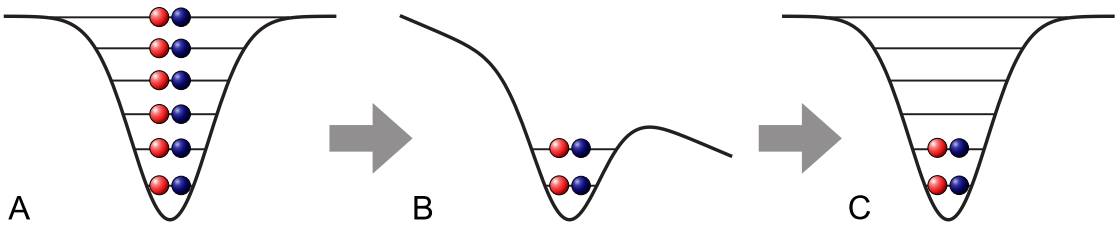

Figure 4.1: The spilling technique. By tilting the trapping potential, the number of occupied quantum states can be controlled. The strength of the tilt defines the number of remaining atoms in the trap.

in figure 4.1: Atoms in state $|1\rangle$ (red balls) and $|2\rangle$ (blue balls) are confined in the potential of an optical dipole trap whose lowest energy levels are occupied with one atom per state (A). By applying a magnetic field gradient $\nabla \boldsymbol{B}$ the atoms are subject to a force due to their magnetic moment $\boldsymbol{\mu}$ that pushes the atoms out of the trap

$$\boldsymbol{F} = \nabla(\boldsymbol{\mu} \cdot \boldsymbol{B}) = (\boldsymbol{\mu} \cdot \nabla)\boldsymbol{B} \tag{4.1}$$

and the potential gets deformed (B). We then wait for a duration t_{spill} until all atoms occupying states which are not part of the desired final quantum state have left the trap. Then, we bring the potential back to its original value (C). After the spilling process is completed, the system ends up in a well defined quantum state. The number of occupied energy states after the spilling process is chosen by controlling the strength of the magnetic field gradient and the depth of the optical potential.
The mapping of the number of occupied energy levels to the number of particles crucially depends on the system's dimensionality. For a 1-D system, energy states are non-degenerate. Therefore each energy level contributes to the final system with one atom per spin state. In the case of two- and three-dimensional systems degenerate energy levels exist. Thus one energy shell can host as many atoms as the degree of degeneracy allows according to Pauli's principle.
The dimensionality of the system which we realize by the axially symmetric optical dipole trap is given by the aspect ratio of the trap

$$\eta = \frac{\omega_\perp}{\omega_\parallel} \tag{4.2}$$

where $\omega_\parallel$ and $\omega_\perp$ is the harmonic trap frequency in axial and radial direction respectively. If the number of atoms in one spin state is smaller than $\eta + 1$, radially only the lowest energy state is occupied. Then, the system is effectively one-dimensional. With an aspect ratio of $\eta = 1 : 10$ for our dipole trap the system is expected to remain one-dimensional for up to $N \sim 20$ atoms. In this regime

the simple picture of spilling shown in figure 4.1 is valid. The relevant potential in axial direction is given as a sum of a Lorentzian according to equation 3.46 and a linear term due to the applied gradient

$$V(z) = V_0 \left(1 - \frac{1}{1 + \left(\frac{z}{z_\mathrm{R}}\right)^2}\right) - \mu_B \, B' \, z \tag{4.3}$$

where V_0 is the depth of the optical potential at $(z, r) = 0$ and z_R the Rayleigh length of the focused laser. The depth of the trap at its center can be calculated using equation 3.45 as

$$V_0 = -\frac{3\,\pi\,c^2}{2\,\omega_0^3}\left(\frac{\Gamma}{\omega_0 - \omega} + \frac{\Gamma}{\omega_0 + \omega}\right). \tag{4.4}$$

4.1.1 Requirements

The scheme can be only applied if two main requirements are met: the occupation probability for the lowest energy states in the trap has to approach unity and the occupied quantum states can be selected on a single state level.

Occupation probability

In a degenerate Fermi gas, the occupation probability for a state with energy E is described by Fermi-Dirac statistics

$$P(E) = \frac{1}{e^{(E-\mu)/k\,T} + 1} \tag{4.5}$$

where μ is the chemical potential and T the temperature. For $T = 0$ all states up to the Fermi energy E_F are occupied with unity probability. For non-zero temperature the occupation probability increases the lower the state's energy is compared to the Fermi energy. This allows us to enhance the occupation probability of the lowest states by increasing the Fermi energy of the system. To realize this we start with a reservoir of cold atoms trapped in an optical dipole trap as sketched in figure 4.2 and enhance its Fermi energy by superimposing a deep microtrap with the reservoir. The maximum enhancement is achieved only if the width of Fermi edge, which is determined by the temperature, is not increased during the transfer of atoms from the reservoir. This is the case when the atoms in the microtrap and the reservoir are in thermal equilibrium. To calculate the occupation probability for the lowest state, we use equation 4.5 where $\mu \approx E_F = k_B\,T_F$ and typical experimental parameters: the energy of the lowest

state is given by $E_0 = \hbar\omega \approx \hbar \cdot 2\pi \times 10\,\mathrm{kHz}$. The temperature of the combined system is determined by the temperature of the reservoir $T = 250\,\mathrm{nK}$ assuming thermal equilibrium between the reservoir and the microtrap. T_F is obtained as the sum $T_F^{\mathrm{reservoir}} + T_F^{\mathrm{microtrap}} \approx (0.5 + 3.5)\,\mu\mathrm{K} = 4\mu\mathrm{K}$.
As a result we can expect an occupation probability for the lowest state of the combined system of $P(E_0) > 0.9999$ which is large enough not to constrain our preparation scheme.

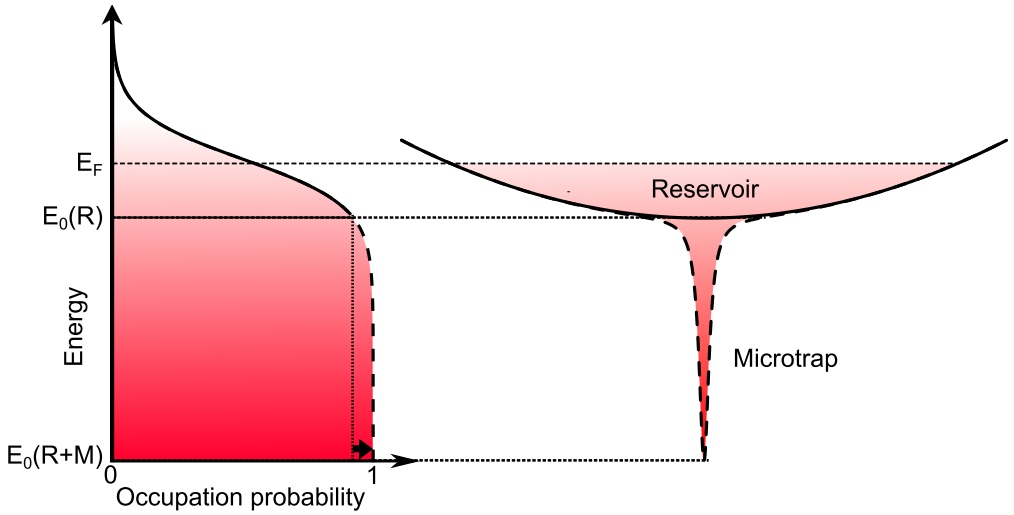

Figure 4.2: Starting point for the preparation of the few-fermion system. The potential of the optical dipole trap is shown on the right, the corresponding Fermi-Dirac distribution on the left hand side. As a starting point we prepare a reservoir of cold atoms. To increase the occupation probability for the lowest energy states we superimpose a deep microtrap with this reservoir. This increases the Fermi energy of the combined system. Therefore the occupation probability for the lowest states approaches unity (black arrow).

Control on the single quantum state level

The deterministic preparation of the few-particle system requires that all atoms occupying states which are not part of the desired final quantum state leave the trap during the duration of the spilling process t_{spill}. To see how this requirement can be fulfilled the energy spectrum for the system in the tilted configuration has to be considered as shown in figure 4.3. Atoms with an energy higher than the potential barrier $E > V_0$ (gray shaded region) are unbound and escape on a

timescale given by the trap frequency $\omega_{\parallel}$. The escape of these atoms is guaranteed as long as

$$t_{\text{spill}} \gg 1/\omega_{\parallel}. \tag{4.6}$$

In the case of a true bound state with $E < V_0$ atoms can tunnel through the barrier. To prepare a system with atoms occupying energy levels $E_0 ... E_N$ in a reproducible way two conditions have to be fulfilled: First, tunneling of these atoms during the spilling process has to be avoided. Therefore the corresponding tunneling time constants $\tau_0 ... \tau_N$ have to fulfill

$$\tau_0 ... \tau_N \gg t_{\text{spill}}. \tag{4.7}$$

Second, the atoms occupying the energy level closest to the continuum E_{N+1} have to tunnel with a probability close to 1. Therefore the time constant has to satisfy

$$\tau_{N+1} \ll t_{\text{spill}}. \tag{4.8}$$

To be able to reach this regime in the experiment, the separation of the energy levels needs to be on the same order of magnitude as the potential barrier height V_0. This requires a tight microtrap as discussed in chapter 5.6.1.

4.2 Model of the system–the WKB method

This section introduces the WKB (Wentzel-Kramers-Brillouin) method as a theoretical tool to model our experiment. We use it to obtain relevant quantities such as the energy of the single particle states. Furthermore we calculate tunneling times of bound states for the tilted potential in a non-interacting system, similar to [Ott10]. We also determine the energy shift caused by interaction for two repulsively interacting particles. A full description of the method can be found e.g. in [Sch07, Mer98] which is the basis of the following introduction.
In the presence of a potential $V(x)$ the Schödinger equation for one particle reads

$$-\frac{\hbar^2}{2m}\nabla^2\psi = (E - V(x))\,\psi \tag{4.9}$$

If $V = V_0$ is constant, the trivial solution is a plane wave $A \cdot \exp(\pm i\, kx)$. This motivates the ansatz of the WKB method: For a potential $V(x)$ which varies slowly with x, the wave function can be written by means of an amplitude and a phase term according to

$$\psi(x) = A(x)e^{iS(x)/\hbar} \tag{4.10}$$

where the phase term $S(x)$ is in general not linear in k due to the the influence of the potential. To solve the problem, solutions for $A(x)$ and $S(x)$ have to be found.

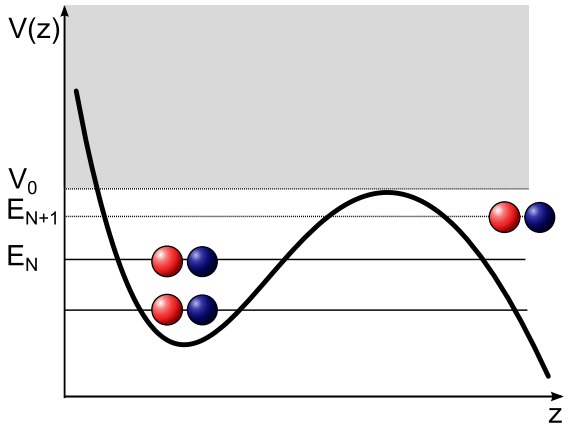

Figure 4.3: Energy spectrum of the system during the spilling process. Systems with $2N$ atoms are prepared with high fidelity when the duration of the spilling process t_{spill} is long enough to remove all atoms occupying energy states E_{N+1} and above. To remove atoms occupying continuum states (gray region) the spilling duration must exceed $1/\omega_{\parallel} \ll t_{\text{spill}}$, where $\omega_{\parallel}$ is the trap frequency of the potential. For atoms occupying the energy state close the the continuum E_{N+1} the tunneling time through the barrier τ_{N+1} has to fulfill $t_{\text{spill}} \ll \tau_{N+1}$. Tunneling of atoms which are part of the final system has to be suppressed for the duration of t_{spill} which requires $\tau_0 ... \tau_N \gg t_{\text{spill}}$.

The slow variation of the potential $V(x)$ translates into a condition of momentum

$$\lambda \left| \frac{dp}{dx} \right| \ll |p(x)| \tag{4.11}$$

where

$$p(x) = \sqrt{2m\left(E - V(x)\right)} \tag{4.12}$$

is the classical momentum and $\lambda(x) = 2\pi\hbar/p(x)$ the local wavelength. In this semi classical picture the change of the particle's momentum over one wavelength has to be small compared to the momentum itself.
In this case, the parameters of equation 4.10 are found to be

$$S(x) = \pm \int_{-\infty}^{\infty} dx' \sqrt{2m\left(E - V(x')\right)} \tag{4.13}$$

and

$$A(x) = \frac{C}{\sqrt{S'(x)}} \tag{4.14}$$

where $S'(x) = \partial/\partial x\, S(x)$ and a numerical coefficient C. The wave function which solves the Schrödinger equation 4.9 is then given by

$$\psi(x) = \sum_{\pm} \frac{C'_{\pm}}{\sqrt{p(x)}} e^{\pm i \int^x dx' p(x')/\hbar} \tag{4.15}$$

where $C'_{\pm}$ are coefficients which have to be determined by boundary conditions. Depending on the particle's energy E two different types of solution exist:
For $E > V$ as it is the case for a particle moving in a potential, $p(x)$ is real leading to an oscillating wave function with a phase proportional to $\int dx'\, p(x')$.
For $E < V$, $p(x)$ is imaginary. Therefore the exponent in solution 4.15 is real. The corresponding wave function decreases, respectively increases exponentially.
For the tilted potential used in the experiment both scenarios are relevant depending on the regions shown in figure 4.4. In region I $E > V$, therefore the solution is a bound state of the potential. Region II represents the tunneling barrier where $E < V$. In region III $E > V$, thus the particle is free. With the WKB method both the energies of the bound states in region I and the tunneling probability through the barrier can be calculated.

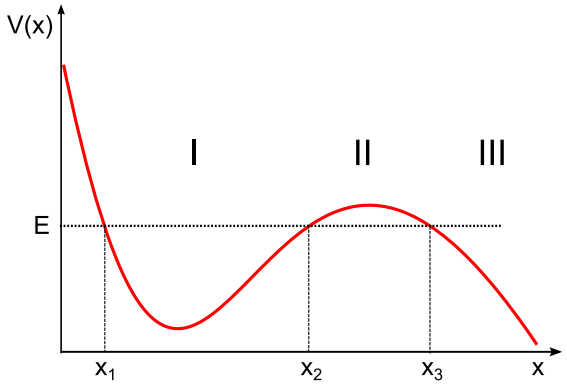

Figure 4.4: Tunneling barrier for the tilted potential. During the spilling process, atoms occupying bound states in region I can tunnel through the barrier (region II) to become free particles (region III). Both the energy levels of the bound states and the tunneling time constants are calculated using the WKB method (see text).

Bound states

In the vicinity of the classical turning points x_1 and x_2, the WKB solution becomes invalid, because p goes to zero. However a solution for x close to x_1 can be found

by approximating the potential linearly $V = V'x$ near the turning point. The Schrödinger equation for the wave function near x_1 becomes

$$\frac{d^2}{dx^2}\psi = -c^2 x\psi \tag{4.16}$$

where $c = \sqrt{-2mV'}/\hbar$. This equation is solved by Airy functions which far away from the turning point behave like

$$\psi_{x1}(x) \sim \sin\left(\frac{1}{\hbar}\int_{x_1}^{x} dx' p(x') + \frac{\pi}{4}\right). \tag{4.17}$$

A similar solution $\psi_{x2}(x)$ can be found for the second turning point x_2.

$$\psi_{x2}(x) \sim \sin\left(\frac{1}{\hbar}\int_{x}^{x_2} dx' p(x') + \frac{\pi}{4}\right) \tag{4.18}$$

$$= \sin\left(\frac{1}{\hbar}\left(\int_{x1}^{x_2} dx' p(x') - \int_{x1}^{x} dx' p(x')\right) + \frac{\pi}{4}\right) \tag{4.19}$$

Away from both turning points, the solutions $\psi_{x1}(x)$ and $\psi_{x2}(x)$ have to agree. This yields a condition on the integral over the momentum

$$\frac{1}{\hbar}\int_{x_1}^{x_2} dx\, p(x) = \pi(n + 1/2) \tag{4.20}$$

where $n = 0, 1, 2, ...$
Equation 4.20 is equivalent to the Bohr-Sommerfeld quantization of classical momentum. The bound state energies of any slowly varying potential $V(x)$ can be calculated by inserting the potential into 4.12 and evaluating the integral 4.20 for a given energy E. The values of E which fulfill equation 4.20 are the energies of the bound states in the potential.

Tunneling probabilities

A tunneling barrier represented by region II in figure 4.4 with $E < V(x)$ leads to an imaginary value of $p(x)$. This causes the solution for the wave function 4.15 to decay exponentially. The transmission probability can be obtained as

$$|S(E)|^2 = \exp\left(-2\int_{x_1}^{x_2} \frac{\sqrt{2m(V(x) - E)}}{\hbar} dx\right) \tag{4.21}$$

To calculate the tunneling rate of an atom the transmission probability 4.21 has to be weighted with the rate at which the atom hits the barrier. This 'knocking frequency' $\nu(E)$ can be determined via the particle's energy E

$$\nu(E) = \frac{E}{h}. \tag{4.22}$$

The tunneling rate then becomes

$$R(E) = \nu(E) \cdot |S(E)|^2. \tag{4.23}$$

The mean lifetime of the atom is given by

$$\tau(E) = \frac{1}{R(E)} = \frac{1}{\nu} \cdot \frac{1}{|S(E)|^2}. \tag{4.24}$$

4.2.1 Energies and lifetimes for a non-interacting system

For realistic experimental parameters, the tilted potential 4.3 takes the form

$$V(z) = s \cdot 3,326\,\mu\mathrm{K}\, k_B \left(1 - \frac{1}{1 + \left(\frac{z}{9.975 \cdot 10^{-6}\mathrm{m}}\right)^2}\right) - \mu_B \cdot 18.92\,\mathrm{Gauss/cm} \cdot z \tag{4.25}$$

where $0 < s < 1$ is a variable representing the relative depth of the optical trap when the gradient is applied. In the experiment we use s to control the number of atoms of the prepared system as discussed in chapter 6. The detailed characterization of the potential which leads to the parameters for the calculation is discussed in chapter 7.3. In figure 4.5 the potential is plotted for three exemplary values of s.

With the mean lifetime for each state given by equation 4.24, the mean occupation probability for an energy level E_i after a spilling duration of t_{spill} can be calculated to

$$P(E_i) = e^{-t_{\mathrm{spill}}/\tau(E_i)} \tag{4.26}$$

From that, the mean atom number in the final system can be obtained as

$$n = 2 \cdot \sum_{i=1}^{N} P(E_i) \tag{4.27}$$

where N is the number of bound states. The factor of 2 accounts for the fact that each energy state is occupied by 2 atoms. The mean atom number is calculated as a function of s assuming a spilling duration of $t_{\mathrm{spill}} = 25\,\mathrm{ms}$. The result is shown in figure 4.5. In certain ranges of s stable plateaus for even atom numbers exist. In this regime, the lifetime for atoms occupying the highest lying bound state is short compared to the spilling duration and atoms occupying lower lying states have long lifetimes.

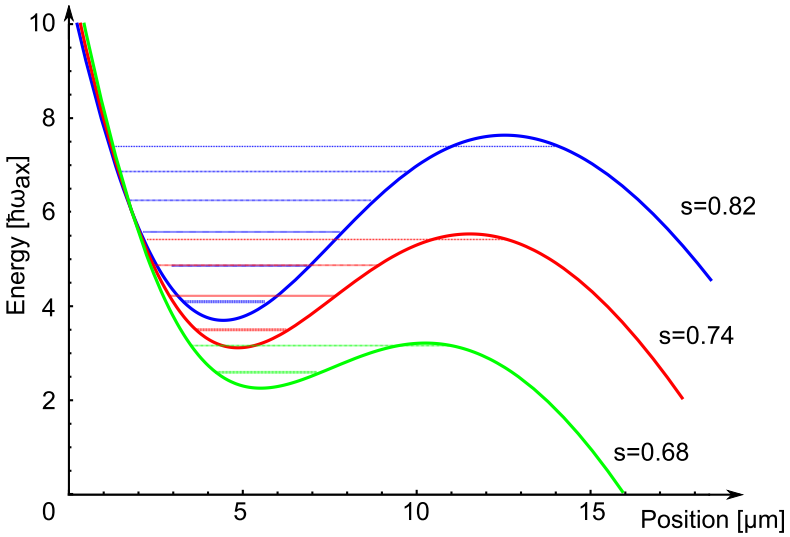

Figure 4.5: Tilted potential for parameters used in the experiment. The parameter s represents the depth of the microtrap when the gradient is applied. We control the number of atoms by tuning s to a value such that atoms occupying the highest bound state tunnel through the barrier while at the same time tunneling of atoms occupying lower lying energy states is suppressed. The y-axis is scaled in units of $\hbar\omega_{\mathrm{ax}}$ where ω_{ax} is the harmonic trap frequency of the $s = 0.82$ potential curve without gradient applied.

4.3 Two interacting particles

In the following an analytic solution for two interacting particles in a harmonic trap is given according to [Bus98, Idz06]. The solution for a spherically symmetric potential as well as a cigar-shaped axially symmetric potential, as it is used in the experiment, is discussed. With these solutions the system's interaction energy can be directly calculated for any value of the inter-particle interaction strength. As we tune the interaction strength via a magnetic Feshbach resonance as described in chapter 3.1.2, the system's interaction energy is calculated as a function of the magnetic field. In the last part the WKB method is used to derive the tunneling time constants τ for the tilted potential depending on the value of the applied magnetic field.

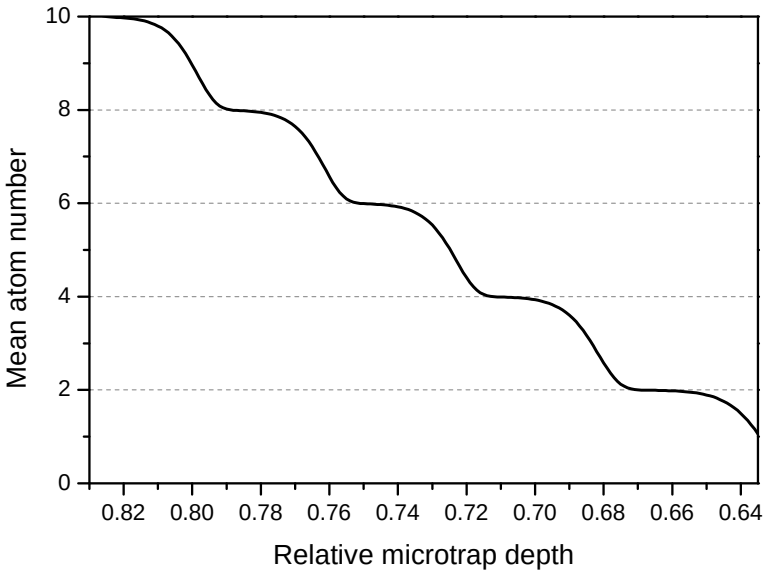

Figure 4.6: WKB calculation for the mean atom number. The mean atom number is determined by the lifetime of bound states in the tilted potential. The lifetimes are controlled by means of the depth of the microtrap potential. Plateaus in the mean atom number indicate that the system only consists of atoms occupying long lived bound states and excess atoms on higher energy levels tunnel on a fast timescale. This is required for deterministic preparation. Parameters for the calculation are $B' = 18.92\,\mathrm{Gauss/cm}$, $P = 291.5\,\mu\mathrm{W}$ and $w_0 = 1.838\mu\mathrm{m}$.

4.3.1 Analytical solution

For two interacting particles in an external trapping potential, the Hamiltonian is of the form

$$H = -\frac{\hbar^2}{2m}\nabla_1^2 - \frac{\hbar^2}{2m}\nabla_1^2 + V_{\mathrm{ext}}(\boldsymbol{r}_1) + V_{\mathrm{ext}}(\boldsymbol{r}_2) + V_{\mathrm{int}}(\boldsymbol{r}_1 - \boldsymbol{r}_2) \tag{4.28}$$

where $\boldsymbol{r}_1$ and $\boldsymbol{r}_2$ denote spatial coordinates of the atoms. V_{ext} denotes the external trapping potential and V_{int} the interaction between the atoms. The interaction between two ultracold atoms, as explained in chapter 3.1, is fully determined by the s-wave phase shift of the scattering process which is fixed by a single parameter, the scattering length a. To model the interaction any potential can be used as long as it reproduces the right scattering amplitude in the limit $r_{\mathrm{eff}} \ll 1/k$ where r_{eff} is the effective range of the potential and k the relative momentum of the colliding particles. In particular a point-like potential can be used leading to an interaction

term in the Hamiltonian

$$V_{\text{int}}(\boldsymbol{r}_2 - \boldsymbol{r}_1) = \frac{4\pi\hbar^2 a}{m}\delta^{3\text{D}}(\boldsymbol{r}_2 - \boldsymbol{r}_1) \tag{4.29}$$

where $\delta^{3\text{D}}$ is the delta function in three dimensions. The drawback of this potential is that the Hamiltonian is not self adjoint in three dimensions, the corresponding matrix is not hermitian.

Spherically symmetric 3D harmonic trap

To overcome this problem, a regularized delta function

$$\delta^{\text{reg}}(\boldsymbol{r}) = \delta^{3\text{D}}(\boldsymbol{r})\frac{\partial}{\partial r}r. \tag{4.30}$$

has been used by Busch et al. [Bus98] to model the interaction between the two particles. With this potential the interaction term of the Hamiltonian becomes

$$V_{\text{int}}(\mathbf{r}) = \frac{4\pi\hbar^2 a}{m}\delta^{3\text{D}}(\boldsymbol{r})\frac{\partial}{\partial r}r. \tag{4.31}$$

For a harmonic trap with spherical symmetry the full Hamiltonian becomes

$$H = -\frac{\hbar^2}{2m}\nabla_1^2 - \frac{\hbar^2}{2m}\nabla_1^2 + \frac{m}{2}\omega r_1^2 + \frac{m}{2}\omega r_2^2 + \frac{4\pi\hbar^2 a}{m}\delta^{3\text{D}}(\boldsymbol{r})\frac{\partial}{\partial r}r \tag{4.32}$$

where ω is the trap frequency. The Schrödinger equation for this Hamiltonian can be solved because center-of-mass and relative motion of the particles decouple. Therefore the Hamiltonian can be written as a sum $H = H_{\text{CM}} + H_{\text{rel}}$ with

$$H_{\text{CM}} = -\frac{\hbar^2}{2M}\nabla_R^2 + \frac{M}{m}V_{\text{ext}}(\boldsymbol{R}) \tag{4.33}$$

and

$$H_{\text{rel}} = -\frac{\hbar^2}{2\mu}\nabla_r^2 + \frac{\mu}{m}V_{\text{ext}}(\boldsymbol{r}) + V_{\text{int}}(\boldsymbol{r}) \tag{4.34}$$

where $\boldsymbol{R} = (\boldsymbol{r}_1 + \boldsymbol{r}_2)/2$ is the center of mass coordinate, $\boldsymbol{r} = \boldsymbol{r}_1 - \boldsymbol{r}_2$ the relative coordinate of the atoms, $M = 2 \cdot m$ the total mass and $\mu = m/2$ the reduced mass. By expressing all lengths in units of the harmonic oscillator length $x_0 = \sqrt{\hbar/(\mu\omega)} = \sqrt{2\hbar/(m\omega)}$ and energies in units of $\hbar\omega$ the Schrödinger equation for the relative motion simplifies to

$$\left(-\frac{1}{2}\nabla_r^2 + \frac{1}{2}\boldsymbol{r}^2 + 2\pi a\delta^{3\text{D}}(\boldsymbol{r})\frac{\partial}{\partial r}r\right)\Psi(\boldsymbol{r}) = E\,\Psi(\boldsymbol{r}) \tag{4.35}$$

which reduces the equation to an effective one-particle problem.
To solve the equation the unknown wave function $\Psi(\boldsymbol{r})$ is expanded in terms of harmonic oscillator wave functions $\phi_n(\boldsymbol{r})$

$$\Psi(\boldsymbol{r}) = \sum_{n=0}^{\infty} c_n \phi_n(\boldsymbol{r}) \tag{4.36}$$

with coefficients c_n which have to be determined. They are found by inserting the expansion into the Schroedinger equation 4.35 and projecting the result onto the harmonic oscillator function $\phi_n^*(\boldsymbol{r})$. After some algebra one obtains for the coefficients

$$c_n = A \frac{\phi_n^*(0)}{E_n - E} \tag{4.37}$$

where A is a numerical factor which normalizes the wave function. With these coefficients the wave function 4.36 can be reinserted into 4.35 yielding

$$2\pi \left[\frac{\partial}{\partial r} \left(r \sum_{n=0}^{\infty} \frac{\phi_n^*(0)\, \phi_n(\boldsymbol{r})}{E_n - E} \right) \right]_{r \to 0} = -\frac{1}{a}. \tag{4.38}$$

After inserting the actual orbitals of the harmonic oscillator $\phi_n(\boldsymbol{r})$, the left hand side of equation 4.38 can be evaluated. One finds the important solution which relates the interaction strength given by a and the total energy in the relative degree of freedom of the two particles E_{tot}

$$2 \frac{\Gamma(-E_{\mathrm{tot}}/2 + 3/4)}{\Gamma(-E_{\mathrm{tot}}/2 + 1/4)} = \frac{1}{a} \tag{4.39}$$

where Γ is the Gamma function. As we are interested in the interaction shift the offset energy of 3/2 in units of $\hbar\omega$ has to be subtracted. For the interaction shift ϵ one finds

$$2 \frac{\Gamma(-\epsilon/2)}{\Gamma(-\epsilon/2 - 1/2)} = \frac{1}{a}. \tag{4.40}$$

Axially symmetric harmonic trap

For a system with axial symmetry the analytic solution has been found by Idziaszek et al. [Idz06]. The solution can be given analytically because center of mass motion and relative motion decouple as in the spherically symmetric case. Furthermore the motion in longitudinal direction decouples from the motion in radial direction. In relative coordinates the Schrödinger equation for an axially symmetric harmonic oscillator writes

$$\left(-\frac{1}{2} \nabla_r^2 + \frac{1}{2} \left(\eta^2 \rho^2 + z^2 \right) + 2\pi a \delta\left(\boldsymbol{r}\right) \frac{\partial}{\partial r} r \right) \Psi(\boldsymbol{r}) = E\, \Psi(\boldsymbol{r}) \tag{4.41}$$

where $\eta = \frac{\omega_\perp}{\omega_\parallel}$ is the aspect ratio of the trap determined by the trap frequencies in longitudinal $\omega_\parallel$ and transversal $\omega_\perp$ direction respectively. Energies are given in units of $\hbar\omega_\parallel$ and lengths in units of the reduced harmonic oscillator length $x_\parallel = \sqrt{2\hbar/m\omega_\parallel}$. The solutions can be determined in the same way as in the symmetric case: by expanding the wave function in terms of harmonic oscillator functions, in this case in polar coordinates $\Phi_n(\rho, \phi)$ and the harmonic oscillator wave function in z direction $\Theta_k(z)$

$$\Psi(\boldsymbol{r}) = \sum_{n,k} c_{n,k} \Phi_n(\rho, \phi) \Theta_k(z). \tag{4.42}$$

After the coefficients $c_{n,k}$ have been found in a similar way as in the previous case, the ansatz 4.42 can be inserted into the Schrödinger equation 4.41. This leads to the equation which relates the interaction strength to the system's energy. For the case of a cigar-shaped trap with $\eta > 1$ and $\eta = n$ being a positive integer, the relation is given by

$$\frac{2\Gamma(-\epsilon/2)}{\Gamma(-\epsilon/2 - 1/2)} - \frac{\Gamma(-\epsilon/2)}{\Gamma(-\epsilon/2 + 1/2)} \sum_{m=1}^{n-1} F\left(1, \frac{\epsilon}{2}, \frac{\epsilon}{2} + \frac{1}{2}, e^{i2\pi\frac{m}{n}}\right) = \frac{1}{a} \tag{4.43}$$

where F is the hyper-geometric function (Hypergeometric2F1 in Mathematica). For the spherically symmetric case $n = \eta = 1$ the second term in equation 4.43 vanishes leading to the same result as found in the previous section.
A simpler expression which can be used to calculate the lowest energy states $\epsilon < \eta\,\hbar\omega_\parallel$ reads

$$-\sqrt{\eta}\xi_H\left(\frac{1}{2}, 1 - \frac{\epsilon}{2\eta}\right) - \eta\frac{\Gamma(-\epsilon/2)}{\Gamma(-\epsilon/2 + 1/2)} = \frac{1}{a} \tag{4.44}$$

where ξ_H denotes the Hurwitz zeta function (HurwitzZeta in Mathematica). Expressions for pancake shaped traps with aspect ratio $\eta < 1$ can be found in [Idz06].

Coupling strength in one dimension

So far equations which relate the coupling strength of the two particles to their interaction energy have been given for the case of a spherically symmetric (equation 4.40) and axially symmetric (4.43) harmonic potential. In general, the coupling strength on the right hand side of these equations depends on the scattering amplitude f which describes the asymptotic form of the scattered wave function as discussed in chapter 3.1. When no external potential is present the scattered wave has radial symmetry. In the limit of low momentum the relative wave function of the two particles can be written

$$\psi_r(\boldsymbol{r}) \sim e^{i\boldsymbol{k}\boldsymbol{r}} - a\frac{e^{i\,kr}}{r}.$$

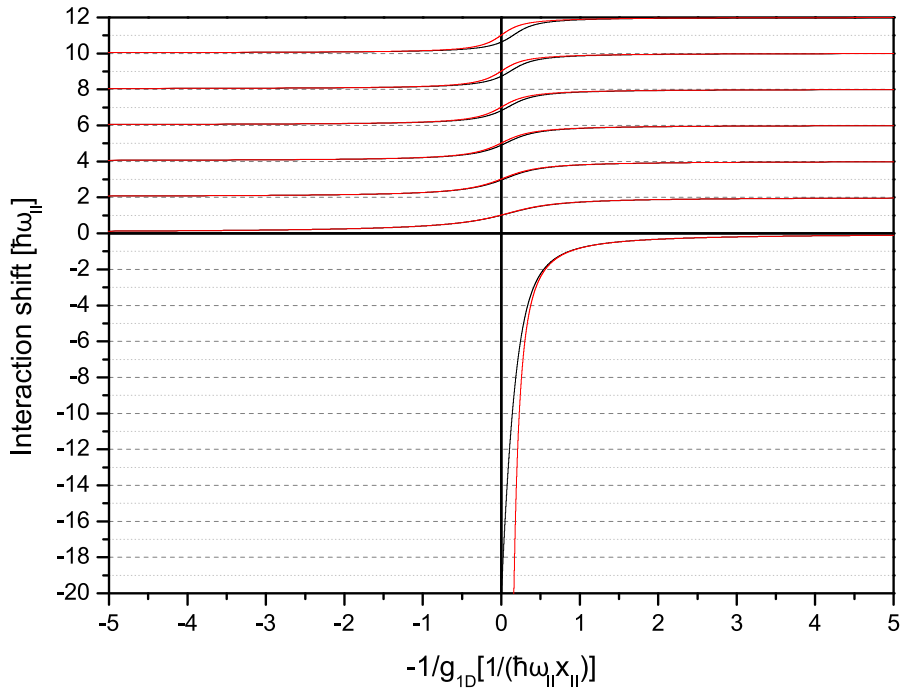

Figure 4.7: Energy shift for two atoms as a function of negative inverse coupling strength. The red lines represent the analytic solution for a spherically symmetric harmonic oscillator potential according to Busch et al. [Bus98]. The solution for an axially symmetric harmonic oscillator potential with aspect ratio of 1 to 10 is indicated by the black lines according to Idziaszek et al. [Idz06]. Only the latter solution is a valid description for the bound state $E < 0$.

according to equation 3.12. An external trapping potential influences the asymptotic form of the wave function but can be neglected when the characteristic length scale of the external potential r_0 is large compared to a. When r_0 becomes comparable to a the scattering amplitude and thus the coupling strength is modified compared to the free particle case. In an extreme case, the confinement becomes strong in two dimensions such that the asymptotic wave function is restricted to one dimension. This effect has been calculated by Olshanii et al. [Ols98] for a potential symmetric around the z axis with strong harmonic confinement in radial direction. To solve the problem, two approximations are made which are fulfilled in our experiment for particle numbers $N \ll 2\eta$ where $\eta = 10$ denotes the aspect ratio of the trap: the system is radially in its ground state and the energy of the colliding particles is not sufficient to excite the first axially symmetric state which

has an energy difference of $2\,\hbar\omega_\perp$ to the ground state. This sets the condition

$$\frac{\hbar^2 k_z^2}{2\mu} < 2\hbar\omega_\perp \tag{4.45}$$

where k_z denotes the wave vector of the relative wave function of two interacting particles. With this approximation the asymptotic form of the wave function becomes

$$\psi_r(z,\rho) \sim \left(e^{ik_z z} + f \cdot e^{i\,k\cdot z}\right)\phi(\rho)$$

where $\phi(\rho)$ is the wave function of the ground state of the harmonic oscillator in radial direction. In the limit of low momentum the scattering amplitude has the following form

$$f(k_z) = -\frac{1}{1 + ik_z a_{1\mathrm{D}}} \tag{4.46}$$

where the scattering length in one dimension is calculated as

$$a_{1\mathrm{D}} = -\frac{x_\perp^2}{2a}\left(1 - C\,\frac{a}{x_\perp}\right) \tag{4.47}$$

where $C = \zeta\left(\frac{1}{2}\right) = 1.46...$, ζ is the Riemann zeta function and $x_\perp = \sqrt{2\hbar/m\omega_\perp}$ denotes the reduced harmonic oscillator length in radial direction. In this case a one dimensional delta-potential

$$V_{1\mathrm{D}}(z) = g_{1\mathrm{D}}\delta(z). \tag{4.48}$$

can be used to model the interactions which yields the right scattering amplitude 4.46. This defines the coupling constant to

$$g_{1\mathrm{D}} = -\frac{4\hbar^2 a}{m x_\perp^2}\frac{1}{1 - Ca/x_\perp}. \tag{4.49}$$

Compared with the coupling constant in three dimensions 3.37

$$g_{3\mathrm{D}} = \frac{4\pi\hbar^2}{m}a$$

the coupling constant in one dimension can be obtained by rescaling a with a parameter of the confinement $x_\perp$. In particular, the coupling strength diverges when $a = 1/C\,x_\perp = 0.68\,x_\perp$ This divergence is referred to as a confinement-induced resonance. Equation 4.49 is important because it allows us to calculate the coupling strength between two particles for our one-dimensional system. As we tune the scattering length a by means of a magnetic Feshbach resonance (see

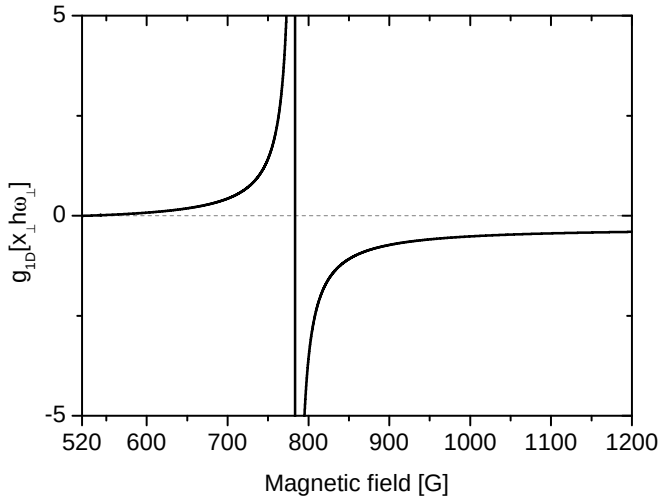

Figure 4.8: Coupling constant g_{1D} for two ultracold atoms as a function of magnetic field. When the scattering length a becomes comparable to the transverse harmonic oscillator length $x_\perp$ which is the case for a magnetic field of $B = 783\,\text{Gauss}$, g_{1D} diverges. This phenomenon is referred to as confinement-induced resonance.

figure 3.6) we calculate g_{1D} as a function of applied magnetic field.
The result is plotted in figure 4.8. The coupling strength diverges at a magnetic field of $B_{CIR} = 783\,\text{Gauss}$ because a becomes comparable to $x_\perp$.
The magnitude of $x_\perp$ and $\omega_\perp$ are determined by characterizing the optical potential as discussed in chapter 7.3. In particular, we measure the energy difference between first and third radial state $(E_2 - E_0)/h$. From that we deduce $\omega_\perp = \sqrt{2.75/4}\,(2\pi \times 14330)\,\text{Hz} = (2\pi \times 11883)\,\text{Hz}$ which yields $x_\perp = 0.53\mu\text{m}$ for the chosen relative depth of the microtrap of $s = 2.75/4$.
Since we determined the coupling strength for our system as a function of magnetic field, we can now use the analytical equation 4.40 to calculate the interaction shift of the particles in the trap. The result is presented in figure 4.9. Starting from a non-interacting system we can increase the interaction shift by more than $1.5\,\hbar\omega_\parallel$.

4.3.2 Experimental access to the interaction energy

The tunability of the interaction strength raises the question how this energy shift can actually be measured in the experiment. Our approach to probe the energy of the system is to explore the tunneling dynamics of the particles in the tilted

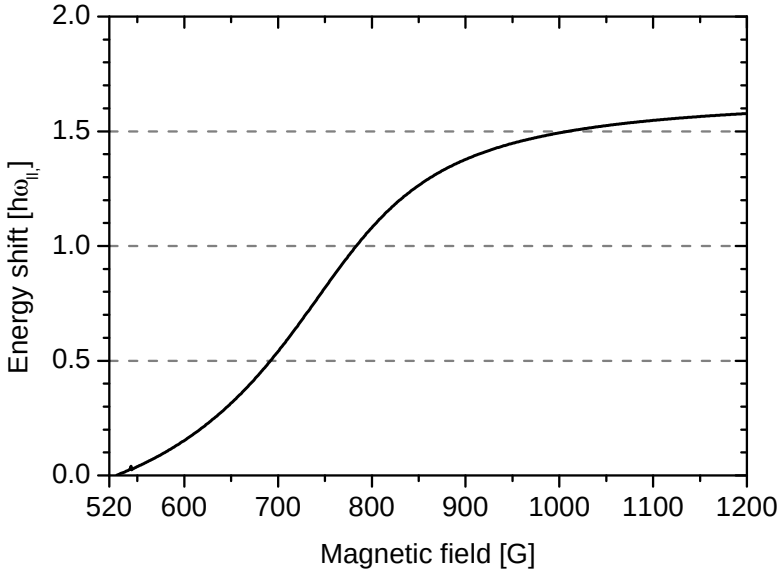

Figure 4.9: Energy shift as a function of magnetic field. The energy shift for two interacting atoms in a harmonic potential is calculated using the analytical expression given in equation 4.40 and the coupling strength in one dimension g_{1D} according to equation 4.49. We can raise the interaction energy by more than $1.5\,\hbar\omega_{\parallel}$ by increasing the magnetic field.

potential as sketched in figure 4.10. The higher the energy of the system becomes the smaller is the effective tunnel barrier for the particle and the faster is the timescale of the tunneling process. Given a precise theoretical mapping between the tunneling time constant and the system's energy, the energy of the system can be determined measuring tunneling times. We use the WKB method described in chapter 4.2 to establish this link. The model we use assumes that a shift in interaction energy affects the tunneling time of one atom through the barrier. The assumption is justified because as soon as one atom tunnels the interaction shift vanishes. This leads to a suppression of tunneling for the second atom. The model does not account for pair tunneling which is suppressed according to our measurements as discussed in chapter 7.1.

Before the results of the WKB calculation are discussed it is important to note that the analytical solution for the interaction shift given in equation 4.40 is valid for a harmonic potential. However, to measure the tunneling times we need to tilt the potential as shown in figure 4.10. Therefore the potential becomes anharmonic. In fact, the ratio of $\tilde{\omega}_{\parallel} = (E_1 - E_0)/\hbar$ to the harmonic approximation

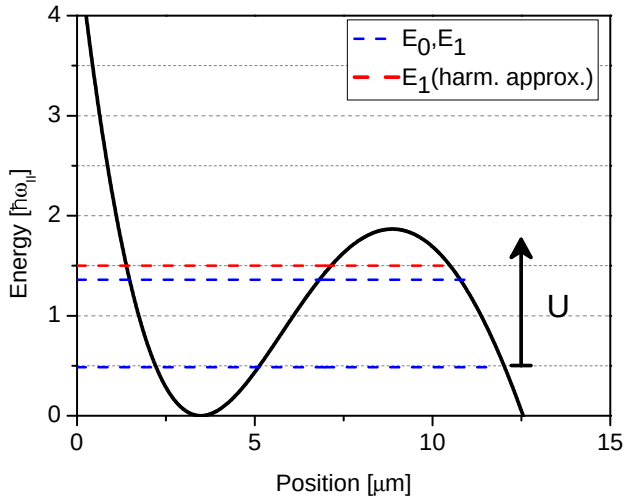

Figure 4.10: Principle of measuring the interaction shift U. Interactions between two particles increases the system's energy which effectively reduces the tunneling time of one atom through the barrier. By measuring the tunneling time we deduce the interaction shift U. Parameters for the calculation are $B' = 18.92\,\text{Gauss/cm}$, $P = 291.5\,\mu\text{W}$, $w_0 = 1.838\mu\text{m}$ and $s = 2.75/4$.

given by $\omega_\parallel$ amounts to $A = \tilde{\omega}_\parallel/\omega_\parallel \sim 80\%$ as indicated by the blue and red lines of figure 4.10. To account for this an-harmonicity we rescale the energy shift in the harmonic approximation as plotted in figure 4.9 by A. This rescaling leads to the fact that right at the confinement-induced resonance the energy shift amounts to $\hbar\tilde{\omega}_\parallel$ rather than $\hbar\omega_\parallel$ which agrees with our measurements [Zür11].
With this rescaled interaction shift we calculate the tunneling times as function of the magnetic field. The result is presented in figure figure 4.11.
For experimental parameters chosen, the lifetime of the ground state with vanishing interaction energy is extremely long ($t \sim 1000\,\text{s}$). When the interaction energy is raised, the tunneling barrier effectively decreases. Therefore the lifetime of the state is decreased by more than six orders of magnitude.
The most important result of the calculation is shown in figure 4.12 where the tunneling time is presented as a function of interaction shift. The energy shift is given in units of $\hbar\tilde{\omega}_\parallel$. This graph allows us to deduce the energy shift caused by interactions from the tunneling time which is the experimental observable.

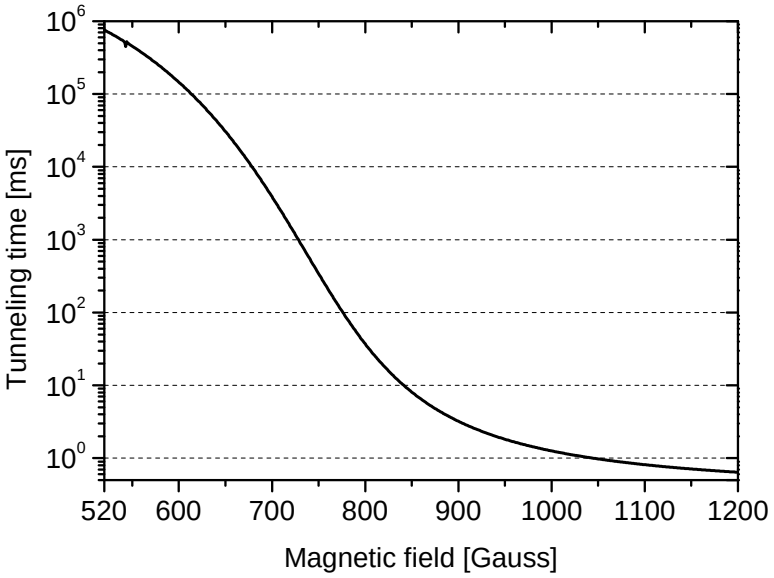

Figure 4.11: Tunneling time as a function of applied magnetic field for the tilted potential. As the interactions raise the system's energy for increasing magnetic field the tunneling barrier effectively decreases. Therefore the tunneling time can be reduced by more than six orders of magnitude.

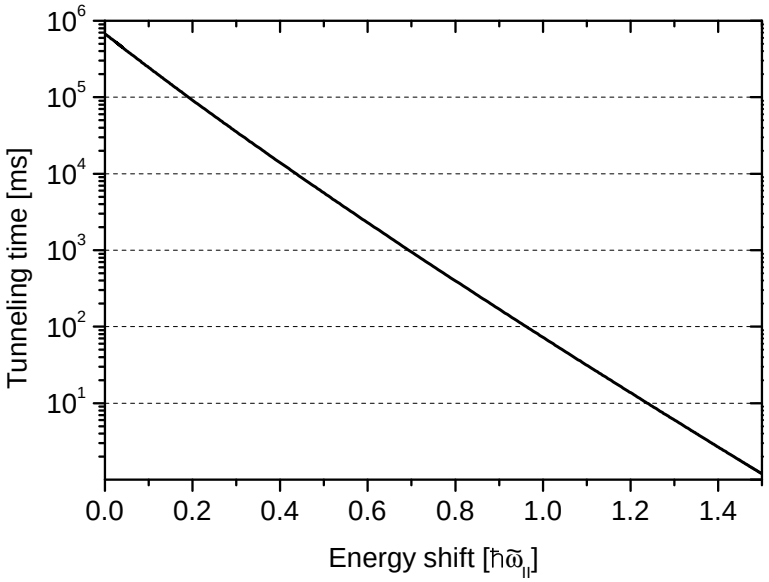

Figure 4.12: Tunneling time as a function of interaction shift for the tilted potential. This dependence allows us to deduce the interaction energy shift from the measurement of tunneling times.

5 Experimental Setup

We use two fundamental properties of a degenerate Fermi gas to prepare the few-particle systems: According to Pauli's principle each state can be occupied with one fermionic atom per spin state. Furthermore, the occupation probability for the lowest states approaches unity according to Fermi-Dirac statistics. Therefore the lowest states are occupied with one fermionic atom per spin state. This allows us to control the number of particles by controlling the number of occupied quantum states. Our approach, the spilling technique, is to choose the occupied quantum states by tilting the confining potential in such a way that only a well defined number of states remains bound.
To prepare a system in which the lowest states are occupied with high probability we use a property of the Fermi-Dirac distribution: the occupation probability increases the lower the state's energy is compared to the Fermi energy. This allows us to enhance the occupation probability of the lowest states by increasing the Fermi energy of the system. We realize this by starting with a reservoir of cold atoms trapped in an optical dipole trap and enhance its Fermi energy by superimposing a deep microtrap with this reservoir.
To successfully apply the spilling technique we need to choose occupied quantum states on a single state level which requires a small-sized microtrap as discussed it will be discussed in this chapter.
This chapter presents the experimental implementation of both the reservoir and the microtrap with a strong emphasis on the microtrap setup which is the focus of this thesis. One of the major experimental challenges is to probe the few-particle systems on a single particle level. Our technique of using a magneto-optical trap as a single atom detector is described. It closes with a description of a high-resolution objective which has been designed during this thesis. Considerable effort has been put into this design with the goal to improve the control and the tunability of the system in several ways: First, the objective allows us to create a smaller microtrap. As this increases the level of control over the occupied quantum states in the potential, it should improve the preparation fidelity of the few-particle systems significantly. Second, we will be able to explore tunable quantum systems in two and three dimensions in a variety of trapping geometries such as periodic potentials.

5.1 Design goals

A major design goal of the experimental setup is to allow a high-fidelity preparation of few-particle systems. For this one important requirement is the small size of the microtrap as it will be discussed in section 5.6.1. To obtain a small-sized dipole trap a Gaussian laser beam is focused using a high-resolution objective. The size of the microtrap is determined by the resolution of the objective which is given by

$$r = 1.22\frac{\lambda}{2\,\mathrm{NA}} \tag{5.1}$$

where λ is the wavelength of the light and $\mathrm{NA} = \sin\theta$ the numerical aperture of the objective which has an opening angle of 2θ. Therefore the realization of a small microtrap requires good optical access to the vacuum chamber where the experiments are performed.
Another prerequisite for high-fidelity preparation is that the timescale for collisions of the sample with background gas atoms is much longer than the timescale for preparation and detection of the sample. To meet this condition, the vacuum pressure in the experimental chamber has to be sufficiently low. In current state of the art experiments [Bak09, She10], a lifetime of $t \approx 60\,\mathrm{s}$ is main factor which limits the detection efficiency. Although the $1/e$-lifetime of atoms in our magneto-optical trap exceeds 250 s, this is just large enough not to limit the detection fidelity of samples with up to ten atoms as shown in chapter 5.5.
Another major design goal for the whole apparatus was to fulfill those requirements with a setup as simple as possible since a simpler setup is easier to assemble, debug and maintain.

5.2 Vacuum chamber

The vacuum chamber is designed to ensure long lifetimes of the prepared samples and provide large optical access. A sketch of the complete vacuum chamber is shown in figure 5.1. As the hot lithium oven leads to an increase in pressure, the oven chamber is separated from the experimental chamber via a differential pumping tube to be able to reach a low pressure where experiments are performed. To pump a broad range of gases a combination of pumps is used. Reactive gases like H_2 are gettered with two titanium sublimation pumps which coat the surface of the two CF100 crosses in both chambers. Two ion pumps efficiently pump non-reactive gases such as noble gases. As the pumping speed in the heart of the experimental chamber, the spherical octagon, is limited by the conductance of a CF40 flange an additional pumping technique is used. The walls of the octagon

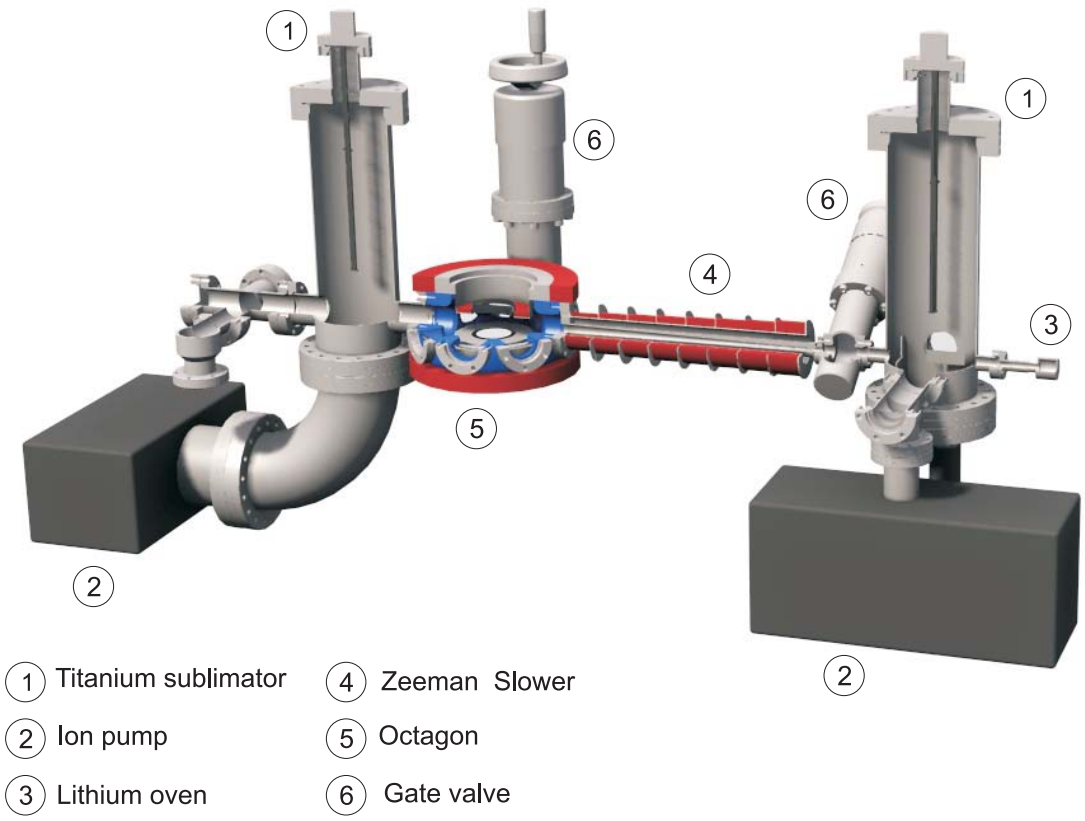

Figure 5.1: Complete vacuum system. To be able to reach low background pressure in the presence of the hot lithium oven, the vacuum system is divided into two parts which are connected via a differential pumping tube. In this way samples with lifetimes exceeding 250 s can be prepared in the spherical octagon where the experiments are performed. From [Ser07].

are coated with a non-evaporable getter coating (NEG). Its great advantage is that it lowers the pressure directly where the experiments are performed. With these three pumping techniques a vacuum on the order of $p \approx 10^{-12}$ mbar is reached which is sufficiently low not to limit the detection fidelity (see chapter 5.5).
The second requirement for the vacuum setup, large optical access, is provided by reentrant view ports attached to the spherical octagon. A picture of the octagon with the view ports is shown in figure 5.2. They allow a numerical aperture of NA= 0.65 which is large enough to focus the laser beam for the microtrap to a waist of $w_0 < 1\mu$m. This is sufficient to prepare few-particle systems with high fidelity as discussed in chapter 5.6.1.

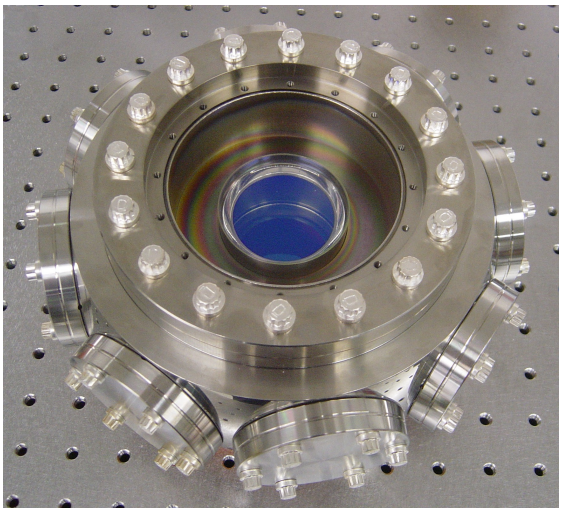

Figure 5.2: Octagon with reentrant view ports. The reentrant view ports provide optical access under a large solid angle. This allows a high numerical aperture NA = 0.65 for atom detection and for focusing the microtrap beam to a waist $w_0 < 1\,\mu$m. They also provide space for mounting the Feshbach coils close to the atoms. This minimizes the power the high magnetic fields require to tune the inter-particle interactions.

5.3 The reservoir

To reach a high occupation probability for the lowest states of the potential we prepare a reservoir of cold atoms and enhance its Fermi energy by superimposing a deep microtrap as discussed in section 4.1.1. For this, the reservoir has to fulfill two major requirements with respect to the number of atoms and its degree of degeneracy:
First, the maximum enhancement is achieved only if the width of Fermi edge, which is determined by the temperature, is not increased when both traps are combined as sketched in figure 4.2. In order to preserve this temperature the number of atoms which fit into the microtrap has to be small compared to the number of atoms in the reservoir. In the current setup, the microtrap holds about 600 atoms in two states before the spilling process is applied. Experimentally, we found that a reservoir consisting of 10^4 atoms per spin state is sufficiently large to obtain a high occupation probability for the lowest states.
Second, the occupation probability for the lowest states of the combined system depends on the initial degree of degeneracy of the reservoir. Thus the degree of degeneracy of the reservoir has to be high enough to reach an occupation probability which is close to one for the lowest states of the combined system. A reservoir

which is mildly degenerate with $T/T_F \sim 0.5$ fulfills this requirement.
The following section briefly describes the preparation of the reservoir. A detailed description can be found in previous theses, for example in [Lom11].
Starting point is an effusive lithium oven where lithium is vaporized into the gas phase by heating the sample. This creates an atomic beam with particle velocities corresponding to $T_{\text{initial}} \sim 10^3\,\text{K}$. To reach the final temperature the atom's kinetic energy has to be reduced by 9 orders of magnitude. This is done in two steps. First a source of cold atoms is prepared by laser cooling techniques which are briefly discussed. Final part of this cooling stage is the magneto-optical trap which contains 10^8 atoms at $T = 0.5\,\text{mK}$. These atoms are transferred into the optical dipole trap where evaporative cooling is performed to prepare the final reservoir.

5.3.1 Cold atom source

Laser cooling

A source of cold atoms is required to load the optical dipole trap in order to prepare the reservoir. The preparation of the cold atom source exploits the spontaneous force which acts on an atom due to absorption and spontaneous emission of photons. The absorption of a photon from the laser-field changes the atoms momentum by

$$\Delta \boldsymbol{p}_{\text{atom}} = \boldsymbol{p}_{\text{photon}} = \hbar \boldsymbol{k} \tag{5.2}$$

Because the subsequent spontaneous emission is isotropic, the momentum transfer gained in the emission process averages to zero. Hence, the spontaneous force acting on an atom can be written as

$$\langle \boldsymbol{F} \rangle = \hbar \boldsymbol{k} \gamma_p \tag{5.3}$$

where γ_p is the scattering rate. The scattering rate depends on the detuning of the laser with respect to the atomic transition $\delta = \omega_0 - \omega_{\text{laser}}$, where ω_0 denotes the frequency of the atomic transition. Its magnitude is given according to [Met99]

$$\gamma_p = \frac{s_0 \gamma/2}{1 + s_0 + (2\delta/\gamma)^2} \tag{5.4}$$

where γ is the natural line width of the transition and s_0 is the saturation parameter given by $s_0 = I/I_{\text{sat}}$ where I is the laser intensity and $I_{\text{sat}} = \hbar\omega_0^3\gamma/(12\pi c^2)$. For ^{6}Li, $\gamma = 2\pi \cdot 5.7\,\text{MHz}$ and $I_{\text{sat}} = 2.54\,\text{mW/cm}^2$.
The maximum force which can be achieved is given $F_{\text{max}} = \hbar k \gamma/2$ leading to a deceleration of $a_{\text{max}} \approx 10^5\, g$. Although the momentum change of the atom caused by the absorption of a single photon is tiny a lithium atom can be slowed down from 1000 m/s to 10 m/s within a distance on the order of 1 m.

Zeeman Slower

In the simplest scenario the spontaneous force is applied by sending a laser beam counter-propagating to an atomic beam. As the atoms in the atomic beam move with a velocity v, their transition frequency becomes Doppler shifted by an amount of $\delta_v = -kv$, where k denotes the wave vector of the laser beam. Thus, the laser has to be red-detuned by the same amount in order to decelerate the atoms. As soon as the atoms decelerate their Doppler shift changes leading to a decrease in scattering rate according to equation 5.4 which prevents further deceleration. To compensate for the changing Doppler shift during the deceleration we use the Zeeman effect to shift the atomic resonance frequency such that the atoms remain resonant during the whole deceleration process. The device which provides the required magnetic fields is called a Zeeman slower. The shape of the required magnetic field and the properties of the Zeeman slower which we use in the experiment are discussed in [Ser07].

Magneto-optical trap

In three dimensions atoms can be slowed down by means of 6 counter-propagating laser beams which are red detuned with respect to the atomic transition frequency. Higher velocities of the atoms lead to decreasing detuning with respect to the counter-propagating beam which increases the spontaneous force acting on the atoms. This result in a damping force which is proportional to the atoms' velocity in the regime of low light intensities. Therefore this scheme is called an optical molasses.
To add a spatial confinement, the force has to become not only velocity- but also position-dependent. As the force only depends on the scattering rate, a spatial varying scattering rate is sufficient to create the confinement. Such a configuration is realized within a magneto-optical trap (MOT). A magnetic quadrupole field is applied which causes an increase in the magnetic Zeeman shift which is proportional to the distance of the atoms from the zero of the magnetic field. The larger the distance of an atom from the center becomes the more photons are scattered. When circular polarized light is used the atoms absorb more photons from the beam that pushes them to the center of the trap. The minimum temperature which can be achieved in a magneto-optical trap depends on the equilibrium of cooling force and heating due to spontaneous emission. For low saturation intensities this value is given as [Met99]

$$T_D = \frac{\hbar\gamma}{2k_B}. \tag{5.5}$$

For Lithium, the Doppler temperature has a value of $T_D = 140\,\mu$K. In principle there exists techniques to overcome this limit such as polarization gradient cooling. However these techniques cannot be applied to Lithium because of its light mass. A fundamental limit poses the increase in energy due to the absorption of a single photon given by the recoil temperature

$$T_R = \frac{\hbar^2 k^2}{2k_B m}. \tag{5.6}$$

For lithium, the recoil temperature takes a value of $T_R = 3.5\,\mu K$.
Our magneto-optical trap is able to load 10^8 atoms/s at a temperature of 0.5mK. A detailed description can be found in [Ser07]. For most experiments we start with 10^8 atoms which requires a loading time of 1 s. To reduce the temperature of the sample below the Doppler limit, evaporative cooling in an optical dipole trap is performed.

Laser system

Following previous considerations, a laser system is required which provides light with a variable detuning with respect to the atomic transition. Furthermore, to apply laser cooling techniques the detuning of the laser has to be controlled with a precision which is small compared to the natural line width of $\gamma = 2\pi \times 5.8\,$MHz. These conditions are met by grating stabilized diode lasers (DL100 Toptica) which emit on a single longitudinal mode. In this configuration, a laser diode and a grating form a cavity whose length and therefore the output wavelength is controlled by moving the position of the grating with respect to the diode using a piezoelectric actuator. As a frequency reference we stabilize one diode laser using the technique of Doppler free spectroscopy of ^{6}Li in a vapor cell to the $F = 3/2 \rightarrow F' = 5/2$ transition (see figure 5.3). The other diode lasers are stabilized with respect to the reference laser by a beat offset locking technique [Sch98, Ser07, Lom08], which allows us to change the detuning of the laser with respect to the transition frequency dynamically.

A further requirement on the laser system is to provide sufficient output power in order to saturate the atomic transitions in all optical beams. For lithium the required saturation intensity is $I_{\text{sat}} = 2.54\,$mW/cm. As the output power of our diode lasers is limited to $P \sim 25\,$mW we use an amplifier chip (Toptica, TA100) to obtain $P \sim 400\,$mW of total power with the spectral properties of the seeding diode laser.
We use the $F = 3/2 \rightarrow F' = 5/2$ transition for laser cooling. However, as the excited hyperfine states cannot be resolved (see figure 5.3), the probability for the atom to decay into the $F = 1/2$ ground state manifold is significant: the optical

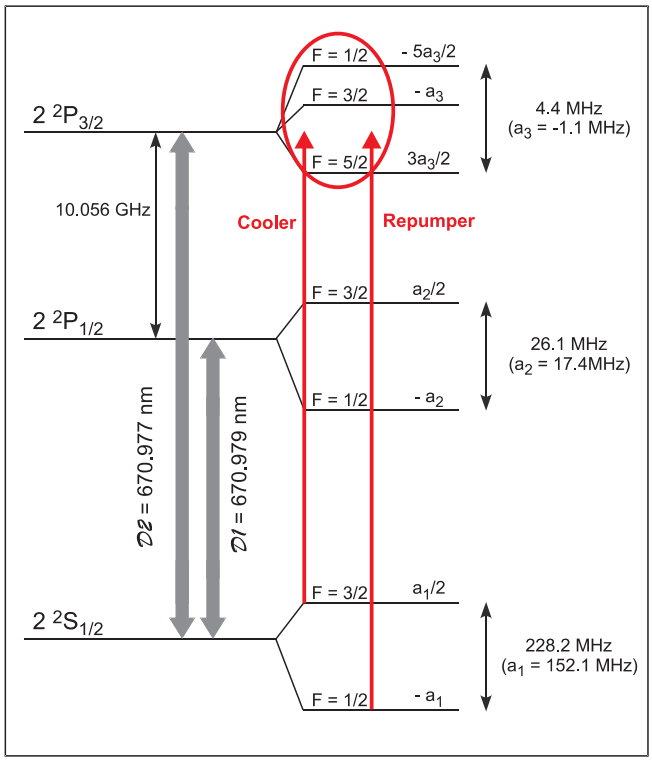

Figure 5.3: Level scheme of ^{6}Li. For laser cooling the D_2 transition is used. Due to the natural line-width of the transition of 6 MHz the excited hyperfine states are not resolved. As the decay probability into the $F = 1/2$ manifold of the ground state is significant, a re-pump laser is required.

transition is not closed. Therefore a re-pump laser is required. To obtain both frequencies with a single laser we lock the diode laser seeding the TA to the crossover between the two ground state manifolds and split the output light into two parts. We generate the two frequencies by shifting the frequency of one part of the light by -114 MHz (cooler) and the second part by $+114$ MHz (re-pumper) using of two acousto-optical modulators (aom). They also allow us to control the intensity of cooler and re-pumper light. This is a crucial requirement for the operation of the magneto-optical trap as single atom detector as described in section 5.5. We combine the parts containing the two frequencies again into a single beam which is coupled into fibers to distribute them to the experiment.

5.3.2 Optical dipole trap

To perform evaporative cooling atoms are transferred from the magneto-optical trap into an optical dipole trap. This trap creates a conservative potential whose strength is proportional to the spatial intensity distribution of the trapping light as discussed in section 3.2.
In the experiment the dipole trap is formed by two laser beams ($\lambda = 1070\,\mathrm{nm}$) focused to a waist of $w_0 = 40\,\mu\mathrm{m}$ and both crossed at an angle of 15°. We transfer about 1% of the atoms, i.e.10^6 atoms from the MOT into the dipole trap. We remove the hottest atoms of the sample by reducing the depth of the dipole trap by lowering the intensity of the trapping light using an acousto-optical modulator (aom) over a couple of seconds. A detailed description of the evaporation process can be found in [Lom11]. As the efficiency of evaporative cooling crucially relies on the time the sample needs to thermalize high elastic collision rates are required. Since the cross section for identical fermions vanishes, as discussed in chapter 3.1, we use a mixture of atoms in two different hyperfine states ($|1\rangle$ and $|2\rangle$, see chapter 3.1) in order to perform evaporative cooling. To obtain a high collision rate we tune the inter-particle interactions using a Feshbach resonance. The final number of atoms in the sample and its degeneracy depends on the efficiency of the evaporation process. In principle this efficiency is maximized by evaporating in the vicinity of the Feshbach resonance. However, for a large positive scattering length a molecular bound state is populated if the temperature of the sample becomes comparable to the binding energy of the molecule. Evaporating in this regime leads to the formation of bosonic molecules which can form a molecular Bose-Einstein condensate. In our apparatus we can prepare condensates consisting of 150000 molecules at a temperature of 100 nK.
To prepare a degenerate Fermi gas, the population of the molecular branch has to be avoided. We reach this by starting the evaporating close to the resonance. Before the formation of molecules sets in we continue the evaporation with a negative value of the scattering length ($B = 300\,\mathrm{Gauss}$) because there is no molecular bound state which can be populated. Using this technique we prepare degenerate Fermi gases consisting of 75000 atoms per state with $T/T_F \approx 0.28$. These are the starting point for our previous experiments.
In order to prepare the reservoir for loading the microtrap we perform the complete evaporation at a field of $B = 300\,\mathrm{Gauss}$. The final system consists of $N \approx 2{\cdot}10^4$ atoms per spin state at a temperature of $T \lesssim 250\,\mathrm{nK}$ which corresponds to $T/T_F \approx 0.5$. This is completely sufficient for the preparation of few-particle systems as it will be discussed in the next chapter.

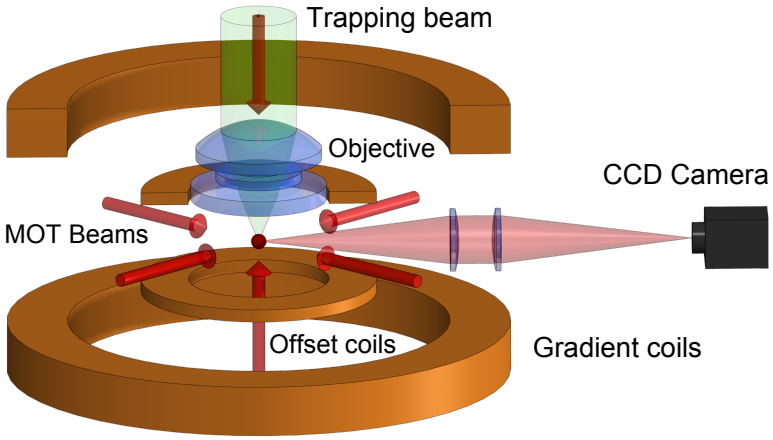

Figure 5.4: Microtrap setup. Systems with up to 10 fermions are prepared with ^{6}Li atoms in a micrometer sized optical dipole trap created by the focus of a single laser beam. The number of atoms in the sample is detected with single atom resolution by transferring them into a magneto-optical trap and collecting their fluorescence on a CCD camera. A Feshbach resonance allows us to tune the interaction between the particles with a magnetic offset field.

5.4 The microtrap

The key elements of the experimental setup which are required to create a tunable few-particle system are presented in figure 5.4. After a brief summary this section describes the parts in detail.
Heart of the setup is the trapping beam which is focused with a high-resolution objective to create the microtrap. To perform the spilling process, the gradient coils are used to apply a magnetic field gradient in z-direction. The interactions between the particles are tuned by means of a magnetic Feshbach resonance. Therefore large homogeneous offset fields are required which are created by the offset coils. To detect the samples on a single atom level, they are transferred into the magneto-optical trap where their fluorescence signal is recorded via a CCD camera.
The setup for focusing the trapping beam to create the microtrap is shown in figure 5.5. To obtain a focus as small as possible, a clean Gaussian beam is required. Therefore the setup is divided into two parts connected with a single mode polarization maintaining optical fiber (Thorlabs P3-1064PM-FC-5) which cleans the beam profile. The part before the fiber (left panel of figure 5.5) is referred to as 'low noise trapping light source', the part after the fiber as 'focusing setup'.

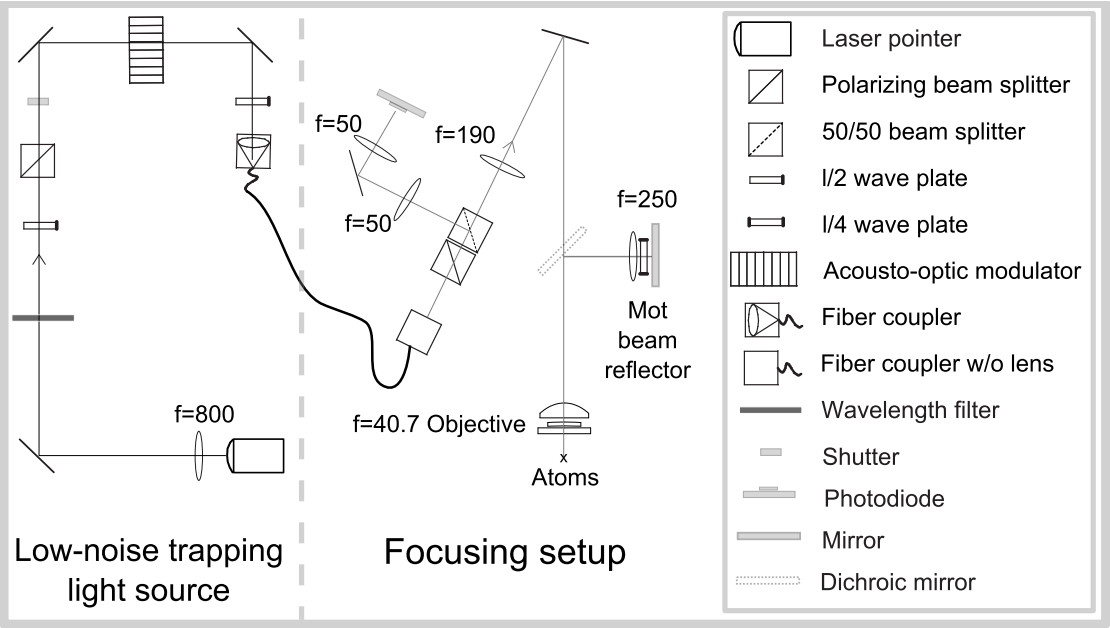

Figure 5.5: The microtrap setup. To obtain a clean beam profile and pointing stability for the microtrap beam, the setup is divided into two parts which are connected with an optical fiber. The intensity of the microtrap beam after the fiber is monitored with a photo diode and stabilized by means of an acousto-optical modulator.

5.4.1 Low-noise trapping light source

A high preparation fidelity requires intensity stability of the optical potential because intensity noise directly translates into a variation of tunneling times of the bound states in the tilted potential. This variation hinders the deterministic application of the spilling scheme.
According to WKB calculations (figure 5.17), the required relative intensity stability for a trap with a waist of $w_0 = 1.8\mu$m as used in the experiment is on the order of 10^{-3}. Therefore, an intensity stabilization scheme which is significantly more accurate than 10^{-3} is required. The scheme has to work in two different frequency domains: First, the system is extremely sensitive to noise with a frequency on the order of the trap frequency, i.e. up to 100 kHz. Therefore, it is essential to minimize the noise in this frequency band. Furthermore, long-term drifts have to be minimized because they cause shot-to-shot variations of the tunneling times of the system in the tilted potential which degrades the overall preparation fidelity of the system.
The required intensity stability is reached by using a laser with low intrinsic in-

tensity noise in combination with an intensity stabilization scheme.

Microtrap laser

As light source with low intrinsic noise we use a green laser pointer (100 mW http://greenlaserdepot.com) as it is used in presentations. A sketch of its interior is shown in figure 5.6. It contains a laser diode emitting at $\lambda_p = 808\,\text{nm}$ pumping a

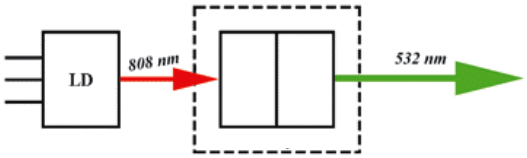

Figure 5.6: Working principle of a green laser pointer. A laser diode emitting at $\lambda = 808\,\text{nm}$ pumps a Yttrium orthovanadate crystal which is doped with neodymium. The crystal emits at $\lambda = 1064\,\text{nm}$ which is frequency doubled to green light $\lambda = 532\,\text{nm}$ by means of a nonlinear crystal. Image from [CAS].

Yttrium orthovanadate crystal which is doped with neodymium (Nd:YVO4). This active medium emits light at $\lambda = 1064\,\text{nm}$ which is frequency doubled to green light at $\lambda = 532\,\text{nm}$ with a nonlinear crystal. As the reflectivity does not reach 100% for $\lambda = 1064\,\text{nm}$ at the output facet of the crystal, the laser pointer also emits $P \approx 4\,\text{mW}$ at $\lambda = 1064\,\text{nm}$. At this wavelength, the laser runs on a single longitudinal mode. A characterization of the laser can be found in [Haf11].
To have as much laser light available for trapping as possible, high fiber coupling efficiency is desired. Therefore the diameter and divergence of the beam is matched to the lens of the fiber coupler (Thorlabs C240TME-B) by means of a lens with $f = 800\,\text{mm}$ placed directly in front of the laser pointer. In this way fiber coupling efficiencies exceeding 50% are reached. A color filter which only transmits light at $\lambda = 1064\,\text{nm}$ (Thorlabs FGL610S) is used to remove the green light. A picture of this setup is shown in figure 5.7. After the filter, a polarizing beam splitter is used to clean the polarization of the beam. This makes the setup more robust against polarization drifts which is crucial to stabilize the intensity of the microtrap. The intensity of the beam is controlled with the acousto-optical modulator (see below). For fine alignment of the beam polarization with respect to one of the main axes of the polarization maintaining fiber a $\lambda/2$-plate is placed directly in front of the fiber coupler.

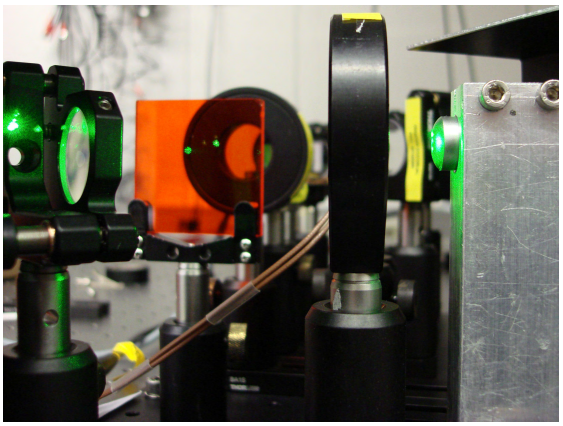

Figure 5.7: Laser pointer as low-noise light source for the microtrap beam. The green light ($\lambda = 532\,\mathrm{nm}$) is removed with a wavelength filter (red glass) leaving only the fundamental wave($\lambda = 1064\,\mathrm{nm}$) which is coupled into a fiber. The intensity noise of the output light is low enough to allow a high fidelity preparation process.

Intensity stabilization

To stabilize the intensity of the microtrap, the intensity of the light after the fiber is monitored with a photo diode (Hamamatsu G8370-81) whose output signal is fed into a digital PID-controller. Details of the implementation of the PID-controller can be found in [Zür09]. Deviations from the set value are corrected by adapting the laser intensity before the fiber with an acousto-optical modulator (Crystal Technology 3110-197). The light intensity is controlled by adjusting the amplitude of the radio-frequency (rf) signal which causes the sound wave in the aom. The aom requires a 110 MHz radio-frequency (rf) signal for optimum diffraction efficiency which is generated with a voltage-controlled oscillator (VCO). A sketch of the stabilization scheme is shown in figure 5.8. To control the rf-intensity at high bandwidth and large dynamic range we multiply the output of the PID-controller with the output of the radio-frequency source using two mixers. Parameters of the PID loop can be optimized over the whole dynamic range if the feedback loop has a linear response. Therefore we compensate the non-linear characteristic of the two mixers by using a look-up table in the PID loop. This can be realized since the PID controller is implemented digitally.
The noise suppression is evaluated by taking the Fourier transform of the photo diode voltage using a digital oscilloscope (TiePie HS3). In the frequency range up to 100 kHz, which is large compared to typical trap frequencies of $1 - 30$ kHz, the scope shows a noise level of $(20 \log \Delta U/1\mathrm{V}) = -70$ where U is the output voltage

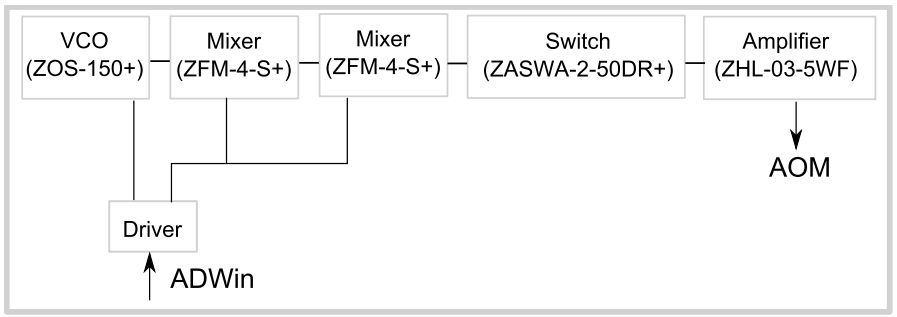

Figure 5.8: Setup to control the acousto-optical modulator (aom). To obtain high bandwidth and large dynamic range we use two mixers to control the radio-frequency signal which is fed into the aom. Parts from Mini-circuits.

of the photo diode. This corresponds to relative intensity noise

$$\mathrm{RIN} = \frac{\left\langle \delta P_{\mathrm{opt}}^2 \right\rangle}{P_{\mathrm{opt}}^2} \frac{1}{\mathrm{Hz}} = \left(\frac{\Delta U}{U} \frac{1}{\sqrt{bs}} \right)^2 = -116 \frac{\mathrm{dB}}{\mathrm{Hz}} \tag{5.7}$$

where $\left\langle \delta P_{\mathrm{opt}}^2 \right\rangle$ is the mean-square optical intensity fluctuation in a 1-Hz bandwidth, P_{opt}^2 denotes the square of the average optical power and bs the bin size of the scope in the frequency domain. For comparison, a commercially available low-noise light source (Innolight Mephisto) reaches values of RIN$< -130\,\mathrm{dB/Hz}$ in the same frequency band. To evaluate long term drifts, we measured the laser intensity by means of a second photo diode which placed in the focus of the objective. For a measurement duration of 10 hours, we achieve a relative intensity stability of $5 \cdot 10^{-4}$ between the two photo diodes.
To reach this level of accuracy several hurdles had to be overcome. First, it is crucial to remove the cover glass of the photo diodes because interference effects due to reflections from the cover glass result in intensity drifts. The second source of error is caused by polarization drifts of the light source. Although we used a polarization-maintaining fiber with a polarizing beam splitter at its entrance port it turned out to be necessary to clean the polarization after the fiber by means of a second polarizing beam splitter. In addition, the out-coupling of the light for the PID photo diode after the fiber has to be made as robust to polarization drifts as possible. This is fulfilled when a polarization drift causes only a low relative change in intensity on the photo diode. Therefore we use a 50/50 non-polarizing beam splitter which reflects a significant portion of the light and whose reflectivity is almost the same for s and p polarization.

wavelength	1064 nm	671 nm
focal length	40.7 mm	
image distance	∞	2570 mm
field of view (diameter)	200 μm	
max. diffraction limited NA	0.44	0.27
entrance aperture at max NA (diameter)	36 mm	22 mm
resolution	1.4 μm	1.5 μm
waist of the focus	0.9 μm	1 μm

Table 5.1: Design parameters for the focusing objective.

5.4.2 The focusing setup

The main goal of the optical setup after the fiber is to create the small focus which is required to prepare the microtrap. This is done by collimating the beam after the optical fiber with a $f = 190\,\text{mm}$ doublet (CVI Melles Griot LAI-190.0-50.0) and focusing it using the $f = 40.7\,\text{mm}$ focusing objective.
Additionally, the setup provides a monitoring port for the intensity stabilization. To pick up a significant portion of the beam a 50/50 non polarizing cube (Edmund Optics 49005) is placed after the polarizing beam splitter which eliminates the effects of polarization drifts.
The objective has been designed using the optical design software OSLO. In the following, the design of the focusing objective is discussed as well as its measured performance. Furthermore the integration into the optical setup for the MOT is described.

Design parameters for the objective

The focusing objective has been designed to meet several requirements. First, the setup has to be as simple as possible. Therefore the number of optical elements should be minimized and commercially available catalog lenses are preferred. Furthermore, the magnification of the setup should be flexible. For that reason an infinite conjugate design has been chosen to be able to change the magnification by simply choosing a different second lens. This design has also the advantage that optical elements like dichroic mirrors for imaging purposes can be inserted into the path between the objective and the second lens without degrading the performance of the objective which was not possible with the previous design (see [Ott10]).

To obtain high preparation fidelity, the system should be optimized to create a small focus at $\lambda = 1064\,\text{nm}$. The size of the focus should be much smaller than the

size of the focus of the previous objective with $w_0 \sim 3\mu$m. At the same time the objective should have a decent imaging performance at $\lambda = 671\,$nm. The setup should be also easy to align, which requires a large field of view.
Before the actual design is discussed a brief overview over relevant parameters is given. The diffraction-limited resolution of an imaging system is given as

$$r = 1.22\frac{\lambda}{2\mathrm{NA}} \tag{5.8}$$

where NA denotes the numerical aperture. This value corresponds to the distance from the maximum to the minimum of the objective's point-spread-function (psf) which is given as an Airy function for a diffraction limited objective.
The waist of the focused Gaussian laser beam is defined as the $1/e^2$-radius of the intensity distribution. It depends on the illumination of the entrance pupil of the objective [Cvi]. Therefore, the $1/e^2$-radius of the image spot can be written as

$$w_0 = K\frac{\lambda}{2\mathrm{NA}}, \tag{5.9}$$

where K is a constant depending on the illumination of the entrance pupil. Only for a uniformly illuminated pupil, the intensity distribution in the image plane is given by the Airy function. If the entrance pupil is illuminated with a Gaussian intensity distribution the side maxima of the Airy pattern vanish but also the $1/e^2-$radius of the focus increases. For a qualitative analysis it is useful to define a truncation ratio

$$T = \frac{w_{\mathrm{ap}}}{r_{\mathrm{ap}}} \tag{5.10}$$

where w_{ap} is the waist of the Gaussian beam at the objective's aperture which has a radius of r_{ap}. For a given truncation ratio the value of K can be calculated using the formula [Cvi]

$$K(T) = 0.82 + \frac{0.32}{(T-0.28)^{1.82}} - \frac{0.27}{(T-0.28)^{1.89}}. \tag{5.11}$$

Values for K for $T = 0, 0.5, 1, 2, \infty$ are shown in table 5.2. For a Gaussian beam with a waist which is equal to the aperture radius the truncation becomes $T = 1$. Thus the waist in the focus will be about 12% larger compared to a uniformly illuminated case. The important relation between the imaging resolution and the $1/e^2$-radius of the point spread function is given by $K(\infty)/1.22 = 0.67$.
Starting point for the design was a high numerical aspheric lens with long working distance (Thorlabs AL5040) to be able to insert further elements between the lens and the view port. The lens is designed for $\lambda = 780\,$nm and works diffraction

Truncation ratio	spot size [λ/2NA]
∞	0.82
2	0.85
1	0.92
0.5	1.26

Table 5.2: $1/e^2$-spot size and truncation ratio. The resolution according to the Rayleigh is defined as $1.22\lambda/2\text{NA}$.

Radius 1	245.39 mm
Radius 2	600 mm
Thickness	4 mm
Focal length	800 mm
Material	BK7
Distance to aspheric lens	4.3 mm

Table 5.3: Properties of the meniscus lens (JML OPTICAL CMN11281).

limited up to NA= 0.55. However the diffraction-limited numerical aperture for $\lambda = 1064\,\text{nm}$ is significantly reduced to NA= 0.35. In addition, the 6 mm thick fused silica window of the reentrant view port introduces aberrations and degrades the performance further. This limits the numerical aperture to NA= 0.22. Placing an additional element between aspheric lens and view port provides the degrees of freedom to bring the diffraction limited performance up to NA= 0.44. Closest to the ideal solution comes a positive meniscus lens (JML OPTICAL CMN11281, for details see table 5.3). A sketch of the objective is shown in figure 5.9. As the meniscus lens is only available with 50 mm diameter, its diameter was reduced using a lathe to 34 mm to fit into the mount. With this lens configuration, the parameters of the nominal system are given in table 5.1. According to the final design parameters, the trapping beam can be focused to a waist of $w_0 < 1\,\mu\text{m}$ which is sufficiently small to prepare few-particle systems at high fidelity.
The lenses are mounted within an aluminum tube as shown in figure 5.10. The right distance between the aspheric lens and the meniscus lens is set by a spacer which also centers the meniscus lens with respect to the optical axis. The aspheric lens is centered to the same axis via a tube which is fixed by means of a retaining ring. As the alignment of the objective requires the degree of freedom to tilt it with respect to the optical axes and translate it in three directions we mount the objective using a 5-axis mount (Newport LP2a) whose stability we increase by enforcing it with additional aluminum sheets. Although the adjustment of the focus in z-direction causes a tilt of the objective with respect to the optical axes,

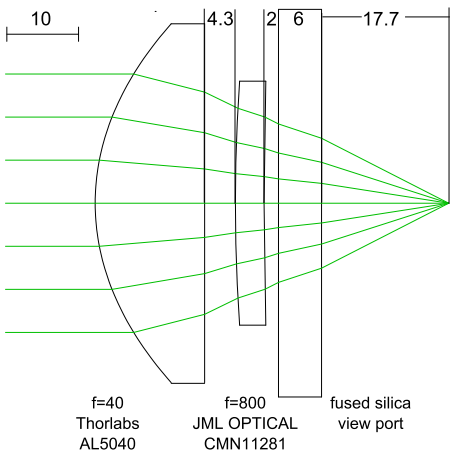

Figure 5.9: The objective consists of two elements, one aspheric lens and a positive meniscus lens which compensates spherical aberrations caused by the vacuum view port. It is designed to focus the trapping light to a waist of $w_0 \sim 1\,\mu$m in order to create a small volume dipole trap. Units in mm.

the mount has the main advantage that it is stable. Therefore, we need to realign the microtrap only every four months.

Performance test

The performance of the objective was evaluated in two steps as sketched in figure 5.11. In a first setup, the point spread function of the objective was determined by imaging an object whose extension is small compared to the targeted resolution. The imaging resolution can be directly determined from the intensity distribution of the corresponding image. It is given as the distance between the maximum intensity to the first minimum of the Airy disc. To extract this distance, a 2-D Gaussian is fitted to the intensity distribution of the image. From the fit parameter the $1/e^2$ radius w_{fit} was obtained and the imaging resolution was calculated according

$$r = 1.22/K(\infty) \cdot 1/M \cdot w_{\mathrm{fit}} = 1.5/M\, w_{\mathrm{fit}}, \tag{5.12}$$

where M is the magnification of the system.
To measure the magnification, the object was displaced in the x, y-plane perpendicular to the optical axis. The magnification is obtained via $M = d_{\mathrm{i}}/d_{\mathrm{o}}$ where $d_{\mathrm{o}}(d_{\mathrm{i}})$ is the distance the object (image) translates. For the magnification a value of $M = 20.3 \pm 1.2$ was measured where the error stems from the uncertainty in the position of the translation stage. Within two standard deviations, the measured

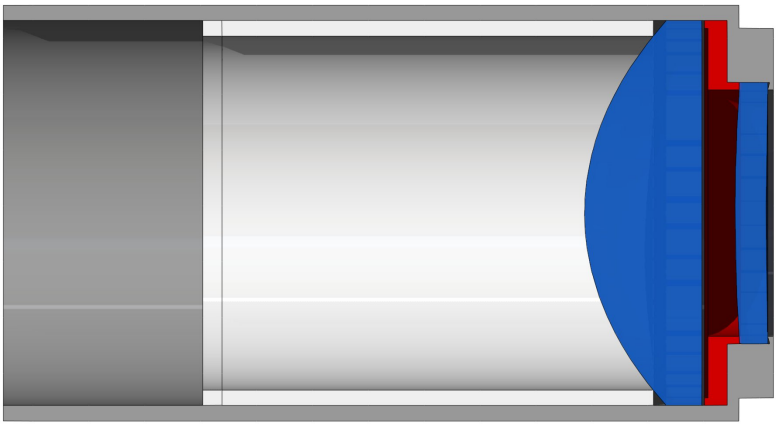

Figure 5.10: Mount for the lenses of the focusing objective. The right distance between the aspheric lens and the meniscus lens is set by a spacer (red) which also centers the meniscus lens with respect to the optical axis. The aspheric lens is centered to the same axis via a tube which is fixed by means of a retaining ring.

value agrees with the theoretical calculated from the ratio of the focal lengths $M_{\text{theo}} = 750\,\text{mm}/40.7\,\text{mm} = 18.4$.
To obtain an accurate result for the intensity distribution a high signal-to noise-ratio is desired. This is optimized when just the test object itself but not the background is transmissive. Therefore a pinhole (Data Optics) with a specified diameter of $d < 0.8\mu\text{m}$ was used as test target.
The alignment of the test setup was done in several steps which are briefly summarized in the following. The trapping laser beam defines the optical axis and all components are subsequently aligned with respect to this axis according to figure 5.11.
First, the CCD camera and an iris were aligned with respect to the trapping light. The position of the iris defines the optical axis. It is later used to align the object within the field of view of the objective. Its position was chosen to be in between the CCD and the $f = 750\,\text{mm}$ lens but as close to the lens as possible. To minimize the number of degrees of freedom, the $f = 750\,\text{mm}$ lens was added into the housing of one of the objectives. Then, the angle of the objective with respect to the optical axis was aligned by overlapping the back reflections from the flat side of the aspheric lens with the incoming trapping light. At this stage the position of the meniscus lens with respect to the aspheric lens in the housing was optimized by overlapping the back reflections of the two lenses with the trapping light. To do so, the retaining ring which fixes the lenses in the mount had to be

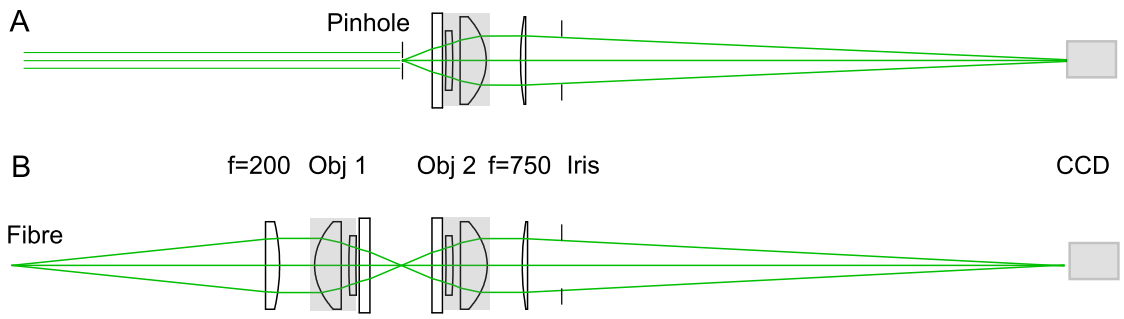

Figure 5.11: Setup for testing the performance of the objective.(A) By imaging a pinhole onto a CCD camera, the point spread function of the objective can be directly measured. (B) The focusing performance can be evaluated by imaging the focus created by one objective with a second identical one.

loosened and tightened again. The next step was to align the x, y-position of the objective with respect to the optical axis. Since a decentered objective causes an asymmetric image of the trapping light and the iris on the CCD, this image is used to optimize the position of the objective. Then the test window and the pinhole were aligned. To make sure that the pinhole's x, y-position is within the field of view of the objective, it had to be translated to the center of the optical axis which is defined by the image of the iris on the camera. Using this alignment technique, the Airy function on the camera showed slightly asymmetric side maxima which could be caused by imperfect alignment.
In order to use this objective to image the focus created by the second objective, imaging errors introduced by the first objective have to be minimized. Therefore a symmetric point-spread-function of the imaging objective is desired. We achieve this by translating the pinhole within the field of view of the imaging objective until the point-spread-function becomes symmetric. This translation only affects the side maxima of the Airy pattern, the resolution is not altered. The images of the pinhole is shown in figure 5.12 (a). We fit a 2-D Gaussian to the intensity distribution of the image to characterize the point-spread-function of the imaging objective. We obtain a resolution of $r_x = r_y = (1.6 \pm 0.1)\mu$m according to equation 5.12. Within two standard deviations the experimental value agrees with the diffraction limit $r_{\text{diff}} = 1.4\mu$m.
Then, the pinhole is removed inserting the second objective which creates the focus of the trapping beam. We image this focus with the imaging objective. The result is shown in figure 5.12 (d). We obtain an upper limit for the size of the focus $w_y = (1.3 \pm 0.1)\mu$m.

In the experiment we limit the beam diameter to $d = 30\,\mathrm{mm}$ in order to fit it through the 2" dichroic mirror which is placed at 45° with respect to the optical axis. This limits the NA for focusing to 0.37. With a truncation ratio of $T \approx 1.3$ we expect a spot size of $w_0^{\mathrm{theo}} = 1.3\,\mu\mathrm{m}$ according to equation 5.9.
According to trap frequency measurements, the focus size obtained in the experiment is $w_0 \approx 1.8\mu\mathrm{m}$ as discussed in chapter 7.2. This deviation could be caused by slight misalignment of the objective in the experiment or by the surface quality of the vacuum view port.

Integrating the objective into the MOT setup

To detect few-particle samples after they have been prepared, we transfer them from the microtrap into the magneto-optical trap. Therefore, both components must be operated at the same time. We realize this by separating the beam for the magneto-optical trap from the microtrap beam using a dichroic mirror. In order to retro-reflect the beam for the magneto-optical trap it needs to pass the objective twice. To obtain a collimated beam at the position of the MOT, additional optical elements are required. A sketch of the setup is shown in figure 5.13. The beam for the magneto-optical trap is collimated with a $f = 250\,\mathrm{mm}$ lens and retro-reflected through the objective (A). The 1" diameter of the lens limits the diameter of this beam at the position of the magneto-optical trap to $d \sim 4\,\mathrm{mm}$, which is sufficiently large to operate it in the detection mode. However, in order to load the reservoir a larger beam diameter is required. Therefore we dynamically insert the required optical elements into the optical path using a motorized stage during the loading phase of the reservoir (B). A picture of this setup is shown in figure 5.14.

5.4.3 Magnetic field coils

Two pairs of coils are used to control the few-particle systems. To perform the spilling process, a gradient field is required. The second pair of coils provides both homogeneous offset fields for tuning the inter-particle interaction and a quadrupole field to operate the magneto-optical trap as a single-atom detector.

Spilling gradient

In order to perform the spilling scheme we apply a magnetic field gradient along the z-axis. This gradient is produced by means of a pair of coils in approximately anti-Helmholtz configuration which is also used to create the magnetic field for the magneto-optical trap in order to prepare the reservoir (see section 5.3.1) [Ser07]. To spill atoms we typically apply a gradient of $B'_{\mathrm{spill}} = 18.9(2)\,\mathrm{Gauss/cm}$. This

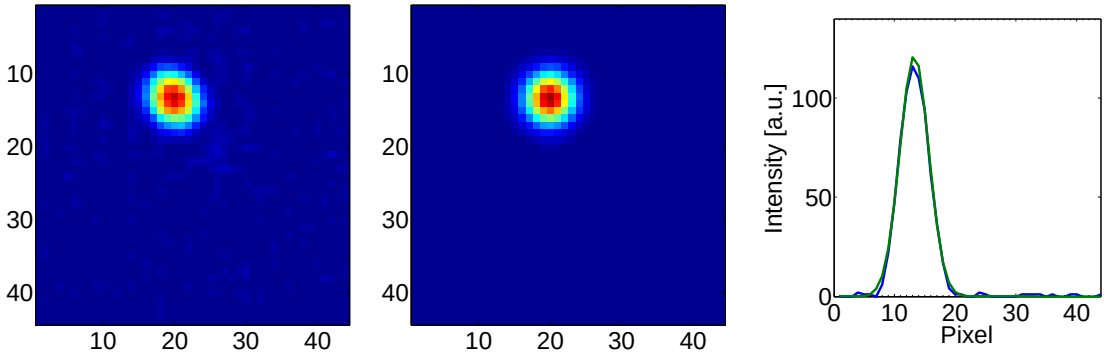

(a) Image of the pinhole.

(b) Gaussian fit to the pinhole image. Fit parameters for one standard deviation are $\sigma_x = 2.34$ pixel, $\sigma_y = 2.39$ pixel.

(c) Profile in y direction through the maximum.

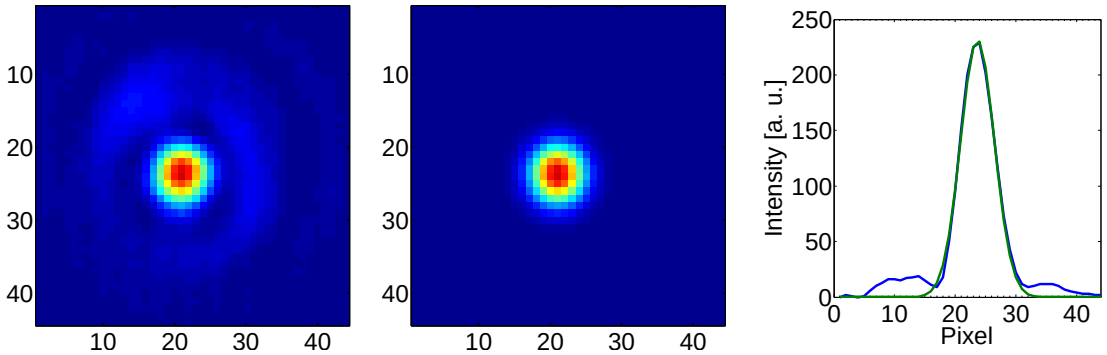

(d) Image of the focus.

(e) Gaussian fit to the focus image. Fit parameters for one standard deviation are $\sigma_x = 2.62$ pixel, $\sigma_y = 2.78$ pixel.

(f) Profile in y direction through the maximum.

Figure 5.12: Evaluation of the performance of the focusing objective. The square pixels have a width of 4.65μm, the measured magnification amounts to 20.3±1.2. The determined imaging resolution $r_x = r_y = (1.6 \pm 0.1)\mu$m agrees within two standard deviations with the diffraction limit of $r_{\text{theo}} = 1.4\mu$m. The focus has a measured waist of $w_x = (1.2 \pm 0.1)\mu$m, $w_y = (1.3 \pm 0.1)\mu$m. This size is small enough to prepare few-fermion systems with high fidelities.

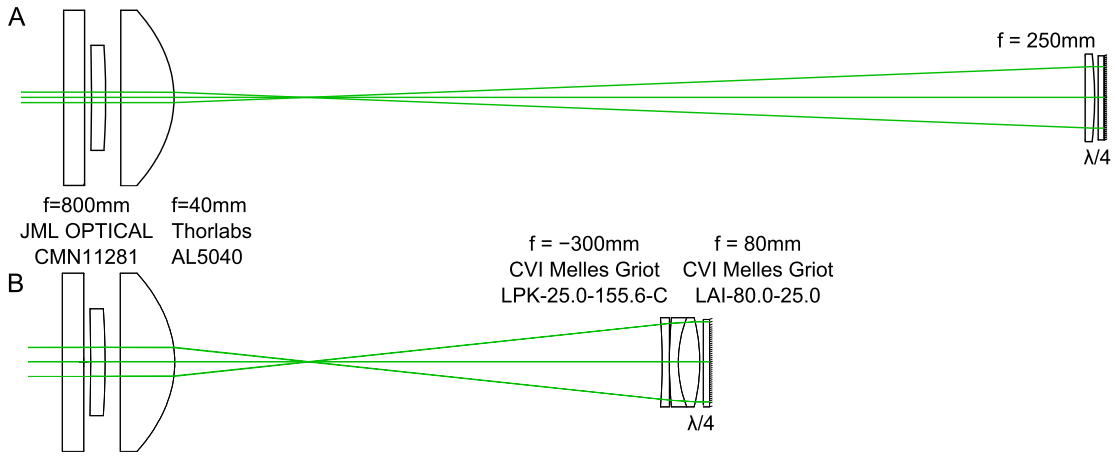

Figure 5.13: Setup for retro-reflecting the MOT beam for the detection of the prepared samples (A) and loading of the reservoir (B). To obtain a collimated beam at the MOT center a combination of lenses, a $\lambda/4$-plate and a mirror is used. During the loading phase(B), the whole assembly is inserted into the optical path using a motorized stage.

magnitude is deduced from the gradient which is necessary to levitate the atoms against the gravitational force given by $B'_{\mathrm{grav}} = mg/\mu_B$. It is worth to note that applying higher gradients does not lead to an increase in preparation fidelity as shown in figure 5.18 (b).

Feshbach field and quadrupole field

We tune the inter-particle interaction with a magnetic Feshbach resonance as described in section 3.1.2. Therefore large homogeneous fields up to 1500 Gauss have to be applied. They are created by a set of coils, the Feshbach coils, which are approximately in Helmholtz configuration. To produce these high magnetic fields high currents are required. Therefore a large amount of heat has to be dissipated. The required power is minimized by reducing the distance between the two coils as much as possible. However, the coils still produce several kW of heat, thus a sophisticated cooling scheme has been developed. A description of the Feshbach coils can be found in [Ser07, Lom08, Zür09].
To operate the magneto-optical trap as a single atom detector, a we apply a strong quadruple field with a gradient of 250 Gauss/cm as discussed in section 5.5.

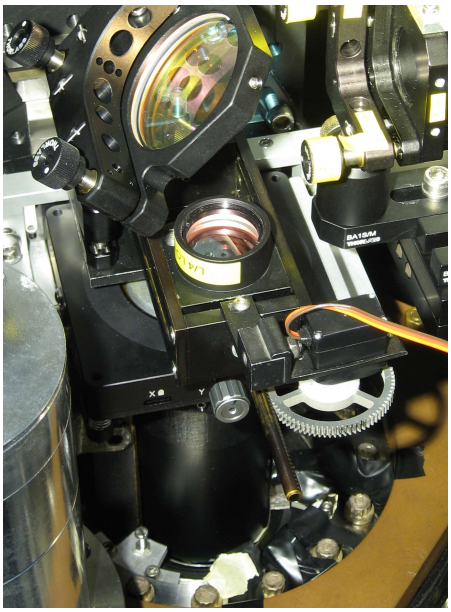

Figure 5.14: Microtrap setup. The laser beam which is focused to create the microtrap passes a dichroic mirror from above and enters the objective (black tube). To prepare the reservoir of cold atoms a motorized mirror is inserted into the beam path for operation of the magneto optical trap.

5.5 Single atom detector

We use the magneto-optical trap not only as the first stage of cooling but also as a single-atom detector. This principle was first demonstrated in [Hu94] where discrete steps in the fluorescence of a magneto-optical trap could be recorded using a photo diode. The key advantage over other detection schemes is that the observation time and therefore the number of collected photons can be made almost arbitrarily large. Ultimately, it is only limited by the lifetime of the magneto-optical trap, which is mainly determined by collisions with the background gas. In principle also light-assisted collisions of two lithium atoms can lead to a reduction of the lifetime. In our experiment the $1/e$-lifetime of atoms in the magneto-optical trap exceeds 250 s which is only limited by collisions with the background gas. Although this value seems to be more than sufficient it can be a limiting factor as the estimation of detection fidelity as a function of atom number and exposure time shows. With the value of the lifetime a maximum allowed exposure time t_{ex} can be estimated given a desired detection fidelity. The detection fidelity per atom

can be calculated according to

$$p = e^{-t_{\mathrm{ex}}/250\,\mathrm{s}}. \tag{5.13}$$

Therefore the detection fidelity of samples consisting of ten atoms amounts to

$$P = \left(e^{-t_{\mathrm{ex}}/250\,\mathrm{s}}\right)^{10}. \tag{5.14}$$

To reach a detection fidelity exceeding 98% the maximum exposure time is as short as $t_{\mathrm{exp}} = 0.5\,\mathrm{s}$. Therefore the detection setup has to be optimized to maximize the number of scattered photons within this time.
The fluorescence signal of the atoms in the magneto-optical trap is collected with a CCD camera (AVT Guppy F038B NIR) as sketched in figure 5.4. The light is collected by a plano-convex gradium lens with $f = 120\,\mathrm{mm}$ and focused on the CCD with using a plano-convex gradium lens with $f = 200\,\mathrm{mm}$. The number of collected photons is given by the solid angle covered by the first lens, which yields a numerical aperture of NA = 0.18. Therefore a fraction of 0.8% of the emitted photons is collected. With a calibration of the CCD camera of $k = 226\,\mathrm{photons/count}$ [Ott10] and a measured signal of $150\,\mathrm{counts/(atom\,s)}$ we obtain

$$N_{\mathrm{photon}} = 226\frac{\mathrm{photons}}{\mathrm{count}} \times 150\frac{\mathrm{counts}}{\mathrm{atom\ s}} \times 0.5\,\mathrm{s} = 17000\frac{\mathrm{photons}}{\mathrm{atom}} \tag{5.15}$$

which corresponds to a scattering rate of

$$\gamma = \frac{1}{0.008} 226 \times 150\,\mathrm{Hz} = 4.2\,\mathrm{MHz} \sim 0.2\frac{\gamma}{2}. \tag{5.16}$$

where $\frac{\gamma}{2} = \pi \times 5.8\,\mathrm{MHz}$ is the maximum scattering rate. These parameters differ significantly from the ones used for the magneto-optical trap to load the reservoir [Ser07].
The main optimization goal to operate the MOT as a single-atom detector is to obtain a large signal-to-noise ratio which first requires to reduce stray light as well as possible. We achieve this by decreasing the beam diameter of the MOT beams to $d = 4\,\mathrm{mm}$ by means of motorized irises in the optical path as shown in figure 5.15. To minimize the size of the region on the CCD chip where stray light contributes to the background we apply a rather strong gradient of 250 Gauss/cm to compress the MOT.
Under these constraints we maximize the scattering rate to record as many photons as possible within the given exposure time. This requires a high scattering rate, which can be realized with a small detuning and a light intensity above saturation. However, the parameters have to be chosen such that no new limitations arise. If the detuning is chosen too small the operation of the MOT becomes unstable

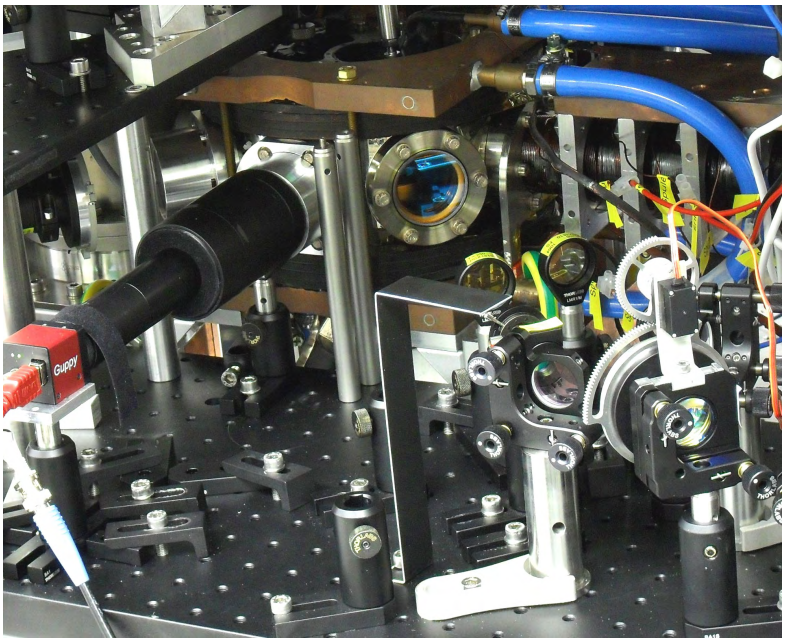

Figure 5.15: Setup for single atom fluorescence imaging. The fluorescence signal of the atoms in the MOT is recorded with a CCD camera from the left. Great care has to be taken to shield the CCD from stray light. For that reason motorized irises (right hand side) have been installed to minimize the diameter of the MOT beams.

because small shifts in the detuning lead to a blue detuning of the beams with respect to the atomic transition which immediately causes an atom loss. For a detuning of twice the natural line width the operation of the MOT remains stable. The light intensity is chosen such that the gain in scattering rate exceeds the additional amount of stray light.

To deduce the atom number from the fluorescence signal we bin the data into a histogram. Peaks in the histogram correspond to an integer number of atoms. We extract the calibration factor

$$\kappa = \text{fluorescence signal/atom} \tag{5.17}$$

from the distance between two peaks. As both intensity of the MOT beams and the detuning fluctuate on a timescale of minutes, the scattering rate and thus κ drifts on a few percent level. We compensate this drift by rescaling κ for each measurement with a scaling factor which is determined from $\bar{\kappa}(n)$, i.e. the mean of κ averaged over measurements $(n-10)$ to $(n+10)$. To calculate $\bar{\kappa}(n)$ we only consider measurements with fluorescence signals close to a peak in the histogram,

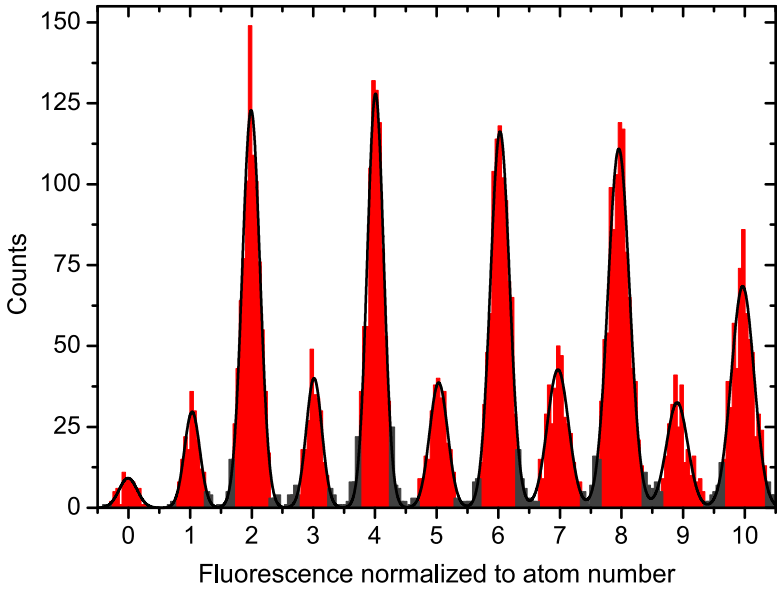

Figure 5.16: Histogram of the normalized fluorescence signal. The black curves are Gaussian fits to the data. The small overlap between the peaks demonstrates that the imaging setup is suited to determine the number of atoms in the prepared sample on a single atom level. The 2-atom (8-atom) peak is separated from its adjacent peaks by 7σ (5.7σ). From [Ser11].

i.e. within 1σ. The rescaled data is binned into a histogram and Gaussian are fitted to the peaks as shown in figure 5.16. The large separation of the peaks of about $6\,\sigma$ allows us to distinguish the prepared systems on a single atom level. The data points within $2\,\sigma$ of each peak are binned to an integer number yielding the number of atoms in the prepared system. The 5% of measurements outside the $2\,\sigma$ environment are rejected (black bars).
An important property of the single-atom detector is its capture efficiency of the samples released from the microtrap. Since we cannot directly measure this efficiency we deduce a lower bound of 98(1)% from the preparation fidelity of the samples (see chapter 6).

5.6 A high-resolution objective

To prepare quantum systems with a new level of flexibility a high-resolution objective has been designed during this thesis. This section motivates its design and discusses major design parameters. Unfortunately the objective could not be

tested within the duration of this thesis because the delivery of the glass blanks to the company which cuts, coats and assembles the lenses (Jenoptik) was delayed significantly.

5.6.1 Motivation and design goals

Increasing the preparation fidelity

For the preparation of few-particle systems in a deterministic way we need to control the lifetimes of bound states in the tilted potential as described in chapter 4.1.1. To find out to what extend this is feasible in the experiment, it is instructive to consider the simplest case: the preparation of a system consisting of two atoms in two spin states occupying the ground state of the potential. To prepare such a system deterministically, the occupation probability for the lowest energy state has to approach unity. Furthermore, the occupation probability for the second state has to vanish after the spilling process has been performed.
We calculate the mean occupation number from the tunneling time τ which we obtain from a WKB calculation according to equation 4.26 as

$$P(E_i) = e^{-t_{\mathrm{spill}}/\tau(E_i)},$$

where $i = 0, 1$ labels the energy state and $t_{\mathrm{spill}} = 25\,\mathrm{ms}$ denotes the duration of the spilling process. The magnitude of $\tau(E_i)$ depends on the height of the tunneling barrier which is controlled by the depth of the optical potential and the applied magnetic field gradient. To evaluate the accuracy which is required to control the depth of the optical potential the gradient is kept constant at $B' = 19$ Gauss/cm. The occupation probabilities for the two lowest energy states as a function of the depth of the optical potential are plotted in figure 5.17 for three different sizes of the optical trap. The regime where the first energy level is occupied with a probability $p_0 > 0.995$ and the second with $p_1 < 0.005$ is indicated as the gray shaded region. Within this window the fidelity of preparing a system with one atom is larger than $p > 0.995 \cdot (1 - 0.995) \approx 0.99$. Taking into account the second spin state, the fidelity to prepare two atoms in the ground state amounts to $P_{\mathrm{tot}} = 0.99 \cdot 0.99 \approx 0.98$. For smaller trap sizes the width of this window increases significantly as shown in figure 5.18. From the occupation probability one finds that the depth has to be controlled with an accuracy of only a few percent for trap sizes below one micrometer which can be easily achieved in the experiment. On the other hand, the required accuracy is on the order of 0.1 percent level for a trap with $w_0 = 2.8\,\mu$m as it was the case of the first implementation of the microtrap. This value is close to the accuracy achieved in the experiment and may explain the reduced fidelity obtained with the first micro-trap setup. For the current setup

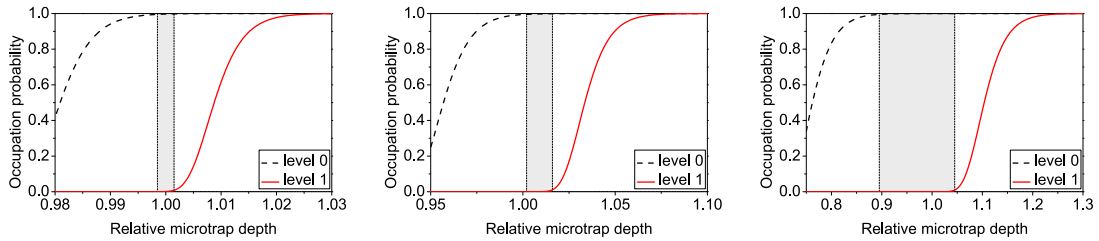

(a) $w_0 = 2.8\mu$m (b) $w_0 = 1.8\mu$m (c) $w_0 = 0.8\mu$m

Figure 5.17: Window of deterministic preparation. For a deterministic preparation of a two-atom system the occupation probability for the first energy level (black dashed line) has to approach 1 whereas the probability for the second level has to vanish (red solid curve) after the spilling process. The occupation probabilities have been calculated using WKB methods. The regime of trap depths where the first energy level is occupied with a probability $p_0 > 0.995$ and the second $p_1 < 0.005$ is indicated as the gray shaded regions. For smaller trap sizes the width of the window increases significantly. Note the different axes.

an accuracy of 0.6% is required. This level is about one order of magnitude lower compared to the accuracy reached in the experiment as shown in section 5.4.1. It is not clear that this limits the preparation fidelity in the experiment. However, if the window of high fidelity preparation is small the system becomes extremely sensitive to other sources of noise which are present in the experiment such as mechanical vibrations. With a trap size below 1μm the optical depth is definitely eliminated as a source of error.

Preparing systems in a variety of potential landscapes

The new objective will allow us to explore few-body systems in a variety of potential landscapes. A first starting point is the realization of a three-dimensional system with a small number of particles. In three dimensions there are degenerate energy levels which leads to the formation of a shell structure. This gives rise to magic numbers corresponding to systems with closed shells, as it is known from nuclei. Since we can tune interactions between the particles the system is uniquely suited to explore pairing effects as discussed in chapter 8.
To prepare a 3-D system, the level spacing in radial direction has to similar in axial direction which requires a trap with low aspect ratio $\eta = \omega_\perp/\omega_\parallel \to 1$. The aspect ratio of the trap formed by a focused Gaussian laser beam is given in the

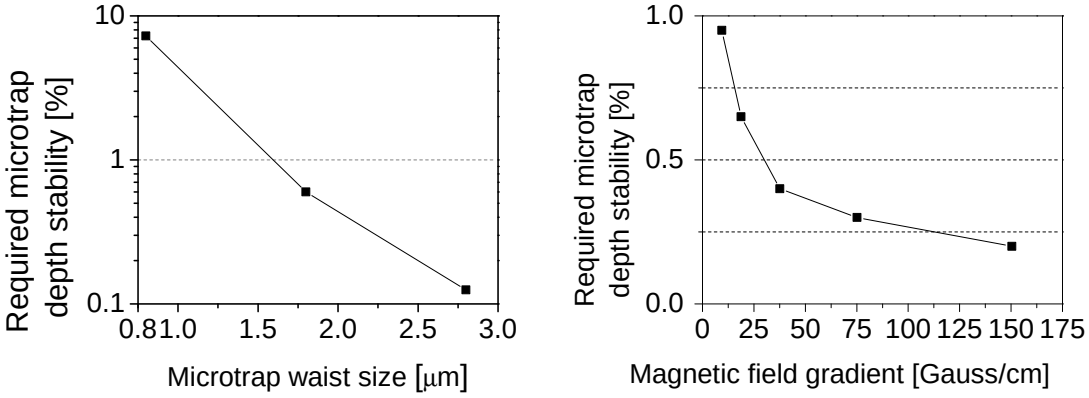

Figure 5.18: Required microtrap power stability versus microtrap size (a) and applied magnetic field gradient (b). The values are given for the preparation of samples consisting of two atoms with preparation fidelity exceeding 98%. For smaller trap sizes, the relative control over the trap depth becomes less critical at a given gradient. Comparing the new objective with the implemented one, the sensitivity will be lowered by a factor of ten. When the magnetic field gradient is lowered, the sensitivity of the preparation fidelity on the relative power stability is reduced. However, the overall trap frequency is also reduced which makes the system more sensitive to low frequency noise. For the calculation a gradient of 19 Gauss/cm was used in (a), a waist of $w_0 = 1.8\,\mu$m in (b).

harmonic approximation as [Gri00]

$$\eta = \frac{\omega_\perp}{\omega_\parallel} = \frac{\sqrt{\frac{4V_0}{mw_0^2}}}{\sqrt{\frac{2V_0}{mz_R^2}}} = \sqrt{2}\frac{z_R}{w_0} \propto w_0 \tag{5.18}$$

where w_0 is the waist, $z_R = \pi w_0^2/\lambda$ the Rayleigh length and V_0 the maximum potential depth. To realize a trap with an aspect ratio close to unity a small waist is required. For that reason, the ability to create a small focus is a major design goal of the objective. With an expected waist of $w_0 < 0.8\,\mu$m, an aspect ratio of $\eta \approx 3$ can be realized.
The objective will also enable us to realize multi-well configurations such as a double well or a periodic potential as discussed in chapter 3.2. Recently a first approach towards the preparation of a system with tunable properties in a multi-well potential has been demonstrated [Zim11].
By subsequently adding more potential wells to our system a controlled transition from the few-particle regime to the many-particle regime is feasible. This can be viewed as extending the artificial atom to a molecule and in the extreme limit to a solid state system as it will be discussed in chapter 8.

Probing the system

The momentum distribution of a macroscopic system can be accessed directly via time-of-flight absorption imaging techniques [Ket99]. However, this technique cannot be applied directly to a few-particle system due to the the vanishing absorption signal of the few atoms. One way to overcome this hurdle is to use fluorescence imaging as discussed in the previous section.
However, to access the momentum distribution the fluorescence signal has to be taken after time of flight, and furthermore the atoms have to be spatially resolved which is extremely challenging due to the low signal-to-noise ratio. There are two approaches to overcome this hurdle: First the signal-to-noise can be increased by averaging over many realizations. Using this technique a time-of-flight image of a single atom could be recorded recently [Fuh10]. The second approach is to recaptured the atoms after time-of-flight in a deep optical lattice to increase the observation time in order to detect their fluorescence signal [Bak09].
For both approaches a high opening-angle of the imaging system is required to collect as many photons as possible. Therefore the designed objective has a numerical aperture of NA= 0.6 which enables us to collect 10% of the emitted photons. To be able to create a deep lattice with the objective using near resonant light it is designed to allow a high-resolution also for $\lambda = 671\,$nm. The high imaging resolution can also be used to probe the quantum state of atoms in a periodic potential.

Provided a high signal-to-noise ratio, the resolution of the designed objective is sufficient to resolve single sites of an optical lattice with commonly used lattice spacing of $d = 532\,\mathrm{nm}$.

5.6.2 Design

Optimization procedure

A first step in optimizing an optical design is to define the figure of merit which has to be minimized. One possibility therefore is the root-mean-square (rms) radius at the image plane of a set of rays which are traced through the optical setup. However, in the limit of a perfect lens the rms radius vanishes, which is an unphysical result. Because of diffraction the intensity distribution and thus the point-spread-function (psf) is given as an Airy function as discussed in section 5.4.2. In this limit, the optical path difference (opd) between the real wavefront and a spherical reference wavefront created by a perfect lens can be used as a figure of merit. Aberrations introduced by a real lens cause an increase in opd which degrades the image. In general, the exact relationship between the opd and the image degradation is not trivial. For opd $\ll \lambda$ the main effect is that the maximum of the psf gets reduced to a ratio whose value is defined as Strehl ratio S. It has been shown by Rayleigh, that a peak-to-valley opd of $\lambda/4$ leads to a Strehl ratio of $S = 0.8$, without decreasing the resolution which is given by the minima of the Airy function. Since the corresponding image cannot be distinguished from a perfect image such an imaging system is called 'diffraction limited'. Although this criterion is widely used one has to consider that it is only valid for an opd which is caused by first order spherical aberrations. As a figure of merit which accounts for a variety of aberrations the rms value of the opd can be used to determine the Strehl ratio on a few percent level according to [Mah82]

$$S = e^{(-2\pi W_{\mathrm{rms}})^2} \tag{5.19}$$

where W_{rms} is the rms wavefront error in units of λ. The diffraction limit, a Strehl ratio of S= 0.8, corresponds to $\mathrm{opd}_{\mathrm{rms}} = 0.07\lambda$. Following these considerations W_{rms} was chosen as a figure of merit to optimize the performance of the objective. The second step to design the objective was to find an initial design as starting point. Two main considerations helped to find this design. Since the objective should perform up to a high numerical aperture, spherical aberrations had to be kept to a minimum. Therefore a biconvex lens with two aspheric surfaces was chosen as first element. Furthermore, the system needs to be achromatic for two wavelengths. The chromatic focal shift due to dispersion between the two

wavelengths $\lambda_1 < \lambda_3$ of a thin spherical lens is given as

$$\Delta f \approx \frac{f}{\nu} \tag{5.20}$$

where f is the focal length and ν is the Abbe number of the glass. This is defined as

$$\nu = \frac{n_2}{n_1 - n_3}. \tag{5.21}$$

where n_i denotes the refractive index at λ_i with $\lambda_1 < \lambda_2 < \lambda_3$.
Commonly, the Abbe number is given for the visible regime where $\lambda_{1,2,3}$ corresponds to blue, green and red light. For a system with two lenses with focal lengths $f_\mathrm{a} > 0$ and f_b the chromatic shift can be compensated if [Wit05]

$$\begin{aligned} \Delta\left(\frac{1}{f_\mathrm{a}}\right) + \Delta\left(\frac{1}{f_\mathrm{b}}\right) &= 0 \\ \Leftrightarrow \frac{1}{\nu_\mathrm{a} f_\mathrm{a}} &= -\frac{1}{\nu_\mathrm{b} f_\mathrm{b}} \\ \Leftrightarrow \frac{f_\mathrm{a}}{f_\mathrm{b}} &= -\frac{\nu_\mathrm{b}}{\nu_\mathrm{a}} \end{aligned} \tag{5.22}$$

Since ν is positive, f_b has to be negative. To obtain a positive focal length for the total system it follows that $f_\mathrm{a} < |f_\mathrm{b}|$ which requires $\nu_\mathrm{b} < \nu_\mathrm{a}$. To minimize aberrations the numerical aperture of the diverging lens has to be kept as small as possible. Therefore $|f_\mathrm{b}|$ has to be as large as possible which requires a large ratio of Abbe numbers between the focusing and the diverging lens according to equation 5.22.
To correct the system for two wavelengths in the NIR regime λ_1, λ_3 with $\lambda_1 = 671\,\mathrm{nm}$, $\lambda_3 = 1064\,\mathrm{nm}$ and $\lambda_2 = (\lambda_3 + \lambda_1)/2 = 868\,\mathrm{nm}$, the corresponding Abbe numbers for the glasses in the catalog were calculated according to equation 5.21 and two glasses (N-SF66, $\nu = 31$, N-PK51, $\nu = 92$) with a high ratio in Abbe number where chosen for an achromat. Because of the positive focal length of the aspheric lens a glass with high Abbe number (N-FK5, $\nu = 75$) had to be selected under the constraint to be hard enough for machining which requires a Knoop hardness $K > 400$.

The initial design consists of a biconvex lens with two aspheric surfaces and one achromat for the NIR regime. A sketch of this setup is shown in figure 5.19. With only two elements it provides a diffraction-limited performance for both wavelengths at a NA= 0.5 with a field of view of $200\,\mu\mathrm{m}$ diameter. To increase the numerical aperture further to NA=0.6, an additional element was added to the design. This also serves the purpose to decrease the required size of the incoming

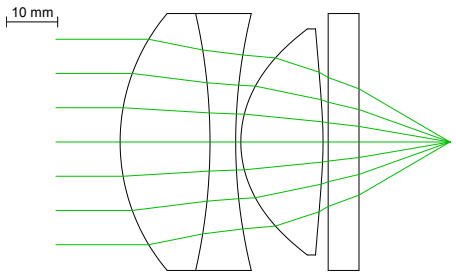

Figure 5.19: Starting point for the final design of the objective. The initial design consists of two elements, one achromat which corrects the chromatic shift for the two wavelengths $\lambda_1 = 671\,\text{nm}$ and $\lambda_2 = 1064\,\text{nm}$, and one double-sided aspheric lens to minimize spherical aberrations. It provides a diffraction-limited performance for a NA~ 0.5 with a field of view with a diameter of 200μm.

beam. As a consequence optics with 1 inch diameter can be used in the further optical setup. Since this element had to be also achromatic a doublet of (N-BK7,N-SF11) was used.

Nominal design

wavelength	1064 nm	671 nm
focal length	20.3 mm	
image distance	∞	
diameter field of view	200 μm	
max. diffraction limited NA	0.6	
entrance aperture diameter at max NA	24.4 mm	
resolution	1.08 μm	0.68 μm
waist of focus	0.72 μm	0.45 μm

Table 5.4: Design parameters of the high-resolution objective.

Figure 5.20 presents a sketch of the final design consisting of the small achromat, the large achromat and the double sided aspheric lens. To evaluate how well the chromatic focal shift is compensated figure 5.21 presents the chromatic focal shift as a function of the wavelength in the paraxial approximation. The use of glasses with adequate Abbe numbers leads to two zero-crossings of the focal shift approximately at the design wavelengths $\lambda_1 = 671\,\text{nm}$ and $\lambda_2 = 1064\,\text{nm}$. The expected focal shift for an on-axis point for the two wavelength without the

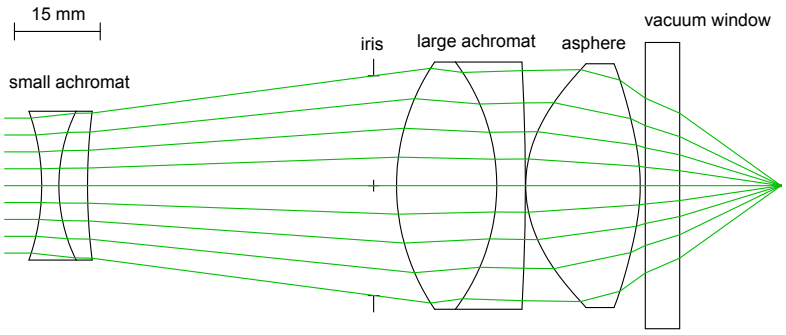

Figure 5.20: Scheme of the high-resolution objective. With the objective it should be possible to improve the preparation fidelity of the few-particle systems by creating a microtrap with smaller volume. Furthermore the creation of arbitrary potentials becomes possible. The objective has been designed to focus the trapping beam ($\lambda_2 = 1064\,\mathrm{nm}$) to a waist of $w_0 = 780\,\mathrm{nm}$. The large opening angle is extremely useful for position-resolved imaging of single atoms. Since 10% of the emitted photons can be collected which should provide enough signal- to-noise to image few-particle samples on a single-atom level after time-of-flight. The expected spatial resolution is $r = 700\,\mathrm{nm}$ for $\lambda_1 = 671\,\mathrm{nm}$ which should give allow to detect ordering phenomena of correlated many-body systems in periodic potentials.

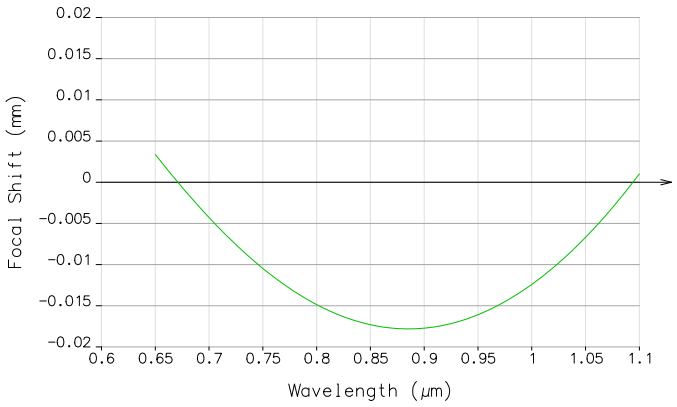

Figure 5.21: Chromatic focus shift in the par-axial approximation. The large achromatic doublet consisting of glasses with adequate Abbe numbers leads to two zero crossings of the focal shift approximately at the design wavelengths $\lambda_1 = 671\,\mathrm{nm}$ and $\lambda_2 = 1064\,\mathrm{nm}$. The expected focal shift for an on-axis point for the two wavelength is $\Delta f < 1\mu\mathrm{m}$.

paraxial approximation is $\Delta f < 1\mu$m. For 671 nm$< \lambda <$ 1064 nm, the focal shift increases up to 18μm.

Figure 5.22 evaluates the performance as a function of the field of view. The field

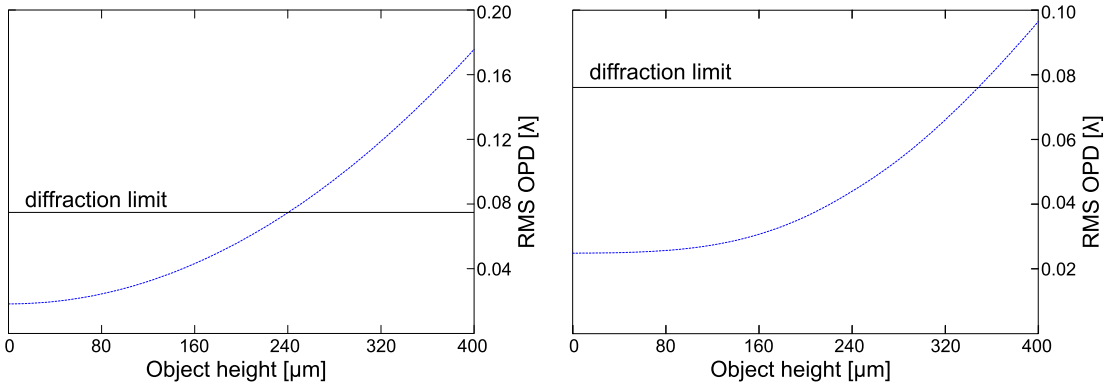

(a) $\lambda_1 = 671$ nm (b) $\lambda_2 = 1064$ nm

Figure 5.22: Root-mean-square (rms) of the optical path difference as a function of object height. The nominal design works diffraction limited for a field of view with a diameter up to $d_1 = 2{\cdot}240\mu$m for $\lambda_1 = 671$ nm and $d_2 = 2 \cdot 350\mu$m for $\lambda_2 = 1064$ nm. Manufacturing tolerances decrease the expected field of view down to $d \approx 200\mu$m.

of view for the nominal design is as large as $d_{671} \approx 480\,\mu$m and $d_{1064} \approx 700\,\mu$m. Design goal was a field of view of $d = 200\,\mu$m which is a more realistic value when manufacturing tolerances are taken into account. To evaluate the focusing and imaging capability of the objective its simulated point spread function for an on-axis point is plotted in figure 5.23. The point spread function for $\lambda_1 = 671$ nm yields a resolution of $r < 0.7\,\mu$m whereas the size of the focus has a waist of $w_0 < 0.8\,\mu$m for $\lambda_2 = 1064$ nm. The parameters of the nominal design are summarized in table 5.4.

Tolerancing

The performance of a real system is worse compared to the nominal design because manufacturing tolerances introduce aberrations which degrade the performance of the system. Therefore, the nominal design has to be significantly better than the diffraction limit corresponding to $S = 0.8$ Strehl ratio in order to have a sufficiently large budget accounting for errors. Our nominal design has a $W_{\mathrm{rms}} = 0.026\lambda$ which is a factor of 2.8 lower than the value for the diffraction limit $W_{\mathrm{rms}} = 0.074\lambda$. This corresponds to a Strehl ratio of $S = 0.97$. The available error budget amounts to

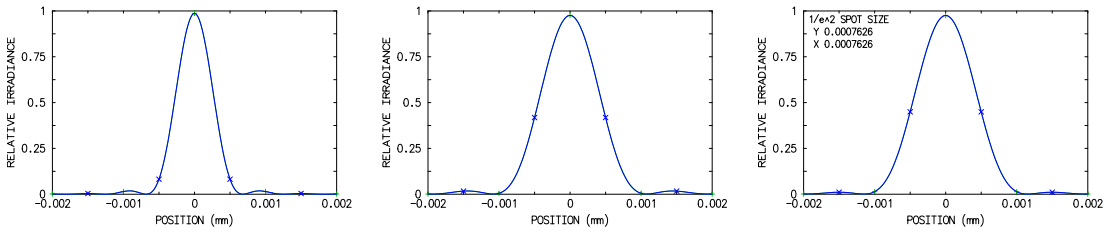

(a) Point spread function for $\lambda_1 = 671\,\text{nm}$ yielding a resolution of $0.68\mu\text{m}$.

(b) Point spread function for $\lambda_2 = 1064\,\text{nm}$ yielding a resolution of $1.08\mu\text{m}$.

(c) Intensity distribution of the focus for an illumination of the entrance pupil with truncation ratio of 1.5. The waist is smaller than $w_0 < 0.8\mu\text{m}$.

Figure 5.23: Imaging and focusing performance of the objective.

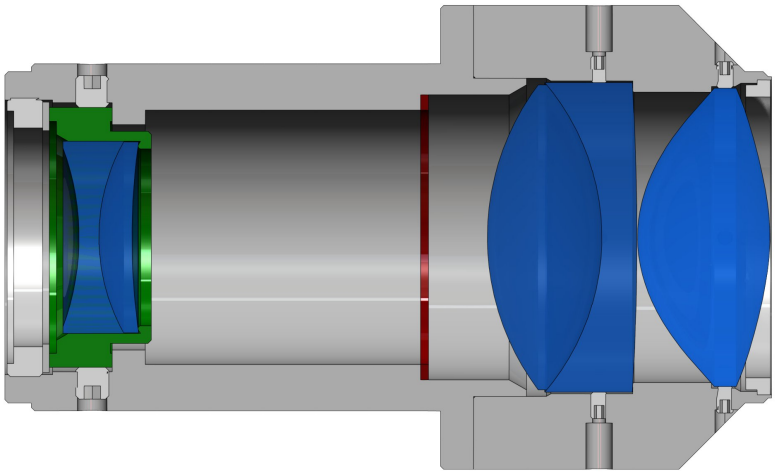

Figure 5.24: Mount for the lenses of the high-resolution objective. The critical alignment of the aspheric lens with respect to the large achromat defines the optical axis of the system. After their alignment the lenses are glued into the mount. To compensate for manufacturing tolerances the small achromat can be translated perpendicular to the optical axes. The iris (red) defines the numerical aperture of the objective to NA = 0.6.

$(0.074 - 0.026)\lambda = 0.048\lambda$.
An overview over the most critical elements can be obtained by evaluating the tolerances which cause an increase of $\Delta W_{\text{rms}} = 0.01\lambda$. Most tolerances can be fulfilled with little effort, such as air spaces, radius tolerances and surface irreg-

Power fringes	1
Irregularity fringes	1
Air spaces [mm]	0.1
Lens thickness [mm]	0.05
Refractive index	$\pm 2 \times 10^{-4}$
Refractive index homogeneity	$\pm 1 \times 10^{-6}$

Table 5.5: Tolerances which are fulfilled with little to moderate effort. For detail see [Fis08].

ularities.These are assigned to the lens as shown in table 5.5. A more detailed description of tolerances in general can be found in [Fis08]. Tolerances which are more difficult to fulfill are assigned to the lens according to the capabilities of the manufacturing company. The system's tolerances can be significantly relaxed by introducing compensator variables. In our design we allow for a focus shift and the small achromat can be decentered perpendicular to the optical axis as shown in figure 5.24. After assigning critical tolerances to the lens their influence on the system's performance is evaluated. Tolerances leading to an increase in in rms opd which exceeds 0.02λ are presented for different values of the numerical aperture in table 5.6. The most critical items is the wedge of the vacuum view port of $1.5'$ which we measured using an interferometric technique. It is followed by the thickness tolerance of the view port which is specified to 0.1mm, the thickness of the aspheric lens and the tilt of its surface with respect to the optical axis. For a decreasing numerical aperture the system becomes more insensitive. The worst case scenario corresponds to a rms opd which is in 95.4% of possible realizations less or equal to the value given in table 5.6. In the worst case, the system is diffraction limited for a numerical aperture between 0.4 and 0.5. We expect the view port not to be the limiting performance factor of the objective in future experiments since the quality of the vacuum view port of the new experimental apparatus which is currently set up is significantly better than the one used in the old experiment.
A complementary error analysis was carried out using the technique of Monte Carlo simulation. The performance of 100 realizations of the objective differing within the range of their manufacturing tolerances was simulated. The results are shown in figure 5.25. For a numerical aperture up to 0.5 there is significant probability that the objective works diffraction limited.
As a summary, the performed error analysis is suitable to give a worst case scenario for the performance of the objective based on statistics. In the worst case we obtain a objective with diffraction-limited performance at a numerical aperture of $0.4 - 0.5$. Considering only the focusing performance for $\lambda_2 = 1064\,\mathrm{nm}$ light, the

NA	Item	Tolerance	Change in rms opd [λ]
0.6	Surface tilt view-port [']	1.5	0.078
	Thickness view-port [mm]	0.1	0.067
	Thickness aspheric lens [mm]	0.025	0.055
	Surface tilt aspheric lens [']	0.5	0.035
	Thickness large achromat [mm]	0.05	0.032
	Tilt large achromat [']	0.5	0.023
	worst case rms opd		**0.172**
0.5	Surface tilt view-port [']	1.5	0.046
	Surface tilt aspheric lens [']	0.5	0.023
	Thickness view-port [mm]	0.05	0.022
	worst case rms opd		**0.100**
0.4	Surface tilt view-port [']	1.5	0.023
	worst case rms opd		**0.057**

Table 5.6: Tolerances which increase the rms opd by more than 0.02λ. Most critical elements are the vacuum view port and the aspheric lens. For lower numerical aperture the system becomes less sensitive. In the worst case the system is diffraction limited with NA= 0.4-0.5.

worst case scenario yields numerical aperture of 0.55. This results in a waist of $w_0 = 830\,\mathrm{nm}$ which is 10% lower than the design goal.

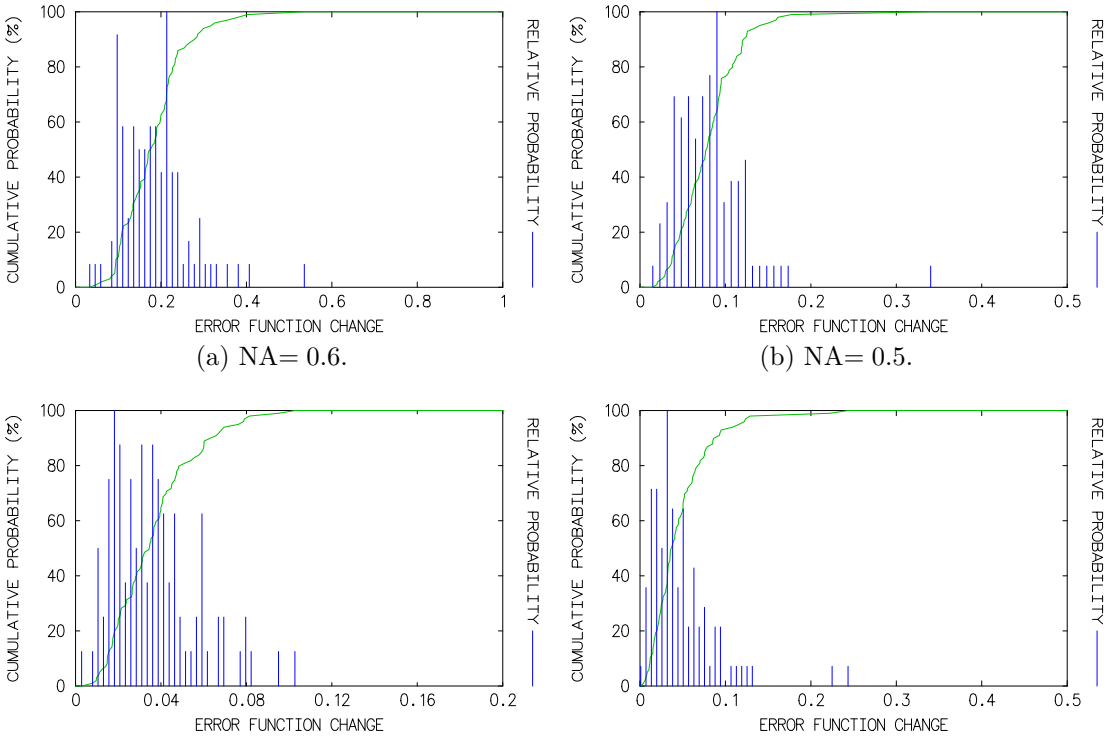

(a) NA= 0.6. (b) NA= 0.5.

(c) NA= 0.4. (d) NA= 0.55, $\lambda = 1064\,\mathrm{nm}$ only.

Figure 5.25: Monte Carlo simulation of the increase in rms opd due to tolerances. The system is diffraction limited when the change in error function is smaller than 0.045. For a decreasing numerical aperture the success probability to obtain a diffraction limited objective increases. Calculations are performed for 100 realizations of the objective.

6 Deterministic preparation of a tunable few-fermion system

We started setting up an apparatus to prepare a tunable few-fermion system at the end of 2006. The idea was to start from a reservoir of cold atoms and spill all but a few atoms which compose the final quantum system. Since the preparation of the reservoir relies on established techniques, a first implementation could be realized already at the beginning of 2009. The reservoir was the starting point for experiments with three-component Fermi gases [Ott08, Lom10a]. In particular, we successfully associated a universal three-body state, an Efimov trimer, and measured its binding energy as a function of the interaction strength [Lom10b].
After this 'distraction' we focused again on the realization of a few-fermion system. The main experimental challenges we had to overcome was the implementation of a single atom detection scheme and the realization of a small microtrap. To be able to count few atoms, the idea was to use a magneto optical trap to record the fluorescence signal of the atoms. A proof of principle experiment was successful in mid of 2009 when we found parameters for the magneto-optical trap that counting of single atoms became possible. Around the same time the first generation of the microtrap was implemented and tested [Zür09]. After we optimized the detection fidelity mainly by reducing stray-light we could make first attempts to spill the microtrap to contain only a few atoms in April 2010. We successfully prepared systems consisting of only one to ten atoms. However, the fluctuations in atom number were so high that only a preparation fidelity of less than 40% could be realized, which is far from being deterministic. Possible limitations for the preparation fidelity were the size of the microtrap, its intensity stability and its mechanical stability. As the size of the microtap cannot be reduced by simple means as discussed in chapter 5 we decided to first improve on the intensity stability as discussed in the previous chapter. The main limiting factor was the intensity fluctuations caused by interference fringes on the cover glass of the photo diode whose output signal was used to stabilize the light power of the microtrap. In addition the setup was sensitive to polarization drifts which we eliminated using a polarizing element after the fiber. With these methods we could achieve a relative intensity stabilization of $0.5 \cdot 10^{-4}$. However, this did not increase the preparation fidelity beyond 60%. This lead us to install the second generation microtrap in

Juli 2010 which allowed us to reduce the microtrap size significantly. A smaller microtap size makes the setup less sensitive to intensity fluctuations as discussed in the previous chapter. This turned out to be the right step because all data for the publication [Ser11] could be taken in August 2010.
Before the main experimental results are presented the chapter starts with a description of the experimental sequence and how initial parameters for the transfer of atoms into the microtrap were found. Then, main results are shown and compared with theoretical expectations. This is followed by a description of the technique we use to probe whether the systems are prepared in their ground state. The chapter finishes with a description of the preparation of imbalanced systems and a state sensitive detection technique.

6.1 Loading the microtrap

To prepare few-particle samples in a deterministic way, the occupation probability for the lowest states of the potential is required to approach unity as discussed in section 4.1.1. Since the occupation probability for an energy state is determined by the Fermi-Dirac distribution, it increases the lower the state's energy is compared to the Fermi energy. This allows us to enhance the occupation probability of the lowest states by increasing the Fermi energy of the system. Therefore, we start with a reservoir of cold atoms and enhance its Fermi energy by superimposing a deep microtrap with the reservoir as discussed in chapter 4.1.1. The maximum enhancement is achieved only if the width of Fermi edge, which is determined by the temperature, is not increased during the transfer of atoms from the reservoir into the microtrap (see figure 4.2). Therefore, atoms in the microtrap and in the reservoir have to be in thermal equilibrium during the transfer which requires a high elastic collision rate. This is obtained for a large value of the scattering length $|a|$ between atoms in states $|1\rangle$ and $|2\rangle$ which can be realized by applying a magnetic field which is close to the Feshbach resonance. However this has some drawbacks since we need to ramp the magnetic field to the zero-crossing of the scattering length ($B = 527$ Gauss, see figure 6.1) in order to prepare non-interacting samples: For positive scattering length there is a molecular bound state which is populated by three-body recombination of three particles into a dimer and a free atom. The formation of molecules can be avoided by transferring the atoms into the microtrap with the scattering length tuned to a negative value where no bound state exists. We obtain a maximum value for $|a|$ by applying a magnetic field of 300 Gauss as indicated in figure 6.1. In this way the magnetic field can be ramped to the zero crossing of the scattering length without populating the molecular branch after the transfer has been completed.

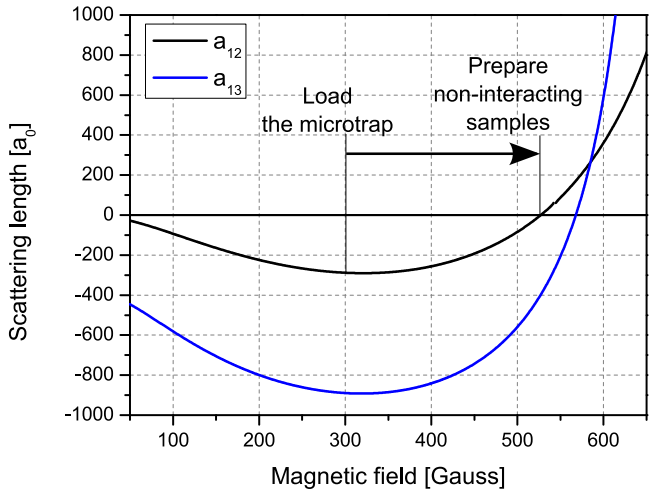

Figure 6.1: Scattering length for the $|1\rangle$-$|2\rangle$ and $|1\rangle$-$|3\rangle$ spin mixture. For an efficient transfer high elastic collision rates are required. Therefore the magnetic field is tuned to 300 Gauss during the transfer of a $|1\rangle$-$|2\rangle$ mixture. After the transfer, the magnetic field is ramped to $B \approx 527$ Gauss in order to prepare a non-interacting few-particle system (black arrow).

If atoms in the microtrap and the reservoir are in thermal equilibrium, the microtrap is completely filled. In that sense, the filling of the microtrap can be used as an indicator for thermalization.

To determine the maximum number of atoms which fit into the microtrap we prepare a strongly interacting sample by using a mixture of atoms in state $|1\rangle$ and $|3\rangle$ (figure 6.1) because negative scattering lengths up to $a_{13} = -894\,a_0$ can be realized. Optimum transfer parameters are found by recording the number of transferred atoms as a function of the interaction strength, the temperature of the reservoir and the time to load the microtrap t_{load}. We control the temperature of the reservoir by adjusting the final depth of the optical dipole trap at the end of the evaporation process. This depth is controlled using an acousto-optical modulator (aom) as described in chapter 5.3. No difference in the filling of the microtrap is found for $20\,\mathrm{ms} < t_{\mathrm{load}} < 500\,\mathrm{ms}$ which suggests that the timescale for thermalization is below 20 ms. The atom number in the microtrap for $t_{\mathrm{load}} = 20\,\mathrm{ms}$ is shown in figure 6.2. For a magnetic field below 520 Gauss, corresponding to a scattering length of $a = -440\,a_0$ and control voltage of the reservoir aom $V_{\mathrm{aom}} \leq 0.2\,\mathrm{V}$, the microtrap is completely filled. Setting a value of $V_{\mathrm{aom}} = 0.2\,\mathrm{V}$ yields a reservoir which consists of $2 \cdot 10^4$ atoms per state at a temperature of $T \leq 250\,\mathrm{nK}$ which corresponds to $T/T_F = 0.5$. To summarize, rates for thermalization seem to be

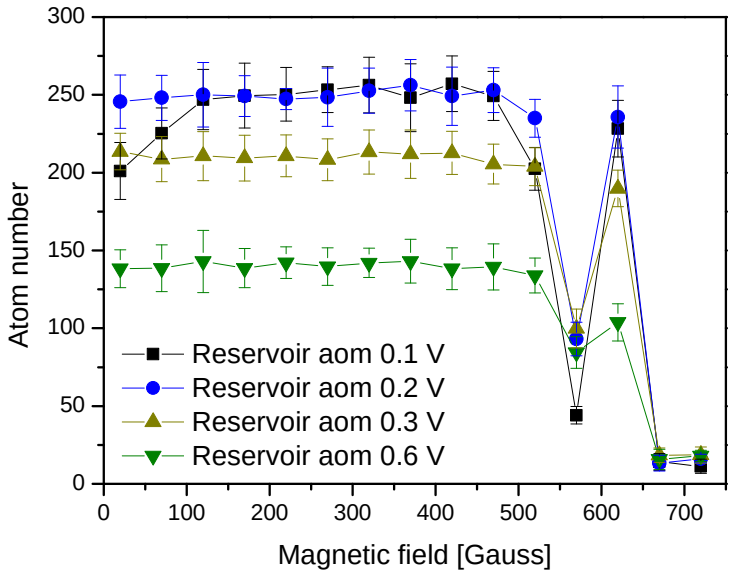

Figure 6.2: Transfer efficiency from the reservoir into the microtrap. An unfilled microtrap indicates that the system has not thermalized yet which hinders the deterministic preparation of the few-fermion system. To determine the maximum filling, a mixture of atoms in state $|1\rangle$ and $|3\rangle$ is prepared and the number of atoms in the microtrap is recorded for different temperatures of the reservoir which is determined by the control voltage of the reservoir aom. Below 568 Gauss, i.e. the field where the scattering length crosses zero, the sample is attractively interacting leading to a maximum filling of the microtrap of $\sim$ 250 atoms. At the zero-crossing of the scattering length, the microtrap does not get populated since the sample does not interact. For a magnetic field above 600 Gauss atoms are lost due to molecule formation and subsequent inelastic collisions.

faster than 20 ms at a scattering length of $a = -440\,a_0$. As the interactions can be made comparable strong for a $|1\rangle$-$|2\rangle$ mixture by applying a field of $B = 300$ Gauss, we are also able to fill the microtrap using this mixture which is more convenient to work with.

Having optimum transfer parameters found, the experimental sequence to prepare

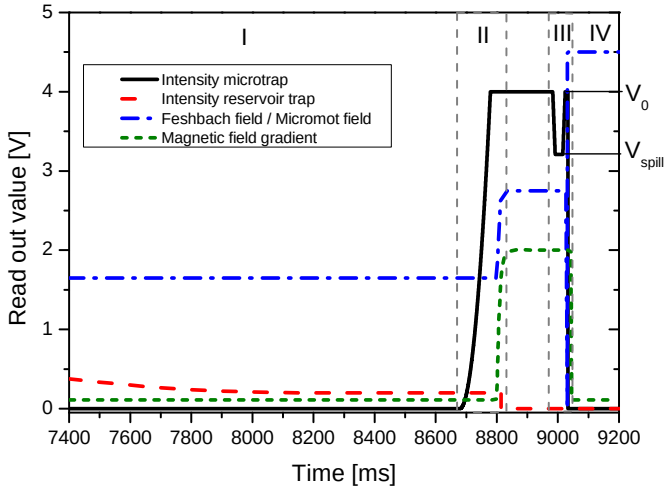

Figure 6.3: Experimental sequence to prepare few-fermion systems. In the first part (I) a reservoir of cold atoms is prepared. This is done by evaporative cooling, i.e. by decreasing the depth of the reservoir trap with an aom. The atoms are transferred into the microtrap (II) by ramping up the microtrap intensity within 100 ms. Then the reservoir is removed by switching off the reservoir dipole trap. The transfer ends by adjusting the Feshbach field such that the system becomes non-interacting. The spilling scheme (III) is applied by reducing the depth of the microtrap potential linearly to a value V_{spill} for a duration of $t_{\mathrm{spill}} = 25$ms during which the magnetic field gradient is applied. Then, the potential of the microtrap is restored to its maximum value to suppress further tunneling of atoms. This ends the spilling process. To detect the prepared sample, the atoms are transferred into the magneto-optical trap where their fluorescence signal is collected for 500 ms (IV). The quadrupole field required to operate the magneto-optical trap is created by the same coils used for tuning the interactions.

non-interacting few-fermion systems consists of four parts as indicated in figure 6.3. In the first step (I) the reservoir of cold atoms is prepared. For this, the atomic cloud is evaporatively cooled by decreasing the intensity of the reservoir

trap which is controlled by an aom (red line). This is followed by the second part of the sequence (II), the transfer of atoms into the microtrap. As both the preparation of the reservoir and the transfer into the microtrap require high collision rates, the Feshbach field is set to 300 Gauss during that time to maximize interactions (blue line). The transfer ends by turning off the interactions, i.e. setting the Feshbach field to $B_0 = 523$ Gauss where the scattering length approaches zero, and switching off the reservoir. The spilling scheme is performed in the third part of the sequence (III). As soon as the spilling gradient has stabilized to its final value the depth of the optical potential is reduced linearly, kept at the desired value for 25 ms to spill atoms and restored to its original value to suppress further tunneling. In the last part (IV) the prepared sample is detected by transferring it into the magneto optical trap and recording the fluorescence signal for 0.5 s.

6.2 Preparing non-interacting samples

To control the number of particles in the system we choose a ratio

$$s = \frac{V_{\text{spill}}}{V_0} \tag{6.1}$$

during the spilling process as indicated in figure 6.3. To determine the preparation fidelity the experimental cycle is repeated 200 times with the same value for s. Figure 6.4 presents the fluorescence signal of the prepared systems which has been normalized to the number of atoms in the trap. Every 200 runs the value of s and therefore the depth of the microtrap during the spilling process is varied by the same amount. For certain values for s we prepare systems consisting of an even number of atoms with high probability. In between these stable regions determined by low atom number fluctuations, there are regions with high fluctuations. The corresponding mean becomes odd.

For a systematic preparation of the few-particle systems more data has been taken in the range $0.645 < s < 0.9$. The mean atom number is calculated and plotted against s. The resulting graph is shown in figure 6.5. Each data point is the average of about 190 measurements.

It presents the main finding of this thesis: We can select the number of particles in the final system ranging from 1 to 10 by choosing an appropriate value for s. Plateaus for a range of values of s exist where systems with an even atom number are prepared. Between these plateaus there is a smaller regime where the prepared systems consist of an odd number of atoms.

This behavior can be understood quantitatively by calculating the occupation probability of the energy levels after the spilling process using the WKB technique

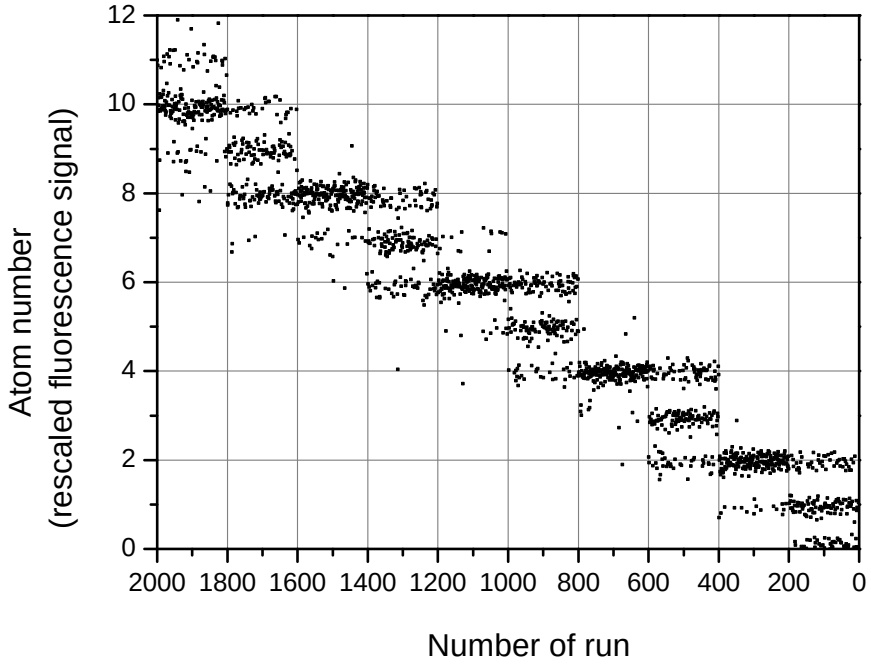

Figure 6.4: Normalized fluorescence signal. Every 200 runs the depth of the microtrap potential is reduced in equidistant steps. This allows us to control the number of atoms in the final system. For trap depths corresponding to an even atom number fluctuations are almost completely suppressed whereas for an odd atom number they are significant.

as described in chapter 4.2. The occupation probability of the ith energy level is determined by the tunneling time constant $\tau(E_i)$ of the atoms through the barrier in the tilted potential according to equation 4.26 as

$$P(E_i) = e^{-t_{\mathrm{spill}}/\tau(E_i)}.$$

This allows to calculate the mean atom number according to

$$n = 2 \cdot \sum_{i=1}^{N} P(E_i)$$

where N is the number of bound states. The factor of 2 accounts for the fact that each energy state is occupied by 2 atoms, one per spin state.
The red line in figure 6.5 presents the result of the calculation. The quantitative agreement of the theoretical curve with the data proofs that we control the number of particles by controlling the number of bound states in the tilted potential on

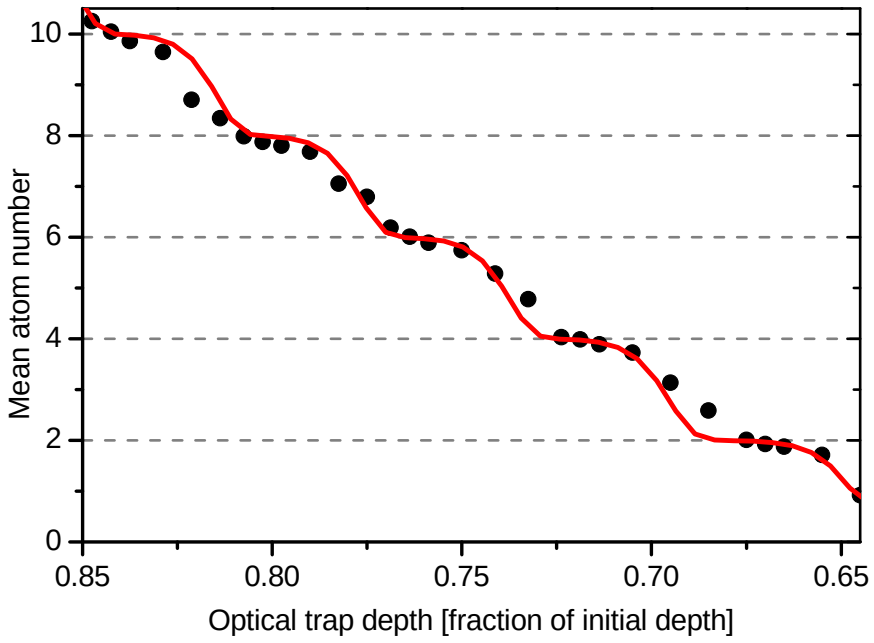

Figure 6.5: Control over the particle number. We choose the number of particles in the system by controlling the depth of the microtrap potential s while the magnetic field gradient is applied. The red line represents a WKB calculation with the parameters for the potential used in the experiment. The atom number of the final system is determined by tunneling of atoms through the barrier during the spilling process. Each data point is the average of ~ 190 measurements.

a single state level. As tunneling for atoms occupying lower states is completely suppressed, the mean atom number in the trap directly depends on the occupation probability for the highest bound state. A plateau in the mean atom number corresponds to a negligible occupation probability of the highest bound state and the second highest bound state is occupied with high probability. The width of the plateau is determined by the derivative of the occupation probability $\partial_s P(s)$. When the potential depth is tuned right between two plateaus the occupation probability for the highest state approaches 0.5 resulting in a mean occupation number of $2 \cdot 0.5 = 1$. At this value of s the derivative $\partial_s P(s)$ has a maximum, therefore the atom number becomes extremely sensitive to the magnitude of s which is subject to fluctuations in the experiment. Therefore, one expects large fluctuations in the atom number.
To perform an accurate calculation the potential has to be known precisely. We

characterize the potential by controlling the motional quantum state of a single atom as discussed in chapter 7.3 which leads to the parameters which enter the calculation: a gradient of $B'_{\mathrm{theo}} = 18.92\,\mathrm{Gauss/cm}$, a light power of $I_{\mathrm{theo}} = 291.5\,\mu\mathrm{W}$ for the microtrap and a waist of $w_0 = 1.838\mu\mathrm{m}$. These values agree within the errors with the parameters used in the experiment $B'_{\mathrm{exp}} = (18.9 \pm 0.2)\,\mathrm{Gauss/cm}$ and $I_{\mathrm{exp}} = (265 \pm 26.5)\,\mu\mathrm{W}$. Since the values of s which correspond to plateaus in the mean atom number drifted about 2% over the time of some months and the potential has been characterized with the new parameters, s was rescaled in the calculation by $2.637/2.685 = 0.98$ to compensate for the drift.
The measured fluctuations in the atom number are presented in figure 6.6. For

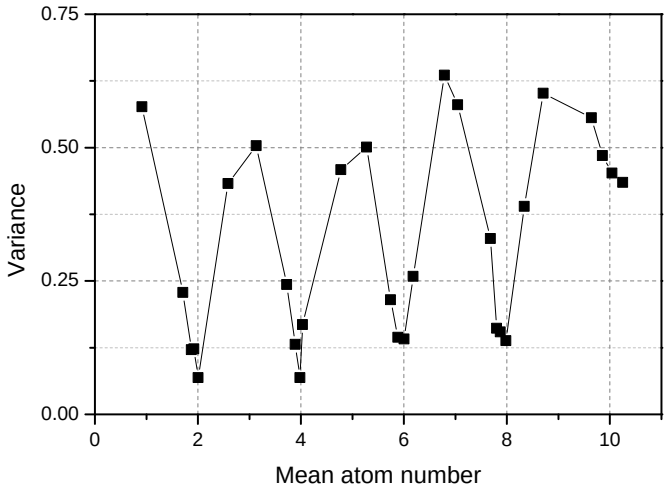

Figure 6.6: Atom number fluctuations. For an even atom number, the fluctuations are strongly suppressed. For eight atoms, the variance reaches a low value of var= 0.017. This corresponds to a suppression of 18 dB of $\mathrm{var}/\langle N\rangle$ compared to a system obeying Poissonian statistics.

systems with up to 10 atoms and an even atom number the fluctuations are significantly reduced. For eight atoms, we achieve

$$\frac{\mathrm{var}}{\langle N\rangle} = \frac{\sigma^2}{\langle N\rangle} = 0.017 \tag{6.2}$$

which corresponds to a suppression of 18 dB compared to a system obeying Poissonian statistics. With fluctuations reduced that far we prepare systems consisting of an even number of atoms ranging from 2 to 10 with a fidelity exceeding 90%. Figure 6.7 (a) and (c) present the corresponding histograms for the preparation of systems with two and eight atoms. The fidelity to prepare a two (eight)-atom

system amount to 96(1)% (92(2)%). The error represents the statistical error. With this fidelity a deterministic preparation of a few-fermion system has been realized.

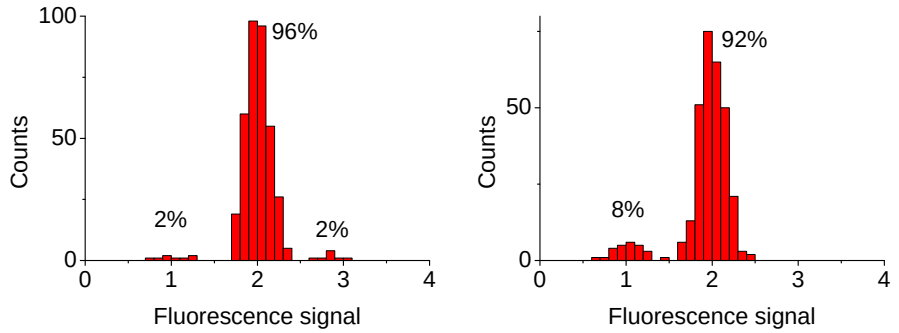

(a) Two-particle system, spilling once. (b) Two-particle system, spilling twice.

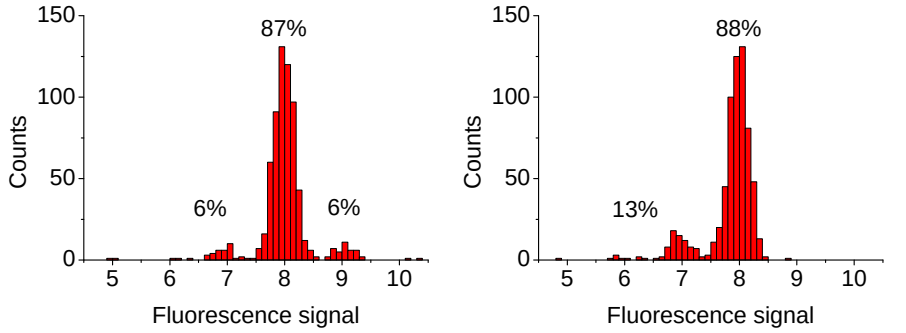

(c) Eight-particle system, spilling once. (d) Eight-particle system, spilling twice.

Figure 6.7: Histogram for the preparation of systems consisting of two and eight particles. (a,c) The systems are prepared by performing the spilling process once. (b,d) The histograms after a second spilling process reveal the degree of excitations as sketched in figure 6.8. From [Ser11].

6.3 Are they in the ground state?

To gain an estimate of the fraction of systems which are not in the ground state of the potential it is instructive to consider the two-atom case. The simplest excitation is given when only one atom occupies the ground state of the potential (probability P_1) and the second atom occupies the first excited energy level (probability P_2). Since the atoms do not interact the probability for this excitation amounts to

$$P_{\text{ex}} = P_1 \cdot P_2. \tag{6.3}$$

An upper bound $P_1 \leq 0.02$ can be deduced from the histogram given in figure 6.7 (b) as the probability to prepare a system with only one atom, i.e. one atom is missing on the lowest level. The probability to prepare systems with three atoms, i.e. one atom on the first excited state, leads to an upper bound $P_2 \leq 0.02$ yielding a total probability of $P = (0.02)^2 = 4 \cdot 10^{-4}$. Therefore only a negligible fraction of two-atom systems is not in the ground state after the potential has been tilted. However, the system can still be excited during the ramp which restores the poten-

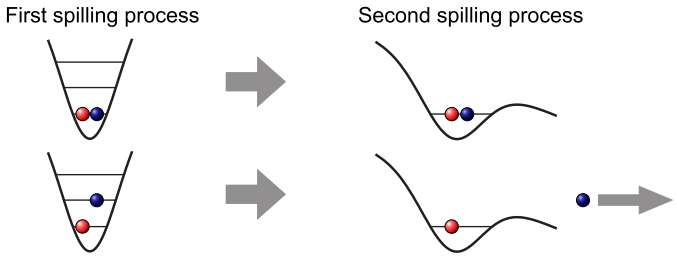

Figure 6.8: To determine whether the prepared few-particle systems are in their ground state, the spilling process is performed twice. This removes atoms which occupy exited single-particle states after the first spilling process. From [Ser11].

tial to complete the spilling process. To evaluate the degree of excitation caused by this ramp, a second spilling process is performed as this removes any excited particles with high fidelity as sketched in figure 6.8. The influence of the second spilling process on the atom number distribution is shown in figures 6.7 (b) and (d). After the second spilling process the number of systems containing two atoms is reduced from 96(1)% to 92(2)%. As the second spilling process removes any particles occupying the second energy level, all systems consisting of three atoms after the first spilling process are converted into two-atom systems after the second spilling process. Therefore, one expects that the number of two-atom systems is increased by that amount to 98%. On the other hand, any excitation which is caused by ramping up the potential after the first spilling process should lead to a decrease in the number of two-atom systems after the second spilling process. Since we observe that 92(2)% of the systems consist of two atoms the difference of 6% gives an upper limit on the number of two-atom systems which where excited while ramping the barrier up.

6.3.1 Theoretical expectation

The expected excitation rate for an atom in the ground state of the microtrap has been calculated analytically for increasing and decreasing trap depths [Zha07, Wei11]. The main results are discussed in the following. The solution is found by solving the time dependent Schrödinger equation for the harmonic oscillator potential. Since the excitation operator corresponding to the change in trap depth has even symmetry, the smallest possible excitation is a transition from the first to the third energy state of the harmonic oscillator potential with energy difference $\Delta E = 2\hbar\omega_{\parallel}$. The criterion for adiabaticity yields [Zha07]

$$\hbar \left| \frac{d\omega(t)}{dt} \right| = \xi \frac{\Delta E^2}{\left| \left\langle \phi_e \left| \frac{\partial H}{\partial \omega} \right| \phi_g \right\rangle \right|} \tag{6.4}$$

where ξ denotes the adiabaticity factor, a numerical factor corresponding the degree of adiabaticity of the process, ϕ_g (ϕ_e) the wave function of the ground (excited) state and $\left| \left\langle \phi_e \left| \frac{\partial H}{\partial \omega} \right| \phi_g \right\rangle \right| = \hbar/\sqrt{2}$ holds for the harmonic oscillator. The differential equation 6.4 relates the speed of the change in trap frequency to the degree of adiabaticity. To maintain a constant ξ during the ramp, its shape has to follow

$$\omega(t) = \frac{\omega_\mathrm{i}}{1 - 4\sqrt{2}\xi\omega_\mathrm{i}\, t}. \tag{6.5}$$

where ω_i (ω_f) is the initial (final) trap frequency. The ramp time T can be calculated according to

$$T = \frac{1 - \frac{\omega_\mathrm{i}}{\omega_\mathrm{f}}}{4\sqrt{2}\xi\omega_\mathrm{i}}. \tag{6.6}$$

For the excitation probability one finds

$$P_e(t) = \frac{4\xi^2}{1 + 4\xi^2} \sin^2 \left(\frac{\sqrt{2\xi^2 + 1/2} \log\left(1 - 4\sqrt{2}\xi\omega_\mathrm{i} t\right)}{4\xi} \right). \tag{6.7}$$

To evaluate the degree of adiabaticity in our system we calculate ξ for experimentally used parameters. To end the spilling process we ramp the trap frequency of the microtrap within $T = 8\,\mathrm{ms}$ from $\omega_\mathrm{i} = 2\pi \times 779\,\mathrm{Hz}$ to $\omega_\mathrm{f} = 2\pi \times 1340\,\mathrm{Hz}$ while the gradient is applied. As we vary the trap depth linearly the slope of the trap frequency does not follow equation 6.5, therefore the magnitude of ξ is not kept constant during the ramp. An upper limit for ξ can be estimated by using equation 6.4

$$\xi \leq \frac{1}{4\sqrt{2}} \frac{\omega'_\mathrm{max}}{\omega^2} \tag{6.8}$$

where $\omega'_{\max} < 2\pi \times 140\,\mathrm{Hz/ms}$ is the maximum change in trap frequency during the ramp. We estimate an adiabaticity factor of $\xi < 7 \cdot 10^{-3}$ which yields a maximum excitation probability according to equation 6.7 as $P_{\max} = 4\xi^2/(1+4\xi^2) = 2 \cdot 10^{-4}$. Therefore we expect no excitations with the ramp speeds chosen in the experiment. In comparison, shortening the ramp to 1 ms yields $\omega'_{\max} = 2\pi \times 1100\,\mathrm{Hz/ms}$ and a corresponding excitation probability of 1%.
It is worth to note that it is in principle possible to obtain fast non-adiabatic ramp speeds without exciting the system because of the oscillatory behavior of equation 6.7. For this, the timing has to be chosen such that the excitation probability has a minimum.

6.4 State sensitive detection and imbalanced systems

We prepare systems with an imbalanced number of atoms in state $|1\rangle$ and $|2\rangle$. To

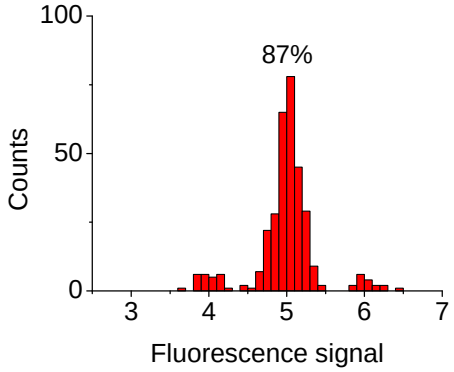

Figure 6.9: Fidelity of the preparation of an imbalanced system with 5 particles. By applying the state sensitive spilling technique arbitrary imbalances of the two components can be created. Here, a system with three atoms in state $|2\rangle$ and two atoms in $|1\rangle$ is prepared with 87% fidelity.

prepare such systems we utilize the fact that the atoms' magnetic moment depends on the magnetic offset field. In the high field regime (for fields above 100 Gauss), the magnetic moment is given as

$$\mu_{\mathrm{HF}} \simeq \mu_B g_J m_J \tag{6.9}$$

where $g_J = 2$ and $m_J = 1/2$ for the two lowest states of ^{6}Li. Therefore the force due to the applied magnetic field gradient is approximately the same for both

states. In the intermediate regime for $B \approx 40\,\text{Gauss}$, the magnetic moment of state $|2\rangle$ vanishes (inset of figure 6.10 (a)). At this offset field, only atoms in

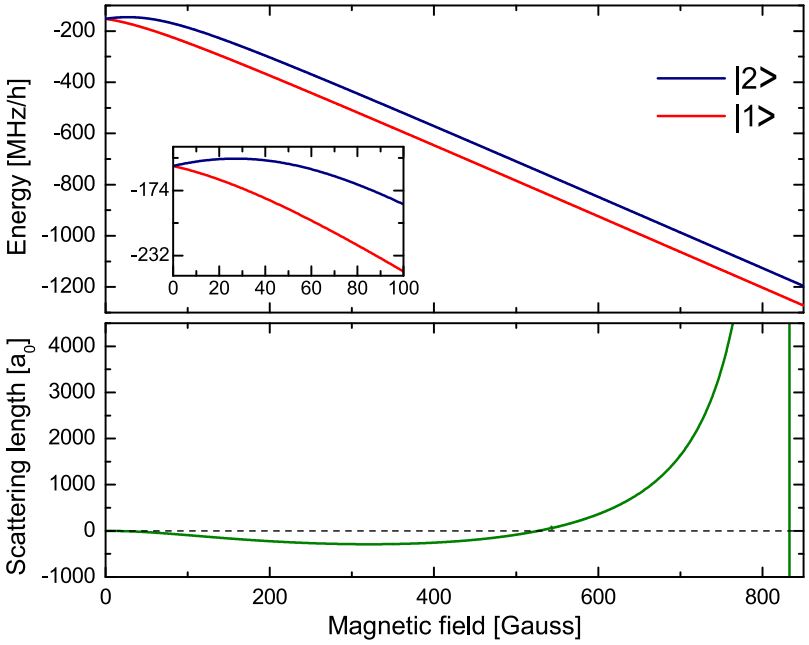

(a) When the spilling process is performed at an offset field of 40 Gauss, only atoms in state $|1\rangle$ are subjected to the force due to the magnetic field gradient because the magnetic moment of atoms in state $|2\rangle$ is negligible. Therefore only atoms in state $|1\rangle$ are spilled.

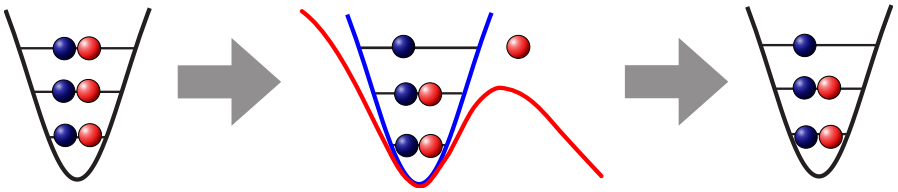

(b) The technique can be used to prepare systems with an imbalanced number of atoms in state $|1\rangle$ and $|2\rangle$ because the potential is tilted only for atoms in state $|1\rangle$. Furthermore it allows us to determine the number of atoms in state $|2\rangle$ by spilling all atoms in state $|1\rangle$ and counting the number of atoms remaining in the trap.

Figure 6.10: Spilling of one spin state.

state $|1\rangle$ are spilled when the gradient is applied (figure 6.10 (b)). For example, to prepare a system with three atoms in state $|2\rangle$ and two atoms in state $|2\rangle$ we

initially prepare a system consisting of three atoms in state $|1\rangle$ and $|2\rangle$ each. In an additional spilling process performed at an offset field of 40 Gauss, we remove one atom in state $|1\rangle$ as shown in figure 6.9.

The preparation fidelity of an imbalanced sample consisting of 5 atoms amounts to 87% as shown in the corresponding histogram.
In addition to the preparation of imbalanced systems this technique allows us to determine the number of atoms in state $|2\rangle$ by spilling all atoms in state $|1\rangle$ and counting the number of atoms remaining in the trap.

7 Entering the playground

After the first preparation of non-interacting few-fermion samples we used our new model system to explore one of the simplest non-trivial few-body systems: two repulsively interacting atoms confined in a one-dimensional harmonic potential. Such a two-particle systems forms the elementary building block of strongly correlated many-body systems in one dimension: Examples are the Tonks-Girardeau gas [Gir10] or the Luttinger liquid [Gia03].
Our results are presented in the first section of this chapter. One of the main findings is that we can utilize the spilling technique not only to prepare the samples, but also to determine the interaction energy of the system. We determine this energy by recording the tunneling time of one atom through the barrier as a function of the repulsion strength. Performing a precise measurement in this way requires detailed knowledge of the trapping potential, which we obtain by mapping out the energy levels of the potential. This is the focus of the second part of the chapter. With the measurement of the energy levels we fully characterize the potential described in the last part of the chapter. This allows us to relate the tunneling time to the energy of the system.
The techniques we developed to map out the confining potential allow us to control the motional quantum state of a single atom. Similar to the case of ions [Die89, Jak99] this degree of control is a crucial requirement for implementing quantum information schemes with neutral atoms [Hay07]. Here, we demonstrate this in a single optical dipole trap.

7.1 Two interacting atoms in a harmonic potential

As a starting point we prepare two non-interacting atoms in two spin states in the ground state of the potential. To determine the energy of the system, we tilt the potential by applying a magnetic field gradient of $B' = 18.9(1)$ Gauss/cm and measure the tunneling rates of atoms through the barrier as plotted in figure 7.1. An increase in interaction energy U effectively reduces the height of the tunneling barrier and therefore causes a decrease in the tunneling time. To measure the tunneling time of atoms occupying the lowest energy state we reduce the tunneling time t_0 of this state to experimental accessible timescales by choosing a slightly

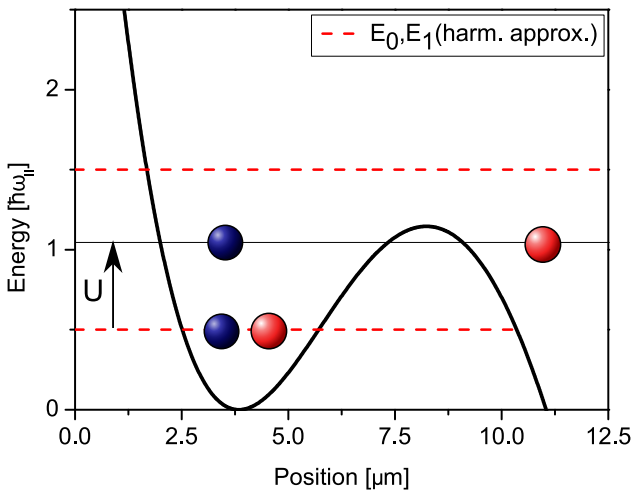

Figure 7.1: Measurement of the interaction energy U. We determine U by tilting the potential and recording the tunneling rate of atoms through the barrier. An increase in interaction energy U effectively reduces the height of the tunneling barrier and thus causes a decrease in the tunneling time.

lower value $s = 2.66/4 = 0.665$ for the optical potential than the one we use for the preparation. To measure the tunneling time, we hold the system in the tilted configuration for a hold time t_{hold}, ramp the potential back up to suppress further tunneling and record the mean atom number as function of the hold time. We perform this measurement for a strongly repulsive system by applying an offset field of 760 Gauss where the scattering length takes a value of $a = 4100\,a_0$. We compare this result to the non-interacting case ($a = 0$).

Figure 7.2 presents our main results. For a non-interacting system we obtain a value for the tunneling time of $t = (630 \pm 120)$ ms. According to WKB calculations we obtain a tunneling of $t = 790$ ms which agrees within $1.5\,\sigma$ with the experimental value. With repulsive interactions one atom leaves the trap on a fast timescale with $t = (6.8 \pm 0.5)$ ms. After the atom has left the trap, tunneling of the second atom becomes suppressed.

We observed a decrease in tunneling time by two orders of magnitude due to the raise in interaction energy in this measurement. However, a quantitative link between the tunneling time and the value of the scattering length a requires additional theoretical understanding. Because of the strong transverse confinement of the trapping potential the three dimensional scattering length a has to be rescaled by the strength of the confinement to obtain the right value for the effective in-

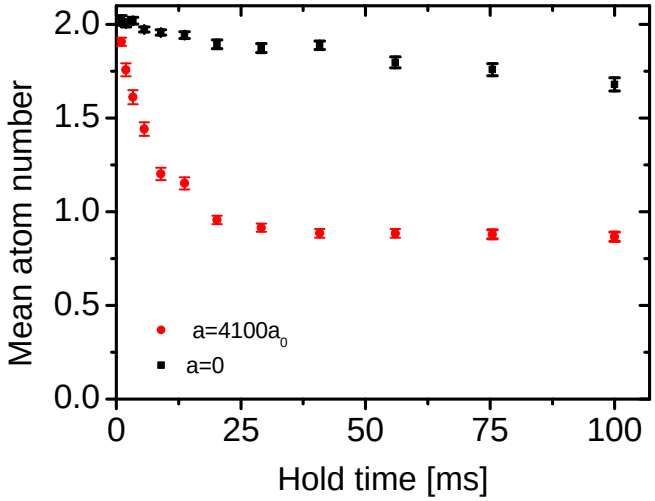

Figure 7.2: Interaction induced dynamics. We choose the height of the barrier such that two noninteracting atoms ($a = 0$) tunnel on a timescale of $t = (630 \pm 120)$ ms (black squares). With repulsive interactions ($a = 4100\, a_0$), one atom escapes on a fast timescale with $t = (6.8 \pm 0.5)$ ms. After this atom has left the trap, tunneling of the second atom becomes suppressed (red circles). Each data point is the average of $\sim$ 190 measurements. According to WKB calculations we obtain a tunneling of $t = 790$ ms for the non-interacting case which agrees within $1.5\,\sigma$ with the experimental value. From [Ser11].

teraction strength between the particles [Ols98] as discussed in chapter 4.3. Using this model, the energy shift in one dimension is calculated in the same way as done in chapter 4.3 for a parameter of $s = 2.66/4 = 0.665$ as used in this experiment. Since the values of s which correspond to plateaus in the mean atom number drifted about 2% over the time of some months and the potential has been characterized with the new parameters, s was rescaled in the calculation by a factor of $2.637/2.685 = 0.98$ to compensate for the drift. The coupling strength in one dimension is calculated as a function of magnetic field according to equation 4.49. With the value of the coupling strength the energy shift can be calculated using equation 4.39.
The expected shift is presented in figure 7.4 as a function of the applied magnetic field. The black line corresponds to the analytical solution, which is valid in the case of a one dimensional harmonic oscillator potential. For a magnetic field of $B = 760$ Gauss we expect an energy shift which is on the order of $\hbar\omega_{\parallel}$ and thus comparable to the level spacing of the potential. Since the tilted potential devi-

ates from the harmonic approximation, the actual expected energy shift is lower as discussed in chapter 4.3 . For the tilted potential, we obtain a ratio

$$A = \frac{\tilde{\omega}_{\parallel}}{\omega_{\parallel}} \sim 80\% \tag{7.1}$$

where $\tilde{\omega}_{\parallel} = (E_1 - E_0)/\hbar$ is obtained from the energy difference of the first and second bound state of the potential and $\omega_{\parallel}$ denotes the trap frequency in the harmonic approximation. In a complementary measurement of the energy shift for $g_{1d} \to \infty$, i.e. on the confinement induced resonance ($B \approx 784\,\text{Gauss}$), we found that the energy shift amount to $\hbar\tilde{\omega}_{\parallel}$ rather than $\hbar\omega_{\parallel}$. Therefore we deduce that rescaling the energy shift in units of $\hbar\tilde{\omega}_{\parallel}$ yields a more accurate solution in the case of an an-harmonic potential [Zür11].
As the tilted potential only supports one bound state, the magnitude of $\tilde{\omega}_{\parallel}$ cannot be directly calculated but has to be extrapolated from a potential depth where two bound states exist. For a depth corresponding to $s = 2.66/4 = 0.665$ as used in the experiment a value of $A = \tilde{\omega}_{\parallel}/\omega_{\parallel} = 0.75$ is extrapolated (figure 7.3). With

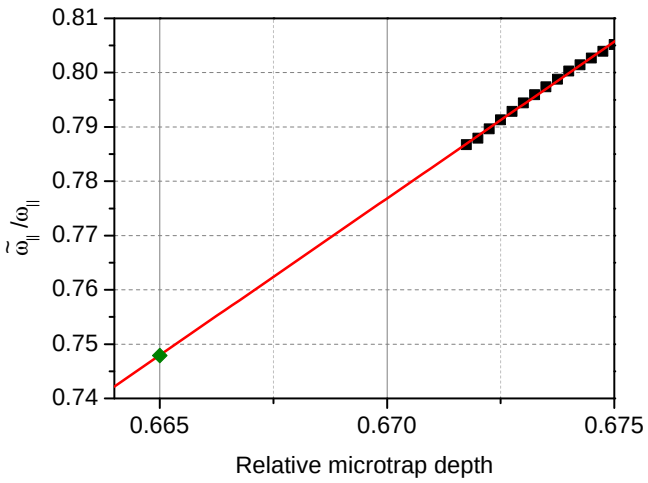

Figure 7.3: An-harmonicity of the tilted potential as a function of the microtrap depth. To obtain an estimation $\tilde{\omega}_{\parallel} = (E_1 - E_0)/\hbar$ for a microtrap depth at which the potential does not support two bound states we extrapolate the value $\tilde{\omega}_{\parallel} < 0.75(1)\,\omega_{\parallel}$ (green diamond) from the region where the potential supports two bound states.

this parameter we obtain a first order approximation for the expected energy shift by rescaling the solution for the harmonic case with A. The result is shown as the red curve in figure 7.4. The blue data points are obtained by calculating the

energies from the measured tunneling times by means of WKB calculations. For the noninteracting case, the measured energy shift of $(0.02 \pm 0.02)\hbar\omega_{\parallel}$ agrees within its error with the theoretical expectation. For the interacting case the measured energy shift amounts to $(0.48 \pm 0.01)\hbar\omega_{\parallel}$. This value is about 26% lower than the magnitude expected for the an-harmonic potential. This discrepancy can be attributed to the fact that the extrapolation of the magnitude of $\tilde{\omega}_{\parallel}$ yields only an upper limit. Quantitative agreement can be obtained when the an-harmonicity of the potential is reduced by increasing the optical trap depth [Zür11].

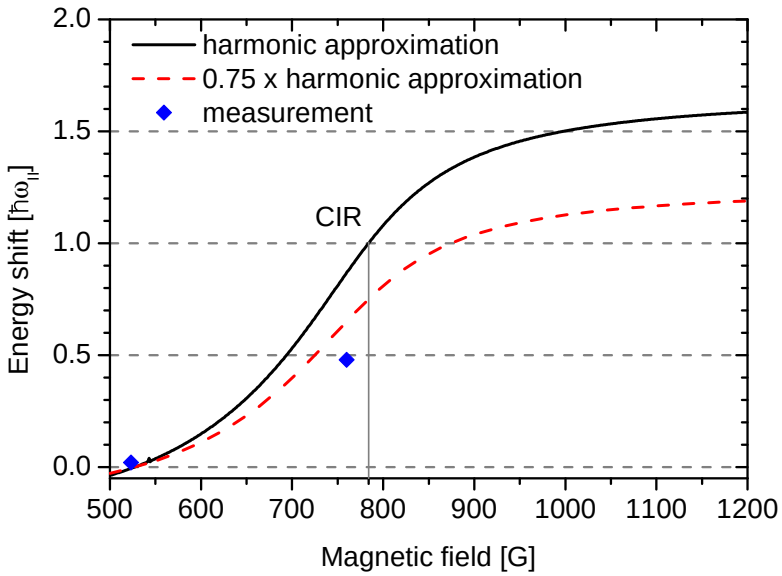

Figure 7.4: Energy shift caused by the interaction between the two particles. The energy shift is calculated analytically for a one-dimensional harmonic oscillator potential (black line). For a magnetic field of 783 Gauss the coupling strength diverges leading to a confinement-induced-resonance (CIR). On resonance the corresponding energy shift amounts to $U = 1\hbar\omega_{\parallel}$. For a magnetic field of $B = 760$ Gauss as applied in the experiment the shift becomes $U = 0.87\,\hbar\omega_{\parallel}$. As the tilted potential is an-harmonic the energy shift is expected to be lower (red line). The blue points represent the energy shift which is calculated from the measured tunneling time for a non-interacting and strongly repulsive interacting system.

7.2 Controlling the motional quantum state of a single atom

We map out the energy levels of the an-harmonic potential by manipulating the motional quantum state of the atom in the trap. Similar to standard spectroscopic techniques we record the excitation probability of the system as a function of the excitation frequency. An overview over the measured transitions is presented in figure 7.5.

To drive transitions between states with different parity such as the transition

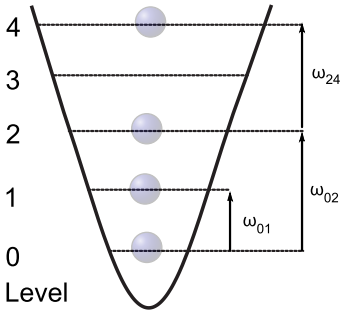

Figure 7.5: Experimental characterization of the an-harmonic potential. We map out the energies of the potential by driving transitions between the corresponding energy levels.

from level 0 to level 1, an operator with odd symmetry is required. We realize this operator by translating the center position of the potential x_0 with the excitation frequency ω by shaking the mirror in the optical path of the microtrap beam with a loudspeaker as shown in figure 7.6. Transitions where initial and final state have the same symmetry, e.g $0 \rightarrow 2$ and $2 \rightarrow 4$ are excited by modulating the depth of the optical potential V_0. The sequence we use to determine the frequency difference ω_{01} between the first and second energy level is sketched in figure 7.7 (a). As a starting point we prepare two non-interacting atoms in the ground state of the trap and excite them to the next energy level by modulating x_0. To determine the number of atoms in the ground state we spill atoms occupying excited states after the excitation pulse. The mean atom number in the ground state is plotted in figure 7.7 (b) as a function of the modulation frequency. We observe a minimum in the ground state population, i.e. a maximum excitation efficiency, for a frequency of $\omega_{01} = 2\pi\,(1486 \pm 11\,)$Hz according to a Lorentzian fit to the data.

The determination of the frequency difference between the first and third energy level ω_{02} is sketched in figure 7.8 (a). We start with one atom in the ground state of the trap which we prepare as discussed in section 6.4. Then we excite the atom

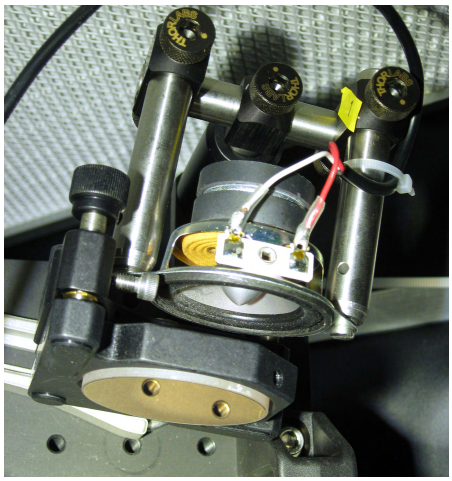

Figure 7.6: To excite an atom in the ground state to the first excited state with frequency ω_{01} the symmetry of the wave function has to change which requires an operator with odd symmetry. We realize this operator by translating the center position of the potential by shaking the micro-trap mirror with a loudspeaker.

to the third energy level by modulating the depth of the potential. To record the mean atom number in the ground state we perform another spilling process which only leaves ground state atoms trapped in the potential. Figure 7.8 (b) shows the mean atom number as a function of modulation frequency. The data show that we coherently drive this transition, in contrast to the $0 \rightarrow 1$ case. For a two-level system with ground and excited state the ground state population is given by the Rabi formula

$$P_g = 1 - P_e = 1 - \left(\frac{|\Omega|}{\Omega_{\text{eff}}}\right)^2 \sin\left(\frac{\Omega_{\text{eff}}}{2}t\right)^2 \tag{7.2}$$

where $\Omega_{\text{eff}} = \sqrt{|\Omega|^2 + \delta^2}$ is the effective Rabi frequency, $\delta = \omega_{02} - \omega$ denotes the detuning and Ω the Rabi frequency on resonance. Driving the system with a constant detuning δ results in Rabi oscillations of the occupation probability of ground and excited states with a frequency given by Ω_{eff}.
To determine the resonance frequency of the transition we measure the occupation probability as a function of ω, which changes the effective Rabi frequency Ω_{eff}. We drive the system with pulses with $N = 150$ cycles. From a fit of equation 7.2 to the data we extract the Rabi frequency given by the coupling strength between the two states and the resonance frequency ω_{02} of the transition. We find $\Omega = 2\pi \times 32(1)\,\text{Hz}$ where the error indicates the error of the fit and $\omega_{02} = 2\pi \times (2985 \pm 10)\,\text{Hz}$. This error is estimated by the width of the peak. The coherence time of the system

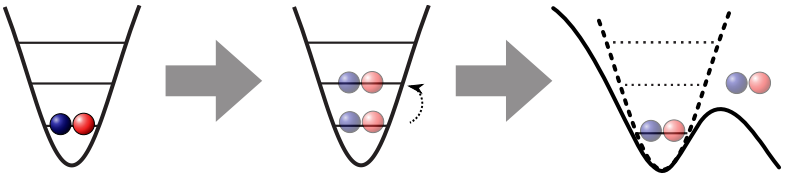

(a) To determine the frequency difference ω_{01} between the first and second energy level we prepare two non-interacting atoms in the ground state of the trap and excite them to the next energy level by modulating the center position of the potential. By spilling atoms in the excited state we determine the number of atoms in the ground state as a function of modulation frequency.

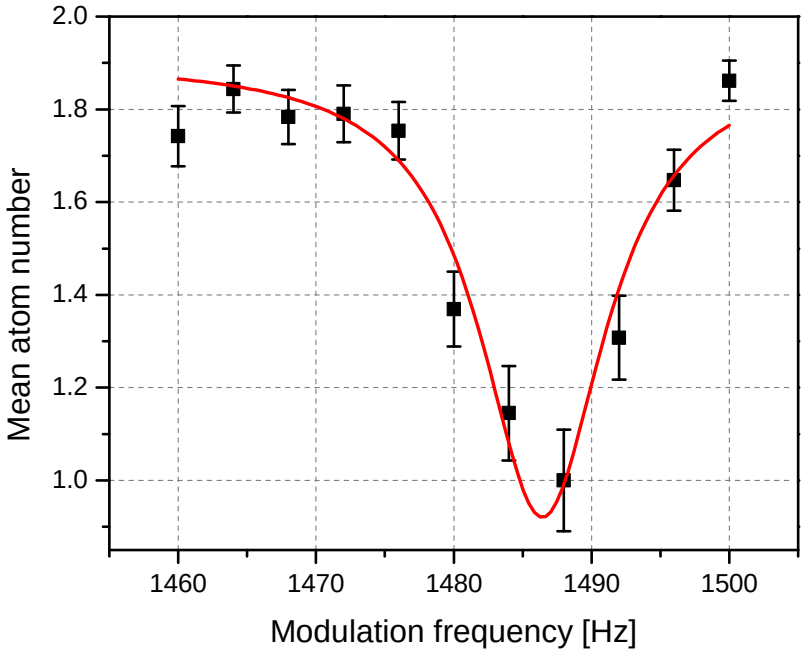

(b) Modulating at a frequency corresponding to the energy difference of first and second energy state yields a maximum in the number of atoms which are transferred to the excited state. Fitting a Lorentzian one finds $\omega_{01} = 2\pi\,(1486 \pm 11\,)$Hz where the error is given by the width of the peak.

Figure 7.7: First experiments with the few-particle system to characterize the potential.

exceeds $t \approx 150\,\text{cycles}/3\,\text{kHz} = 50\,\text{ms}$.
The transition frequency ω_{24} is determined in a similar way. To ensure that only the two relevant levels are involved the system is initialized as sketched in figure 7.9 (a). One atom occupying the third state of the trap is prepared by applying

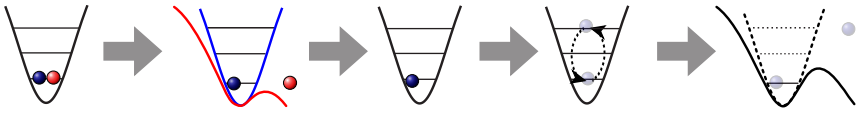

(a) To determine the frequency difference ω_{02}between the first and third energy level we prepare one atom in the ground state of the trap by applying the state sensitive spilling technique to a two atom system (see text). We excite the atom to the third energy level by modulating the depth of the potential. After applying the spilling technique again we record the mean atom number in the ground state as a function of modulation frequency.

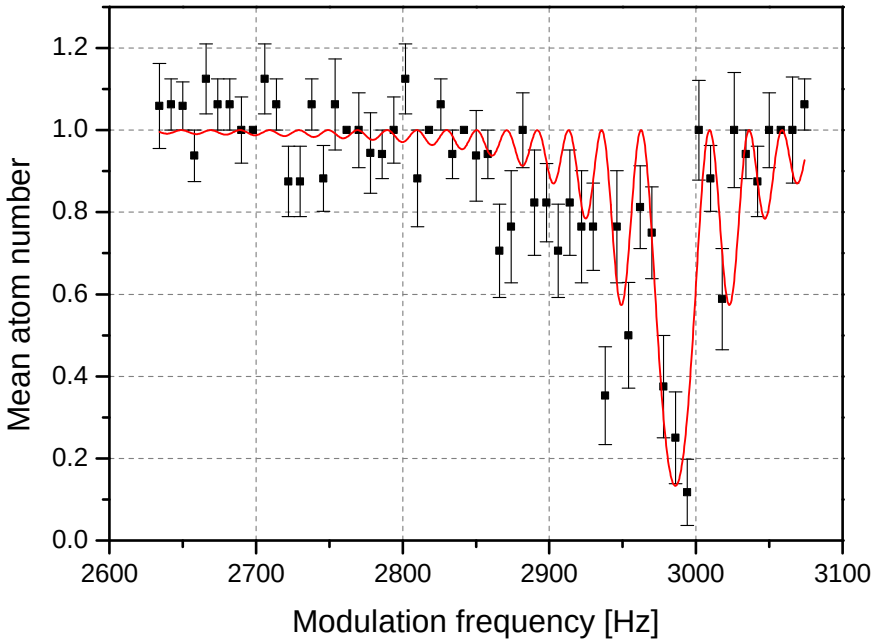

(b) A fit according to the Rabi formula for a two level system 7.2 shows that we drive the transition coherently from the ground state to the second excited state. We find $\omega_{02} = 2\pi\,(2985 \pm 10)\,\mathrm{Hz}$, where the error corresponds to the width of the main peak.

Figure 7.8: Coherent control of a single atom's motion in the microtrap.

a $\pi-$pulse with the measured frequency ω_{02} to a ground state atom. Since the pulse populates also higher levels, all atoms above the third level are removed by applying another spilling process. This yields a system with one atom occupying the third level. We excite the atom to the fifth level by modulating the depth of the potential as described previously. After applying the spilling technique again we measure the mean atom number in the third state as a function of the modulation frequency. The mean atom number as a function of modulation frequency is plotted

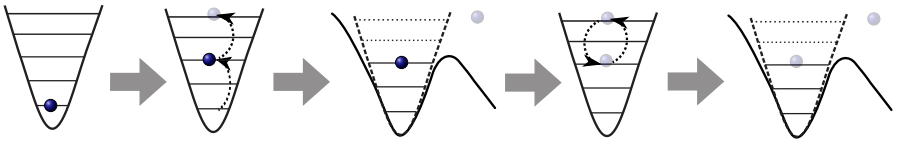

(a) The frequency difference ω_{24} between the third and fifth energy level is determined in a similar way. One atom is prepared in the third state of the trap by applying a $\pi-$pulse to a ground state atom. Since the $\pi-$pulse populates also higher levels, all atoms above the third level are removed by applying a spilling process. Then we excite the atom to the fifth level by modulating the depth of the potential. After applying the spilling technique again we record the mean atom number in the third state as a function of the modulation frequency.

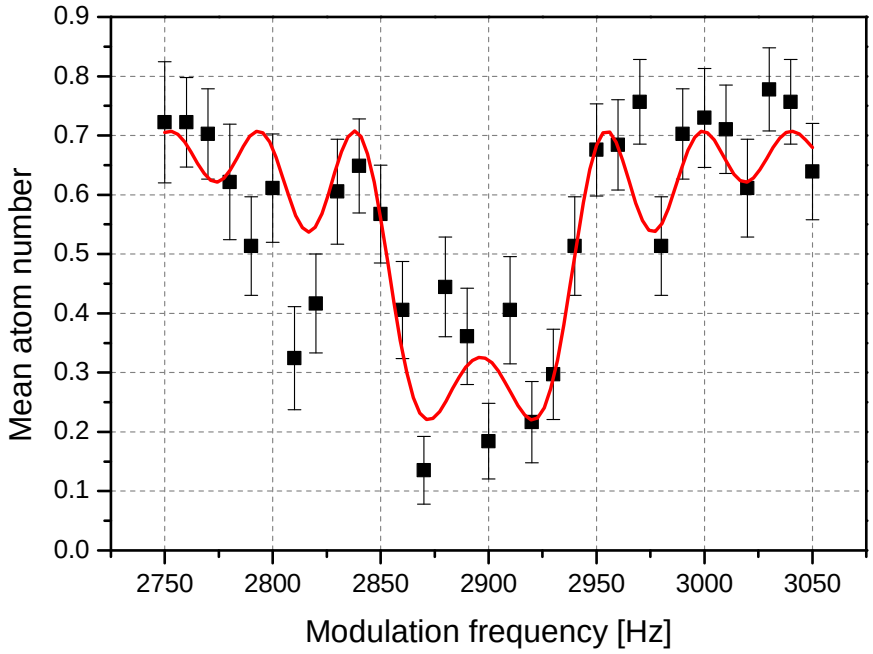

(b) This transition is also driven coherently. A fit according to the Rabi formula for a two level system 7.2 yields $\omega_{24} = 2\pi\,(2900 \pm 20)\,\mathrm{Hz}$ where the error corresponds to the width of the peak.

Figure 7.9: Determination of ω_{24} via coherent excitation.

in figure 7.9 (b) together with a fit according to equation 7.2. We observe that we drive this transition coherently as well, with pulses consisting of $N = 71$ cycles. For the Rabi frequency we obtain $\Omega = 2\pi \times 49(3)\,\mathrm{Hz}$ where the error indicates the error of the fit, and for the resonance frequency $\omega_{24} = 2\pi \times (2900 \pm 20)\,\mathrm{Hz}$. The error is estimated by the width of the peak.

We determine the transitions from level 0 to level 2 of the radial degree of freedom $\omega_{\perp 02}$ in the same way we obtain ω_{02}. Figure 7.10 presents the results. As the trap is slightly elliptic in radial direction, we obtain the two transition frequencies $\omega^{(1)}_{\perp 02} = 2\pi \times (28262 \pm 220)\,\mathrm{Hz}$ and $\omega^{(2)}_{\perp 02} = 2\pi \times (29066 \pm 62)\,\mathrm{Hz}$. These parameters are important since they determine the coupling strength $g_{1\mathrm{d}}$ as discussed in chapter 4.3. In particular, $g_{1\mathrm{d}}$ diverges when the scattering length a becomes reaches $0.68\,x_\perp$ where

$$x_\perp = \sqrt{\frac{2\hbar}{m\omega_\perp}} \tag{7.3}$$

denotes the harmonic oscillator length. To calculate the position of the confinement-induced-resonance we obtain for the radial trap frequency

$$\omega_\perp = \frac{\omega^{(1)}_{\perp 02}/2 + \omega^{(2)}_{\perp 02}/2}{2} = 2\pi \times 14330\,\mathrm{Hz}. \tag{7.4}$$

This value is used to calculate $g_{1\mathrm{d}}$ as done in chapter 4.3. According to this, the confinement induced resonance is at a magnetic field of 783 Gauss.

7.3 Characterizing the potential

As discussed in section 4.1, the potential can be treated purely one-dimensional. In z direction it can be written as a sum of a Lorentzian given in equation 3.46 and a linear term due to the applied magnetic field gradient B'. The combined potential becomes

$$V(z) = V_0 \left(1 - \frac{1}{1 + \left(\frac{z}{z_\mathrm{R}}\right)^2}\right) - \mu_B\, B'\, z$$

where V_0 is the depth of the optical potential at the trap center, $z_\mathrm{R} = \pi w_0^2/\lambda$ the Rayleigh length of the focused laser with $\lambda = 1064\,\mathrm{nm}$. According to equation 3.45 and 3.46 V_0 is given by

$$V_0 = -\frac{3\,\pi\,c^2}{2\,\omega_\mathrm{a}^3}\left(\frac{\Gamma}{\omega_\mathrm{a} - \omega} + \frac{\Gamma}{\omega_\mathrm{a} + \omega}\right)\frac{2P_m}{\pi w_0^2}, \tag{7.5}$$

where $\omega_\mathrm{a} = 2\pi \cdot 4.468 \cdot 10^{14}\,\mathrm{Hz}$ is the frequency of the atomic transition, $\Gamma = 2\pi \cdot 5.872\,\mathrm{MHz}$ its spontaneous decay width and $\omega = 2\pi c/\lambda$. Therefore three parameters are sufficient to determine the shape of the tilted potential: the power in the microtrap P_m, the size of the focus given by its waist w_0 and the applied

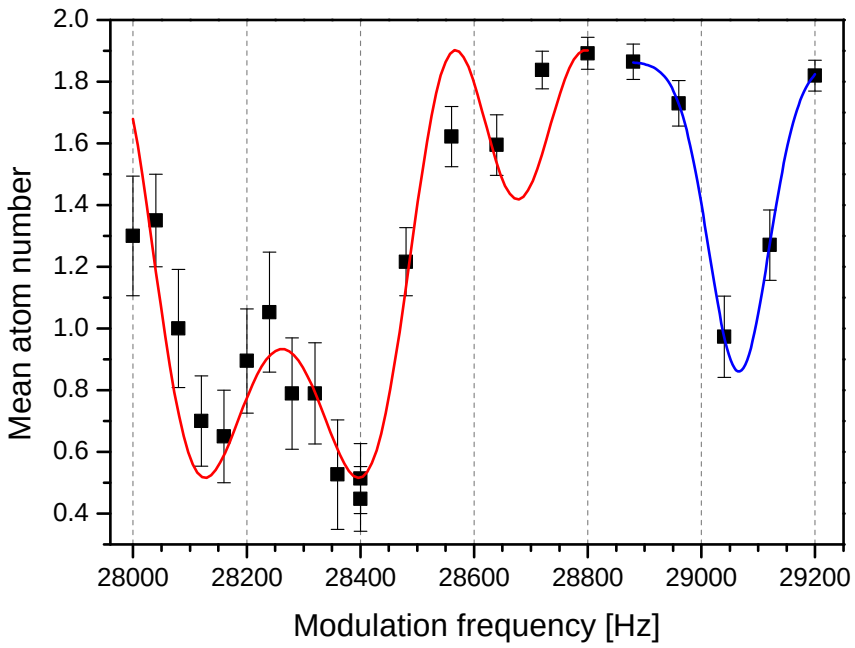

Figure 7.10: Radial trap frequencies. By modulating the depth of the microtrap we excite the system from the radial ground state to the second excited state. Since the trap is slightly elliptic the degeneracy of the eigenstates corresponding to the two main axes of the ellipse is lifted. Therefore we observe two transition frequencies $\omega^{(1)}_{\perp 02} = 2\pi \times (28262 \pm 220)\,\mathrm{Hz}$ and $\omega^{(2)}_{\perp 02} = 2\pi \times (29066 \pm 62)\,\mathrm{Hz}$ where the error is given by the width of the peaks.

magnetic field gradient B'.
To determine optimum parameters for w_0 and P_m, the energy states of the Lorentzian potential without gradient are calculated as described in chapter 4.2 for a combination of values w_0 and P_m. The energy difference between the states

$$\omega^{\mathrm{calc}}_{01} = (E^{\mathrm{calc}}_1 - E^{\mathrm{calc}}_0)/\hbar \tag{7.6}$$
$$\omega^{\mathrm{calc}}_{02} = (E^{\mathrm{calc}}_2 - E^{\mathrm{calc}}_0)/\hbar \tag{7.7}$$
$$\omega^{\mathrm{calc}}_{24} = (E^{\mathrm{calc}}_4 - E^{\mathrm{calc}}_2)/\hbar \tag{7.8}$$

is calculated and compared to the measured values. Optimum parameters are found by minimizing the sum of squares of the deviations from the measured values. The difference in measurement accuracy for the three transitions is accounted for

	experimental value	theoretical value
ω_{01}	$2\pi(1486 \pm 11)$ Hz	$2\pi\, 1504.38$ Hz
ω_{02}	$2\pi(2985 \pm 10)$ Hz	$2\pi\, 2983.73$ Hz
ω_{24}	$2\pi(2900 \pm 20)$ Hz	$2\pi\, 2884.46$ Hz

Table 7.1: Measured and calculated values for the three transition frequencies agree within 1σ for ω_{02}, ω_{24} and 2σ for ω_{01}

parameter	experimental value	theoretical value
P_{m}	265μW$\pm$10%	291.5μW
w_0		1.838μm
B'	18.9(1) Gauss/cm	18.92 Gauss/cm

Table 7.2: Final parameters used for the WKB calculation.

by weighting the squared deviations accordingly. We find

$$SQ = 2\left(\omega_{01}^{\mathrm{calc}} - \omega_{01}^{\mathrm{exp}}\right)^2 + 2\left(\omega_{02}^{\mathrm{calc}} - \omega_{02}^{\mathrm{exp}}\right)^2 + 1\left(\omega_{24}^{\mathrm{calc}} - \omega_{24}^{\mathrm{exp}}\right)^2 \tag{7.9}$$

The function SQ is minimized under the constraint that the value of P_{m} agrees with the measured value $P = 265\mu$W within the experimental uncertainty of 10%. The minimum is obtained for $w_0 = 1.838\mu\,\mathrm{m}$ and $P_{\mathrm{m}} = 291.5\,\mu$W. Table 7.1 lists both experimental and calculated values for the three frequencies. The values agree within 1σ for ω_{02}, ω_{24} and 2σ for ω_{01}.

For the trap depth at the center V_0 we find

$$V_0 = 3.326\,\mu K\, k_B. \tag{7.10}$$

After the parameters P_{m} and w_0 have been fixed the third parameter, the magnetic field gradient B', is determined independently by calculating the tunneling times through the potential barrier. We compare these with the tunneling times measured in the experiment. For a relative trap depth of $s = 2.75/4 = 0.6875$ we measure a tunneling time of $t_0 = 74$ ms for an atom occupying the second energy level which yields a value for the gradient of $B'_{\mathrm{theo}} = 18.92$ Gauss/cm. This is in excellent agreement with the measured gradient of $B' = 18.9(1)$ Gauss/cm. When this gradient is used as input parameter for the WKB calculation of the mean atom number as a function of relative microtrap depth according to equation 4.26, the theoretical expectation agrees well with the measurement for a broad range of trap depths as shown in figure 6.5. This strongly supports the choice of parameters for the potential. Table 7.2 lists the final parameters used for the calculation.

8 Conclusion and Outlook

During this thesis we deterministically prepared a few-fermion system using ultracold ^{6}Li atoms in an optical dipole trap. Ground-state samples consisting of one to ten fermions were prepared with a fidelity of $\sim 90\%$. This system has the unique property that important parameters such as particle number confining potential and inter[particle interactions are tunable.
We used this model system to explore one of the simplest non-trivial few-particle system possible: two interacting fermions in a one-dimensional harmonic potential. To determine the interaction shift which is caused by the repulsion of the particles we tilted the potential and measured the tunneling time of atoms through the resulting potential barrier. We deduce the interaction shift from the measured tunneling times using a WKB calculation. This requires detailed knowledge of the confining potential which we obtain by mapping out its energy states.
In contrast to other tunable quantum systems such as quantum dots and atomic clusters, inter-particle interaction and confining potential can be tuned *independently*. This makes our system uniquely suited to explore pairing in few-fermion systems.

8.1 Pairing in few-fermion systems

Strongly correlated few-fermion systems are the challenge of modern nuclear physics. A prime example is the Halo nucleus ^{11}Li [Neu08] which is stable because of pairing between fermions.
One approach to treat pairing in few-particle systems is to separate pairing effects from the rest of the system's Hamiltonian. This is the concept of the seniority model [Zel03, Mar10] which assumes that the Hamiltonian of the system can be written as a sum

$$H = H_0 + V_{\text{pair}} \tag{8.1}$$

where H_0 includes kinetic energy, potential energy and inter-particle interactions which can be incorporated into a mean field description. The pairing term V_{pair} accounts for correlations which cannot be incorporated into this mean field. The Hamiltonian is simplified by assuming that all single-particle states which are

determined as the solution of H_0 form one degenerate energy shell near the Fermi surface as sketched in figure 8.1. On top of this energy offset the spectrum is added which is caused by pairing of particles within this shell. This pairing spectrum is calculated analytically by diagonalizing the pairing term V_{pair} of the Hamiltonian. It is characterized by the number of unpaired particles denoted by the seniority s. The ground state is obtained for a fully paired system corresponding to $s = 0$. Since a system with odd particle number always leads to one unpaired particle, those systems are less strongly bound which causes the oscillation in binding energy as a function of particle number.

To observe non-trivial pairing effects, each energy level has to be occupied by

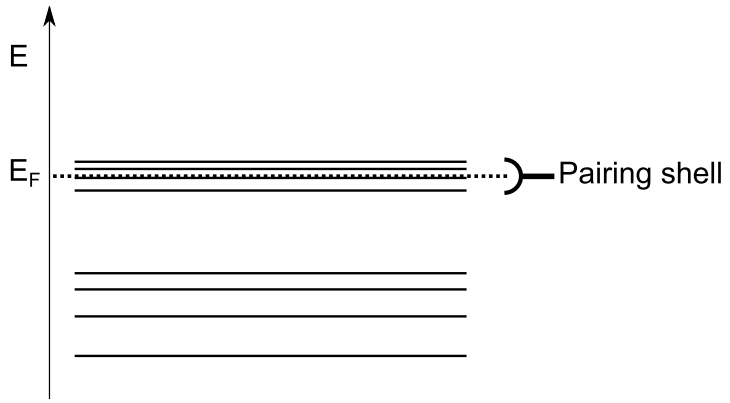

Figure 8.1: Energy spectrum of a few-fermion system. The effects of pairing can be isolated from the rest of the spectrum by assuming that single particle states form one degenerate energy shell near the Fermi surface.

more than two fermions. According to the Pauli's principle this requires degenerate energy shells which is fulfilled in a two- or three-dimensional system.
Thus, we can use a two-dimensional system as a starting point to explore pairing effects.
The corresponding Hamiltonian for ultracold atoms takes a form which is similar to the case of quantum dots as discussed in chapter 2.2. It reads

$$H = H_0 + H_{\text{int}} = \sum_{i=1}^{N} \left(-\frac{\hbar^2}{2m}\nabla_i^2 + \frac{m}{2}\omega r_i^2 \right) + \frac{1}{2} g \sum_{i \neq j} \delta^{\text{2D}} \left(\boldsymbol{r}_i - \boldsymbol{r}_j \right) \tag{8.2}$$

The difference to the case of quantum dots is that the Coulomb term has been replaced with a term describing interactions between ultracold atoms. In our system, the coupling strength g can be tuned to any value $-\infty < g < \infty$.
The interaction term of the Hamiltonian H_{int} has been solved by Rontani et al.

[Ron09] using the seniority model. They compare their result with their numerical solution of the full Hamiltonian using the full configuration interaction method (CI) [Ron06].
The energy spectrum of such an artificial atom can be characterized by means of two quantities [Cap07]: its ionization potential defined as

$$I(N) = E(N-1) - E(N) \tag{8.3}$$

and the electron affinity

$$A(N) = E(N) - E(N+1) \tag{8.4}$$

where $E(N)$ denotes the ground state energy of the N-particle system. The difference of those two quantities yields the fundamental energy gap

$$\Delta_2(N) = |I(N) - A(N)| \,. \tag{8.5}$$

The physical meaning of this parameter becomes evident when the solutions for a non-interacting system is compared with an attractively interacting system as done in figure 8.2. The green line corresponds to the solution of a weakly interacting system. Its energy structure is given by the eigenstates of the two dimensional harmonic oscillator as discussed in chapter 2.2. A maximum of $\Delta_2(N)$ appears for closed shells ($N = 2, 6$ particles) because the ionization potential has a maximum and the electron affinity vanishes, similar to the case of noble gases. For increasing attraction (figure 8.2 (b)) even-odd oscillations in the fundamental energy gap appear. This accounts for the fact that a pair has to broken to remove one particle from a system with even number of constituents . Therefore the ionization potential oscillates as a function of particle number. These results are qualitatively reproduced with the seniority model (figure 8.2 (c)).
To summarize, with the model system we can explore pairing in a two-dimensional few-fermion system by measuring the system's energy as a function of attractive interaction strength. We can directly compare these results to analytical and numerical predictions.

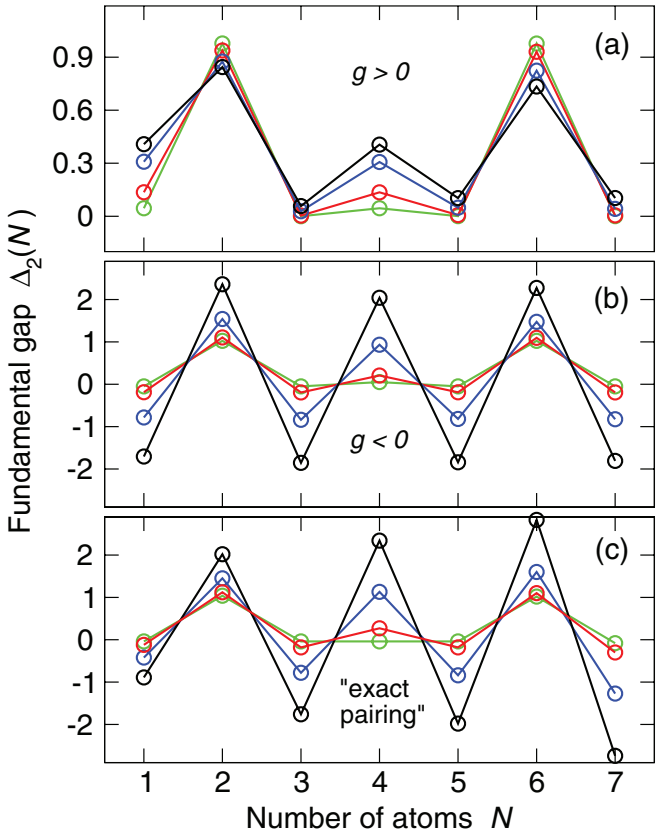

Figure 8.2: Pairing in a two-dimensional system. The energy spectrum of this system is characterized by the fundamental gap which denotes the difference in ionization energy and electron affinity. We can directly test numerical calculations for (a) repulsive and (b) attractive interactions. Results from the seniority model adapted from nuclear physics are shown in panel (c). The absolute value of interaction strength increases from the green, red, blue to black curve. The green curve corresponds to small interactions. The peaks for $N = 2, 6$ particles correspond to magic number of the potential. From [Ron09].

8.2 Quantum simulation of many-body systems

The understanding of correlated many-fermion systems in periodic potentials is the key challenge of condensed matter physics. The simplest possible description of interacting fermions in a periodic potential is the Fermi-Hubbard model, the most intensively studied model in the field. Its Hamiltonian only contains two parameters as sketched in figure 8.3 (A): The tunneling matrix element of particles to adjacent lattice sites t and the on-site interaction U, the energy shift caused by the interactions between the particles.
In spite of the simplicity of this model, it can only be solved analytically in one dimension. In two and three dimensions numerical predictions for its phase diagram can be given which still disagree in parts after decades of intensive research. Solving the model is considered as an important step towards the understanding of high-T_C superconductivity, one of the big open questions in condensed matter physics.
For repulsive interactions the low-temperature phase of this Hamiltonian is characterized by magnetic ordering. In the case of a three dimensional cubic lattice the system is predicted to undergo a phase transition into an antiferromagnetically ordered state if the temperature is reduced below the Néel temperature. In this phase two adjacent lattice sites are occupied with fermions in different spin states as sketched in figure 8.3 (B) for the case of an one-dimensional system.
The observation of such antiferromagnetic order in an ultracold Fermi gas is the biggest challenge in the field of cold quantum gases. To reach this goal the most crucial difficulty is to reduce the entropy per particle. However, this could not be reached in spite of intensive effort.
We prepare few-fermion systems in the ground state of a single trap with near zero entropy. In a bottom-up approach we can extend our system to an artificial molecule by splitting the trap adiabatically into multiple wells while preserving full control over the system's quantum state as indicated in figure 8.3 (B). This allows us to realize the building block of quantum spin systems in a finite, isolated system with control over the number of atoms, their spin state, the number of wells and the inter-particle interaction. Adding multiple potential wells in two dimensions brings us in the outstanding position to simulate the Fermi-Hubbard Hamiltonian in a two-dimensional system. Since we can tune the inter-particle interactions the determination of the long-sought phase diagram is in experimental reach. The magnetic ordered phases of the ground state can be directly detected using our spin selective detection scheme.
This achievement would be the first quantum simulation of an open and highly relevant problem in quantum physics.

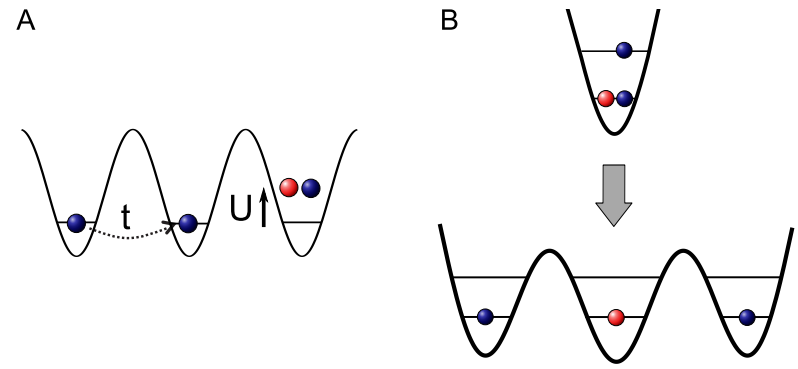

Figure 8.3: Fermi-Hubbard model and possible experimental realization. (A) The physics of interacting fermions in two spin states confined in a periodic potential is described by the Fermi-Hubbard model. It depends on two parameters, the tunneling matrix element t of atoms to adjacent lattice sites and the on-site interaction U given by the interaction strength. (B) Its main building block can be simulated with our model system by preparing a ground state sample in the microtrap and splitting the trap adiabatically into multiple potential wells.

Bibliography

[And95] M. H. Anderson, J. R. Ensher, M. R. Matthews, C. E. Wieman, E. A. Cornell, *Observation of Bose-Einstein Condensation in a Dilute Atomic Vapor*, Science **269**, 198 (1995).

[Bak09] W. S. Bakr, J. I. Gillen, A. Peng, S. Folling, M. Greiner, *A quantum gas microscope for detecting single atoms in a Hubbard-regime optical lattice*, Nature **462**, 74 (2009).

[Bar57] J. Bardeen, L. N. Cooper, J. R. Schrieffer, *Theory of superconductivity*, Phys. Rev. **108**, 1175 (1957).

[Bar05] M. Bartenstein, A. Altmeyer, S. Riedl, R. Geursen, S. Jochim, C. Chin, J. H. Denschlag, R. Grimm, A. Simoni, E. Tiesinga, C. J. Williams, P. S. Julienne, *Precise Determination of ^{6}Li Cold Collision Parameters by Radio-Frequency Spectroscopy on Weakly Bound Molecules*, Phys. Rev. Lett. **94**, 103201 (2005).

[Bel59] S. T. Belyaev, *Effects of Pairing Correlations on Nuclear Properties*, Mat. Fys. Medd. Dan. Vid. Selsk. **31**(11) (1959).

[Blo08] I. Bloch, J. Dalibard, W. Zwerger, *Many-body physics with ultracold gases*, Rev. Mod. Phys. **80**, 885 (2008).

[Boh58] A. Bohr, B. R. Mottelson, D. Pines, *Possible Analogy between the Excitation Spectra of Nuclei and Those of the Superconducting Metallic State*, Phys. Rev. **110**, 936 (1958).

[Bra93] M. Brack, *The physics of simple metal clusters: self-consistent jellium model and semiclassical approaches*, Rev. Mod. Phys. **65**, 677 (1993).

[Bra95] C. C. Bradley, C. A. Sackett, J. J. Tollett, R. G. Hulet, *Evidence of Bose-Einstein Condensation in an Atomic Gas with Attractive Interactions*, Phys. Rev. Lett. **75**, 1687 (1995), erratum: Phys. Rev. Lett. 79, 1170 (1997).

[Bus98] T. Busch, B.-G. Englert, K. Rzażewski, M. Wilkens, *Two Cold Atoms in a Harmonic Trap*, Foundations of Physics **28**, 549 (1998).

[Cap07] K. Capelle, M. Borgh, K. Kärkkäinen, S. M. Reimann, *Energy Gaps and Interaction Blockade in Confined Quantum Systems*, Phys. Rev. Lett. **99**, 010402 (2007).

[CAS] *CASIX*
http://www.casix.com/.

[Cas09] A. W. Castleman, S. N. Khanna, *Clusters, Superatoms, and Building Blocks of New Materials*, The Journal of Physical Chemistry C **113**, 2664 (2009).

[Chi10] C. Chin, R. Grimm, P. Julienne, E. Tiesinga, *Feshbach resonances in ultracold gases*, Rev. Mod. Phys. **82**, 1225 (2010).

[Cvi] *CVI Melles-griot*
https://www.cvimellesgriot.com/Products/Documents/TechnicalGuide/Gaussian-Beam-Optics.pdf.

[Dal98] J. Dalibard, *Collisional dynamics of ultracold atomic gases*, in M. Inguscio, S. Stringari, C. Wieman (Ed.), *Bose-Einstein Condensation in Atomic Gases*, Vol. Course CXL of *Proceedings of the International School of Physics Enrico Fermi* (IOS Press, Varenna, 1998).

[Dav95] K. B. Davis, M.-O. Mewes, M. R. Andrews, N. J. van Druten, D. S. Durfee, D. M. Kurn, W. Ketterle, *Bose-Einstein condensation in a gas of sodium atoms*, Phys. Rev. Lett. **75**, 3969 (1995).

[DeM99] B. DeMarco, D. S. Jin, *Onset of Fermi Degeneracy in a Trapped Atomic Gas*, Science **285**, 1703 (1999).

[Die89] F. Diedrich, J. C. Bergquist, W. M. Itano, D. J. Wineland, *Laser Cooling to the Zero-Point Energy of Motion*, Phys. Rev. Lett. **62**, 403 (1989).

[Fey82] R. Feynman, *Simulating physics with computers*, International Journal of Theoretical Physics **21**, 467–488 (1982), 10.1007/BF02650179.

[Fis08] R. E. Fischer, B. Tadic-Galeb, P. R. Roder, *Optical System Design* (SPIE Press, 2008).

[Fuh10] A. Fuhrmanek, A. M. Lance, C. Tuchendler, P. Grangier, Y. R. P. Sortais, A. Browaeys, *Imaging a single atom in a time-of-flight experiment*, New Journal of Physics **12**, 053028 (2010).

[Gia03] T. Giamarchi, *Quantum Physics in One Dimension* (Claredon Press Oxford, 2003).

[Gir10] M. D. Girardeau, *Two super-Tonks-Girardeau states of a trapped one-dimensional spinor Fermi gas*, Phys. Rev. A **82**, 011607 (2010).

[Gri00] Rudolf Grimm, Matthias Weidemüller, Yurii B. Ovchinnikov, *Optical dipole traps for neutral atoms*, Adv. At. Mol. Opt. Phys. **42**, 95 (2000).

[Haf11] D. Haffa, *A low noise source of 1064nm light by using a laser pointer*, Bachelor thesis, University of Heidelberg (2011).

[Hay07] D. Hayes, P. S. Julienne, I. H. Deutsch, *Quantum Logic via the Exchange Blockade in Ultracold Collisions*, Phys. Rev. Lett. **98**, 070501 (2007).

[Hee93] W. A. de Heer, *The physics of simple metal clusters: experimental aspects and simple models*, Rev. Mod. Phys. **65**, 611 (1993).

[Hen09] K. Henderson, C. Ryu, C. MacCormick, M. G. Boshier, *Experimental demonstration of painting arbitrary and dynamic potentials for Bose–Einstein condensates*, New Journal of Physics **11**, 043030 (2009).

[Her02] L. M. Herz, R. T. Phillips, *Quantum computing: Fine lines from dots*, Nature Materials **1**, 212 (2002).

[Hu94] Z. Hu, H. J. Kimble, *Observation of a Single-Atom in a Magneto-optical Trap*, Opt. Lett. **19**, 1888 (1994).

[Idz06] Z. Idziaszek, T. Calarco, *Analytical solutions for the dynamics of two trapped interacting ultracold atoms*, Phys. Rev. A **74**, 022712 (2006).

[Jak99] D. Jaksch, H.-J. Briegel, J. I. Cirac, C. W. Gardiner, P. Zoller, *Entanglement of Atoms via Cold Controlled Collisions*, Phys. Rev. Lett. **82**, 1975 (1999).

[Jul] P. Julienne, *Private Communications, Calculations done according to [Bar05]*.

[Ket99] W. Ketterle, D. S. Durfee, D. M. Stamper Kurn, *Making, probing and understanding Bose-Einstein condensates*, in M. Inguscio, S. Stringari, C. Wieman (Ed.), *Bose-Einstein Condensation in Atomic Gases*, Vol. CXL of *Proceedings of the International School of Physics Enrico Fermi*, 67–176 (IOS Press, Amsterdam, 1999).

[Ket08] W. Ketterle, M. W. Zwierlein, *Proc. of the International School of Physics Enrico Fermi, Course CLXIV, Varenna, Italy, 20 to 30 June 2006, M. Inguscio, W. Ketterle, C. Salomon, Eds.* (IOS Press, Amsterdam, 2008).

[Kni84] W. D. Knight, K. Clemenger, W. A. de Heer, W. A. Saunders, M. Y. Chou, M. L. Cohen, *Electronic Shell Structure and Abundances of Sodium Clusters*, Phys. Rev. Lett. **52**, 2141 (1984).

[Kou01] L. P. Kouwenhoven, *Few-electron quantum dots*, Reports on Progress in Physics **64**, 701 (2001).

[Lom08] T. Lompe, *An apparatus for the production of molecular Bose-Einstein condensates*, Diploma thesis, University of Heidelberg (2008).

[Lom10a] T. Lompe, T. B. Ottenstein, F. Serwane, K. Viering, A. N. Wenz, G. Zürn, S. Jochim, *Atom-Dimer Scattering in a Three-Component Fermi Gas*, Phys. Rev. Lett. **105**, 103201 (2010).

[Lom10b] T. Lompe, T. B. Ottenstein, F. Serwane, A. N. Wenz, G. Zürn, S. Jochim, *Radio-Frequency Association of Efimov Trimers*, Science **330**, 940 (2010).

[Lom11] T. Lompe, *Efimov Physics in a three-component Fermi gas*, Dissertation, University of Heidelberg (2011).

[Mah82] V. N. Mahajan, *Strehl ratio for primary aberrations: some analytical results for circular and annular pupils*, J. Opt. Soc. Am. **72**, 1258 (1982).

[Mar10] J. A. Maruhn, P.-G. Reinhard, E. Suraud, *Simple Models of Many-Fermion Systems* (Springer-Verlag, New York, 2010).

[Mer98] E. Merzbacher, *Quantum Mechanics* (John Wiley and Sons, Inc., 1998), 3rd Edn.

[Met99] H. J. Metcalf, P. van der Straten, *Laser Cooling and Trapping* (Springer-Verlag, New York, 1999).

[Moe95] A. J. Moerdijk, B. J. Verhaar, A. Axelsson, *Resonances in ultracold collisions of ^{6}Li, ^{7}Li, and ^{23}Na*, Phys. Rev. A **51**, 4852 (1995).

[Neu08] R. Neugart, D. L. Balabanski, K. Blaum, D. Borremans, P. Himpe, M. Kowalska, P. Lievens, S. Mallion, G. Neyens, N. Vermeulen, D. T. Yordanov, *Precision Measurement of Li11 Moments: Influence of Halo Neutrons on the Li9 Core*, Phys. Rev. Lett. **101**, 132502 (2008).

[Ols98] M. Olshanii, *Atomic Scattering in the Presence of an External Confinement and a Gas of Impenetrable Bosons*, Phys. Rev. Lett. **81**, 938 (1998).

[Ott08] T. B. Ottenstein, T. Lompe, M. Kohnen, A. N. Wenz, S. Jochim, *Collisional Stability of a Three-Component Degenerate Fermi Gas*, Phys. Rev. Lett. **101**, 203202 (2008).

[Ott10] T. B. Ottenstein, *Few-body physics in ultracold Fermi gases*, Dissertation, University of Heidelberg (2010).

[Rei02] S. M. Reimann, M. Manninen, *Electronic structure of quantum dots*, Rev. Mod. Phys. **74**, 1283 (2002).

[Rev09] J. U. Reveles, P. A. Clayborne, A. C. Reber, S. N. Khanna, K. Pradhan, P. Sen, M. R. Pederson, *Designer magnetic superatoms*, Nature Chemistry **1**, 310 (2009).

[Ron06] M. Rontani, C. Cavazzoni, D. Bellucci, G. Goldoni, *Full configuration interaction approach to the few-electron problem in artificial atoms*, J. Chem. Phys. **124**, 124102 (2006).

[Ron09] M. Rontani, J. R. Armstrong, Y. Yu, S. Åberg, S. M. Reimann, *Cold Fermionic Atoms in Two-Dimensional Traps: Pairing versus Hund's Rule*, Phys. Rev. Lett. **102**, 060401 (2009).

[Sch98] Schünemann, Engler, Zielonkowski, Weidemuller, Grimm, *Magneto-optic trapping of lithium using semiconductor lasers*, Optics Communications **158**, 263 (1998).

[Sch07] F. Schwabl, *Quantenmechanik* (Springer-Verlag Berlin, 2007), 7th Edn.

[Ser07] F. Serwane, *The setup of a Magneto Optical Trap for the preparation of a mesoscopic degenerate Fermi gas*, Diploma thesis, University of Heidelberg (2007).

[Ser11] F. Serwane, G. Zürn, T. Lompe, T. B. Ottenstein, A. N. Wenz, S. Jochim, *Deterministic Preparation of a Tunable Few-Fermion System*, Science **332**, 336 (2011).

[Sha11] E. R. Shanblatt, D. G. Grier, *Extended and knotted optical traps in three dimensions*, Opt. Express **19**, 5833 (2011).

[She10] J. F. Sherson, C. Weitenberg, M. Endres, M. Cheneau, I. Bloch, S. Kuhr, *Single-atom-resolved fluorescence imaging of an atomic Mott insulator*, Nature **467**, 68 (2010).

[Ste09] A. G. Steele, G. Gotz, L. Kouwenhoven, *Tunable few-electron double quantum dots and Klein tunnelling in ultraclean carbon nanotubes*, Nature Nanotechnology **4**, 363 (2009).

[Tak05] M. Takamoto, F.-L. Hong, R. Higashi, H. Katori, *An optical lattice clock*, Nature **435**, 321–324 (2005).

[Tar96] S. Tarucha, D. G. Austing, T. Honda, R. J. van der Hage, L. P. Kouwenhoven, *Shell Filling and Spin Effects in a Few Electron Quantum Dot*, Phys. Rev. Lett. **77**, 3613 (1996).

[Wal09] N. Walsh, A. Herlert, F. Martinez, G. Marx, L. Schweikhard, *Atomic clusters in a Penning trap: investigation of their properties and utilization as diagnostic tools*, Journal of Physics B: Atomic, Molecular and Optical Physics **42**, 154024 (2009).

[Wei11] C. Weitenberg, S. Kuhr, K. Molmer, J. F. Sherson, *A quantum computation architecture using optical tweezers*, http://arxiv.org/abs/1107.2632 (2011).

[Wit05] V. Witt, *Wie funktionieren Achromat und Apochromat?*, Sterne und Weltraum **October**, 75 (2005).

[Zel03] V. Zelevinsky, A. Volya, *Nuclear pairing: New perspectives*, Physics of Atomic Nuclei **66**, 1781 (2003).

[Zha07] C. Zhang, V. W. Scarola, S. Das Sarma, *Initializing a quantum register from Mott-insulator states in optical lattices*, Phys. Rev. A **75**, 060301 (2007).

[Zim11] B. Zimmermann, T. Müller, J. Meineke, T. Esslinger, H. Moritz, *High-resolution imaging of ultracold fermions in microscopically tailored optical potentials*, New Journal of Physics **13**, 043007 (2011).

[Zür09] G. Zürn, *Realization of an Optical Microtrap for a Highly Degenerate Fermi Gas*, Diploma thesis, University of Heidelberg (2009).

[Zür11] G. Zürn, F. Serwane, T. Lompe, A. Wenz, M. Ries, J. Bohn, S. Jochim, *Fermionization of two distinguishable fermions*, in preparation (2011).

[Zwi06] M. W. Zwierlein, *High-Temperature Superfluidity in an Ultracold Fermi Gas*, Dissertation, MASSACHUSETTS INSTITUTE OF TECHNOLOGY (2006).

Danksagung

Ich danke allen, die mich über die letzten Jahre hinweg begleitet haben. Durch sie wurde diese Arbeit ermöglicht.

Die Entscheidung vor 5 Jahren bei *Selim* in der Gruppe anzufangen war die beste, die ich hätte treffen können. Er hat mir soviel gezeigt, wie ich an andere Stelle nicht hätte lernen können. Insbesondere hat er mich durch seine ungeheure Neugier angesteckt. Ich kenne sonst niemanden, der sich für so viel interessiert. Er hatte stets Zeit für Diskussionen und Späße auch ausserhalb der Physik. Ein Abschied wird mir sehr schwerfallen.

Mein Dank gilt auch allen meinen Gruppenmitgliedern: *Thomas, Timo, Andre, Gerhard, Matthias, Martin, Philipp, Daniel, Johanna, Andrea, Sebastian und Juliana*. Danke, dass wir zusammen diese Maschine gebaut haben, für die Unterstützung während der letzten Jahre und die Antworten auf meine Fragen. Ebenso möchte ich mich für das intensive Korrekturlesen der Arbeit bedanken. Auch ausserhalb des Labors hatte ich viel Spass mit euch: Wenn ich eine Formkrise beim Tischfussball hatte, habt ihr mich stets wieder aufgebaut. Am Ende haben die alten Herren in Gerhard und Andre einen würdigen Gegner gefunden.

Professor Blaum danke ich für das Lesen meiner Arbeit.

Der *Gruppe von Professor Ullrich* danke ich für die großzügige Unterstützung und die angenehme Atmoshpäre während der Zeit am MPI.

Florian Säubert und der Lehrwerkstatt danke ich für die absolut krassen Sachen, die sie immer für uns gebastelt haben. Beispielsweise der Objektivhalter, der auch justiert bleibt wenn ein Kleinwagen darüber fährt.

Meiner Mutter Gerda und meinem Bruder Felix danke ich, dass sie mich immer unterstützt haben, auch in schwierigen Zeiten.

Mechtild Hartmann und Karl Schnekenburger danke ich, dass sie für meine Familie und mich da sind.

Julia danke ich, dass sie mich in meinem Leben begleitet.
Laurin, dass er bald mit mir Fahrrad fährt.